AES/RE/13-32

Geomechanical modelling and subsidence prediction of salt deposits for solution mining

30/08/2013

E.A.M. Wijermars

TU Delft Delft University of Technology

Challenge the future

Title	:	Geomechanical modelling and subsidence prediction of salt deposits for solution mining
Author(s)	:	E.A.M. Wijermars
Date	:	30 August 2013
Professor(s)	:	Dr. M.W.N. Buxton Dr. ir. D.M.J. Ngan-Tillard Dr. P.J. Vardon
External supervisor(s)	:	Ir. T.M. Pinkse (AkzoNobel) Dr. ir. G.M.A. Schreppers (TNO DIANA)
TA Report number	:	AES/RE/13-32
Postal Address	:	Section for Resource Engineering Department of Geoscience & Engineering Delft University of Technology P.O. Box 5028 The Netherlands
Telephone	:	(31) 15 2781328 (secretary)
Telefax	:	(31) 15 2781189

Abstract

AkzoNobel currently mines salt from bedded and domal salt deposits in the Netherlands and Denmark by solution mining. A new brine field will be developed in the coming years in a pillow salt deposit, which is the intermediate between bedded and domal salt deposits, near Haaksbergen (the Netherlands). The geomechanical models that have been developed in the past years to prove the stability of the caverns (underground cavities created during the mining process) differ in all salt operations. The same applies to the methods that were applied to predict subsidence at surface above the caverns that slowly decrease in volume (cavern convergence) due to the creep behaviour of salt. The aim of this work is to analyze and explain the differences in geomechanical modelling and subsidence predictions of bedded and domal salt deposits, to consider how this knowledge can be applied to pillow salt deposits and to investigate which parameters have significant effect on the convergence of caverns and subsidence.

The conclusion from studying the geomechanical models and subsidence predictions is that there is no significant difference in the approach to model caverns in a bedded salt deposit opposed to caverns in a salt dome. The differences lie in, for example, the values of material parameters and not in the choice of a material model. The fact that different material models and evaluation criteria have been used to model AkzoNobel's salt deposits is due to the fact that different consultants or institutions developed these models. All institutions have developed their own approach to the modelling process and therefore the models that they develop are different. Besides parameter values, the nature of salt deposits does determine which simplifications and assumptions are justified. An example is the consideration of a constant temperature or a depth dependent temperature.

A single cavern axisymmetric analysis has been carried out to investigate the effect of cavern dimensions, salt properties and overburden elasticity on the convergence behaviour of a cavern and subsidence at surface. The results indicate that the magnitude of the creep properties of salt have the largest influence on the convergence behaviour of a cavern. This is followed by the cavern volume. Whether this volume is changed by adjusting the cavern diameter or the thickness of the salt roof or floor has a minor influence. Results of volume comparisons show that the elasticity of the salt and overburden have a minor influence on the amount of converged volume that contributes to the volume of the subsidence bowl at surface.

A double cavern plane strain analysis shows that the convergence of caverns that are separated by a wider pillar is larger than for models with thinner pillars. Stress profiles across the pillars show that the pillars carry an increasing load when they become wider. This higher load causes more deformation and therefore more cavern convergence.

Regarding the future Haaksbergen brine field, there is no need to make the current geomechanical model and subsidence prediction better, because cavern stability is proven and the amount of subsidence is within acceptable limits. Moreover, there are no data available that could be implemented in a more sophisticated model. However, sensitivity analyses could be done to investigate how more sophisticated models would influence the results. This can also confirm or deny the necessity of gathering more data of the Haaksbergen salt deposit and overburden.

Acknowledgements

This thesis is the final work of my MSc program in Applied Earth Sciences. During the nine months that I've been working on this thesis, I received essential help and support from a number of people. In the final phase of this thesis work, I would like to express my gratitude to everyone who has been valuable for this work.

First of all, I would like to thank my TU Delft supervisors, Mike Buxton, Phil Vardon and Dominique Ngan-Tillard, for their input and advice during our monthly meetings that were very important to me. Also outside these meetings they were available to discuss a problem or to help me to make decisions about the work and its planning.

I would like to thank AkzoNobel's Mining Technology Department for giving me the opportunity to do my thesis work in the professional environment that this department is. The input and support during my monthly presentations were very valuable. I would like to mention Tobias Pinkse and Wim Paar in particular who helped me to interpret the department's questions that formed the motivation of this work. Special thanks to department manager Rob Selles who has been essential in the interpretation of the modelling results. I would also like to thank fellow student Daan van Berkel for finding a way for me to do volume calculations using Surpac, and for his company in the apartment in Hengelo that AkzoNobel provided.

Thanks to Gerd-Jan Schreppers from TNO DIANA, who was enthusiastic about my project, I got great support from Chantal Frissen in my modelling study. I would like to thank Chantal for being available for small questions as well as for the longer sessions and Gerd-Jan for giving me this opportunity. Also I would like to thank Max Hendriks (TU Delft) for bringing me into contact with TNO DIANA and providing the license.

In the last stage of this work, which consisted mainly of writing this thesis, I spent a considerable amount of time in the 'Afstudeerzolder'. The company of Hanne, Ruben, Tijs and Barend contributed to a good working environment and nice coffee and lunch breaks.

Finally I would like to thank my family and friends. Their continuous support throughout the past nine months meant a lot to me.

Table of Contents

Abstract i
Acknowledgements ii
List of figures vi
List of tables xi
List of symbols xii
Appendices xvi
1. Introduction 1
1.1. Project motivation 1
1.2. Research questions 2
1.3. Objectives 2
1.4. Thesis outline 2
2. Salt deposits and solution mining 1
2.1. Geology of salt deposits 3
2.1.1. Deposition of salt 3
2.1.2. Salt properties 4
2.1.3. Salt tectonics 5
2.2. Solution mining 6
3. Foundations and principles of geomechanical modelling and subsidence predictions in salt solution mining operations 8
3.1. Rock mechanics 8
3.1.1. Stress and strain 8
3.1.2. Elasticity and plasticity 9
3.2. Stress analysis 11
3.2.1. Stress components, principal stress and stress invariants 11
3.2.2. Material models 13
3.2.3. Evaluation criteria 18
3.3. Geomechanical modelling 21
3.3.1. Process of geomechanical modelling 21
3.3.2. Model types 22
3.4. Subsidence prediction 23
3.4.1. BGR method 24

3.4.2. Salt-subsid method 27
4. Hengelo brine field 28
4.1. Geology 28
4.2. Mining 30
4.3. Geomechanical model 32
4.3.1. Row pillars 32
4.3.2. In-line pillars 38
4.4. Subsidence prediction 44
5. Delfzijl brine fields 46
5.1. Geology 46
5.2. Mining 48
5.3. Geomechanical model 49
5.3.1. Heiligerlee and Zuidwending brine fields 49
5.3.2. Gas storage Zuidwending 54
5.4. Subsidence prediction 59
6. Cheshire 60
6.1. Geology 60
6.2. Geomechanical model 60
7. Future Haaksbergen brine field 64
7.1. Geology 64
7.2. Mining 66
7.3. Geomechanical model 66
7.4. Subsidence prediction 70
8. Combined model of the Haaksbergen brine field 71
8.1. Single cavern analysis 72
8.1.1. Scope and objectives 72
8.1.2. Model type 72
8.1.3. Calculation variants 72
8.1.4. Simplifications and assumptions 75
8.1.5. Material behaviour and parameters 80
8.1.6. Evaluation criteria and subsidence prediction 81
8.2. Two cavern analysis 82

8.2.1. Scope and objectives 82
8.2.2. Model type 82
8.2.3. Calculation variants 82
8.2.4. Simplifications and assumptions 83
8.2.5. Material behaviour and parameters 85
8.2.6. Evaluation criteria and subsidence prediction 85
8.3. Calibration of creep properties 85
10.3.1. Creep rates Haaksbergen salt 86
10.3.2. Single element analysis in DIANA 87
9. Results and discussion 89
9.1. Tests on base case 89
9.1.1. Base case 89
9.1.2. Mesh size 93
9.1.3. Phased cavern development 93
9.1.4. Long term response 96
9.1.5. Cavern sealing after operation 97
9.1.6. Depth dependency 98
9.2. Single cavern analysis 100
9.2.1. Cavern dimensions 100
9.2.2. Salt properties 104
9.2.3. Elasticity moduli 109
9.3. Double cavern analysis 112
9.3.1. Comparison with axisymmetric analysis 112
9.3.2. Pillar width 114
10. Conclusion and recommendations 118
10.1. Conclusions 118
10.2. Recommendations 120
11. References 122
Appendix A: Detailed diagram of the process of geomechanical modelling and subsidence prediction I
Appendix B: Process of building and running a model using DIANA II

List of figures

Figure 1: 4.8 m column of evaporites originating from a 300 m column of seawater, after Robertson Handford (1991) 4
Figure 2: Bedded salt deposit (a), pillow salt deposit (b) and salt dome (c), (Geluk *et al.*, 2003) 5
Figure 3: Schematic overview of a cavern and well operating in top injection mode (Geluk *et al.*, 2003) ... 6
Figure 4: Sketch of elastic (blue) and plastic (red) behaviour with linear elastic unloading-reloading curves, after lecture notes 'Computer modelling of engineering materials' by M. Hicks (TU Delft) 9
Figure 5: Basic difference in behaviour between creep and non-creep materials 10
Figure 6: Components of stress acting on a cube in a Cartesian coordinate system 11
Figure 7: Principal stresses on a cube 12
Figure 8: Hooke's Law's representation of elastic behaviour and fictional test results 13
Figure 9: Mohr-Coulomb failure criterion and fictional test results 14
Figure 10: Drucker-Prager shear failure criterion and fictional test results 15
Figure 11: BGRa creep model and fictional test results 16
Figure 12: Sketch of fictional creep test results that show primary and secondary creep 17
Figure 13: Schematic representation of the Minkley material model, (IfG, 2010) 17
Figure 14: Curves of volumetric strain (blue) and differential stress (red) during a fictional triaxial test .. 19
Figure 15: Invariant diagram with the dilatancy boundary (blue) and short term strength (red) derived from fictional test results 19
Figure 16: Flow diagram of the steps in a geomechanical modelling process 21
Figure 17: Illustration of parameters used in the unit shape function, as a plan view (left) and cross section (right), (BGR, 2006) 25
Figure 18: Location of AkzoNobel's mining permits in Twente in 2012 28
Figure 19: Cross section of the geology of the Hengelo brine field, (Drost, 2012) 29
Figure 20: Four cavern categories in the Hengelo brine field: (1) Early SCCs, (2) Early MCCs, (3) Modern MCCs, (4) Modern SCCs 30
Figure 21: Spread of cavern categories over the Hengelo brine field, in 2012 31
Figure 22: Part of the Hengelo brine field with the Usseleres caverns arranged in parallel rows 32
Figure 23: Plan view of caverns represented by wells (green dots) that are aligned in rows with row pillars in between (indicated in red) 33

Figure 24: Complete geomechanical model (left), magnification of zone around cavern (right), (BGR, 2004b) 33
Figure 25: Pressure at 425 m depth where the roof of the cavern is situated, (BGR, 2004b) 35
Figure 26: Result of P-D combinations for base case after 200 years, (BGR, 2004b) 37
Figure 27: Plan view of row configuration of cavern wells (green dots) with in-line pillars (red) 38
Figure 28: The entire 3D in-line pillar model (left) and a magnification of the zone around the caverns (right), (BGR, 2004c) 39
Figure 29: Pressure variations in time in cavern 1 with work-overs (blue) and cavern 2 without work-overs (purple), (BGR, 2004c) 40
Figure 30: Utilization degree at different points in time, (BGR, 2004c) 43
Figure 31: Development of the fracturing criterion in time with the pressure cycles in red for cavern 1 and green for cavern 2, (BGR, 2004c) 43
Figure 32: Relation between extraction grade and subsidence rate after 100 years, for row configurations in dark blue, (BGR, 2003b) 44
Figure 33: Location of the Adolf van Nassau III mining permits and the Delfzijl plant 46
Figure 34: Cross sections through the Heiligerlee (a) (Oranjewoud, 2007) and Zuidwending (b) (Oranjewoud, 2008) brine fields 47
Figure 35: Portion of a triple row cavern field that is 3D modelled, with help of symmetry the entire field is built up by mirroring the yellow block, (BGR, 2002) 50
Figure 36: Pressure variation in time to simulate cavern development in the Heiligerlee brine field, (BGR, 2000) 51
Figure 37: Temperature functions in time for bottom (-1450 m) and top (-700 m) of modelled Heiligerlee caverns (BGR, 2000) 52
Figure 38: Subsidence rates resulting from varying the pillar width and creep properties in Zuidwending brine field (BGR, 2002) 54
Figure 39: Axisymmetric model of a single cavern for the Aardgasbuffer Zuidwending, (IfG, 2009) 55
Figure 40: 3D model of Aardgasbuffer Zuidwending (right), planned cavern field (upper left), approximation hexagonal field (middle left) and plan view of the selected portion of the field (lower left), (IfG, 2009) 55
Figure 41: Results after 10 years of storage operation for an operation scenario (1), (IfG, 2009) 58
Figure 42: 2D model with 4 caverns aligned in a row, (Atkins, 2012) 61
Figure 43: Map of depth of top Z1 Formation in the Haaksbergen salt pillow, (MWH, 2011b) 64

Figure 44: Map of thickness of Z1 Formation in the Haaksbergen salt pillow, (MWH, 2011b) 65
Figure 45: Profile through the Haaksbergen salt pillow, (MWH, 2011b)..... 65
Figure 46: Sketches of first (left, (IfG, 2010)) and second Haaksbergen model (right, (IfG, 2012a))..... 68
Figure 47: Subsidence prediction in m, used in the current mining plan for 12 Haaksbergen caverns, from KBB (2012) 70
Figure 48: Axisymmetric model of the base case 75
Figure 49: Boundary constraints applied to the single cavern model..... 76
Figure 50: Rotation of inclined layers in an axisymmetric model 77
Figure 51: Implementation of cavern development, (a) phase 0, (b) phase 5, (c) phase 10 and (d) zoom in on cavern wall of phase 10 with increasing pressure values with increasing depth 78
Figure 52: Implementation of the 'brinepressure' function 78
Figure 53: Time schedule of cavern development from 2015 to 2050, including image of cavern during phase 5..... 79
Figure 54: Implementation of the ‘temperature’ function..... 79
Figure 55: Converged cross-sectional area (blue) between year x (solid cavern contour) and year x+1 (dashed cavern contour) 81
Figure 56: Subsidence bowl profiles with cross-sectional area of subsidence bowl in year 20 in blue 82
Figure 57: Images of the different two cavern models with different pillar widths..... 83
Figure 58: Dimensions and mesh of calculation variant 057 with two caverns..... 84
Figure 59: Boundary constraints applied to a two cavern plane strain model 84
Figure 60: Time schedule of cavern development in a two cavern plane strain model including an image of the brine pressure acting on the cavern walls in phase 5 85
Figure 61: Best fit (dashed line) with the Haaksbergen creep rates (blue markers)..... 87
Figure 62: Single element creep test simulation in DIANA..... 88
Figure 63: Creep deformation resulting from the single element creep test simulation in DIANA..... 88
Figure 64: Results of the base case variant..... 90
Figure 65: Rate of cross-sectional convergence and ratio of cavern perimeter over cross-sectional area in the course of the model 91
Figure 66: Calculation example of volume calculation by rotation around an axis 91
Figure 67: Cross-sectional cavern area in year 10 (blue) overlapped by year 35 (red) 93
Figure 68: Location of nodes where vertical displacement was recorded 94
Figure 69: Vertical displacement of the nodes for models with 10 phases and 3 phases..... 95

Figure 70: Results of base case when run for 1000 years 96
Figure 71: Implementation of the 'lithostatic' function 97
Figure 72: Results of the base case with simulation of cavern sealing 98
Figure 73: Two models with small caverns situated in the top half of the salt deposit (left) and in the bottom half (right) 99
Figure 74: Results of the analysis with two small caverns 99
Figure 75: Results of the cavern diameter variants 101
Figure 76: Images of calculation variants with different cavern diameters, *D* = 75 m (left) and *D* = 175 m (right) 101
Figure 77: Results of the variants with different salt roof thickness 102
Figure 78: Results of the variant with different thickness of the salt floor 103
Figure 79: Results of cavern dimension variants with respect to the cross-sectional cavern areas in year 35 104
Figure 80: Zoom-in on the results presented in Figure 79 104
Figure 81: Results of the variants with different values of the creep parameter *A* 105
Figure 82: Results of the variants with different values for the stress exponent *n* of the creep law 106
Figure 83: Results of calculation variants with different values for the elasticity modulus of salt 107
Figure 84: Sensitivity analysis of salt properties 108
Figure 85: Creep test results of the Haaksbergen salt (blue markers), with a best fit (dashed black line), an upper (green line) and lower (red line) boundary 109
Figure 86: Division of the axisymmetric model into 5 units: cavern, salt, overburden, base, and subsidence bowl 110
Figure 87: Sensitivity analysis of the variation of the elasticity moduli of different geological units 111
Figure 88: Comparison of results of an axisymmetric and a plane strain analysis 113
Figure 89: Results of the variants with different pillar widths 114
Figure 90: Contours of left hand cavern of models with a pillar width of 225 m (red) and 300 m (green) 115
Figure 91: Images of stress redistribution around caverns, for small pillar width (left) and large pillar width (right) 115
Figure 92: Distribution of mean stress around caverns separated by a 175 m wide pillar in a linear elastic analysis, including the line for the stress profiles of Figure 94 and Figure 95 116

Figure 93: Distribution of mean stress around caverns separated by a 300 m wide pillar in a linear elastic analysis, including the line for the stress profiles of Figure 94 and Figure 95, stress scale equal to Figure 92 116
Figure 94: Profile of mean stress across 175 m wide pillar (blue) and 300 m wide pillar (green) in last time step (year 35) of nonlinear analysis 117
Figure 95: Profile of differential stress across 175 m wide pillar (blue) and 300 m wide pillar (green) in last time step (year 35) of nonlinear analysis 117

List of tables

Table 1: Subsidence prognosis parameter values of the Heiligerlee and Zuidwending brine field, the parameters in white rows were fixed, the parameters in blue rows were varied, (BGR, 2007) 26
Table 2: Material parameters of different geological layers of the row pillar model, (BGR, 2004b) 36
Table 3: Drucker-Prager parameters for Oberer Buntsandstein 1 and BGRa parameters for Röt salt, (BGR, 2004b) 36
Table 4: Calculation variants in in-line pillar study, (BGR, 2004c) 39
Table 5: Thickness and depth intervals in row and in-line pillar models, differences in blue shading 41
Table 6: Material parameters for Zuidwending field optimization study, (BGR, 2002) 52
Table 7: Minkley model parameters depending on plastic strain, (IfG, 2009) 57
Table 8: Minkley model parameters, (IfG, 2009) 57
Table 9: Material parameters of the geological layers in the model (Atkins, 2012) 62
Table 10: Literature strength parameters for rock salt used in the first Haaksbergen model, (IfG, 2010) 69
Table 11: Literature creep parameters for rock salt used in the first Haaksbergen model, (IfG, 2010) 69
Table 12: Strength parameters for rock salt used in the second Haaksbergen model, (IfG, 2012b) 69
Table 13: Creep parameters for rock salt used in the second Haaksbergen model, (IfG, 2012b) 69
Table 14: Base case parameters and values 72
Table 15: Calculation variants in single cavern analysis 73
Table 16: Assumed elastic material parameters for the geological units of the Haaksbergen field 80
Table 17: Fokker creep parameters for the Haaksbergen salt 80
Table 18: Calculation variants of the two cavern models 83
Table 19: Measured creep rates of the Haaksbergen salt, (IfG, 2012b) 86
Table 20: Volumes of cavern and subsidence bowl in year 10 and 35 92
Table 21: Cross-section cavern areas for year 10, 25 and 35 for standard mesh size and a finer mesh 93
Table 22: Cavern and subsidence volumes in year 10 and 35 for E_{Salt} = *10 GPa* and E_{Salt} = *60 GPa* 108
Table 23: Deformations in the model with different deformability of the overburden from year 34 to 35 110
Table 24: 3D volume calculations for the elasticity moduli variants 111
Table 25: Cross-sectional cavern and subsidence bowl areas in year 34 and 35 113

List of symbols

a	[-]	Scale factor in subsidence prediction
A	[m^2]	Area
A	[s^{-1}]	Salt specific parameter of BGR creep law
A_x	[m^2]	Area of surface x
ΔA	[m^2]	Difference in area
c	[Pa]	Cohesion in Mohr-Coulomb failure criterion
D	[m]	Cavern diameter
E	[Pa]	Elasticity or Young's modulus
E_x	[Pa]	Elasticity or Young's modulus of material x
f	[m/m^3]	Value of Fokker shape function for subsidence bowl
f_1	[-]	Material property in dilatancy boundary
f_2	[-]	Material property in dilatancy boundary
F	[N]	Force
G^K	[Pa]	Kelvin shear modulus
G^M	[Pa]	Maxwell shear modulus
h	[m]	Height
h_0	[m]	Initial height
Δh	[m]	Change of height
I_1	[Pa]	Normal stress invariant in Drucker-Prager model
I_σ	[Pa]	Normal stress invariant in dilatancy boundary and short term strength
II_S	[Pa]	Deviatoric stress invariant in dilatancy boundary and short term strength
J_2	[Pa]	Deviatoric stress invariant in Drucker-Prager criterion for shear failure
k	[day^{-1}]	Convergence rate
k	[Pa]	Material property in Drucker-Prager criterion for shear failure
k_φ	[Pa]	Material property in Drucker-Prager criterion for shear failure
K	[Pa]	Bulk modulus
K_0	[-]	Ratio of horizontal over vertical stress
m	[Pa^{-1}]	Minkley model relaxation parameter
n	[-]	Stress exponent in BGR creep law
n_{FRAC}	[-]	Fracturing criterion

$p_{hydrostatic}$	[Pa]	Hydrostatic pressure
p_i	[Pa]	Internal pressure in cavern
p_{lith}	[Pa]	Lithostatic pressure
p_{max}	[Pa]	Maximum operation pressure of a (storage) cavern
$p_{production}$	[Pa]	Production pressure
P	[m]	Pillar width
s	[m]	Subsidence in Eickemeier subsidence prediction model
r	[m]	Radius
r_i	[m]	Inner radius
r_o	[m]	Outer radius
R	[kJ/mol·K]	Gas constant
R_m	[kJ/mol·K]	Gas constant in convergence rate function
t	[day]	Time
T	[K]	Temperature
q_φ	[-]	Material property in Drucker-Prager criterion for shear failure
Q	[kJ/mol]	Activation energy
V_K	[m^3]	Convergence volume in Schober & Sroka function for convergence volume
$\dot{V}_P$	[m^3/day]	Production rate in Schober & Sroka function for convergence volume
V_x	[m^3]	Volume of body x
W_{Pillar}	[m]	Pillar width
x_K	[m]	x coordinate of cavern axis in Fokker shape function for subsidence bowl
y_K	[m]	y coordinate of cavern axis in Fokker shape function for subsidence bowl
y_{ss}	[day^{-1}]	Steady state convergence rate in Salt-subsid
y_0	[day^{-1}]	Transient convergence rate in Salt-subsid
z^u	[m]	Depth of cavern bottom
z^o	[m]	Depth of cavern roof

α	[-]	Material parameter in Drucker-Prager model
α_T	[K^{-1}]	Material parameter for temperature influence on elastic deformation
β	[-]	Strain exponent in Fokker's model for primary creep
β	[°]	Angle between horizontal and the cone determining the boundary of the subsidence bowl at surface
β_C	[-]	Transient convergence duration parameter in Salt-Subsid
B_0	[-]	Curvature parameter of dilatancy function of Minkley model
Γ	[-]	Value of gamma function of generalized factorial in Fokker shape function for subsidence bowl
δ	[-]	Shape adjustment factor in Fokker shape function for subsidence bowl
ε	[-]	Strain
$\dot{\varepsilon}_{cr}$	[s^{-1}]	Creep rate
ε_{ij}	[-]	Strain component acting in direction i on a plane perpendicular to the j-axis
ε_p	[-]	Plastic strain
ε_{vol}	[-]	Volumetric strain, sum of principal strains
ε_1	[-]	Major principal strain
ε_2	[-]	Intermediate principal strain
ε_3	[-]	Minor principal strain
η	[%]	Utilization degree
η^K	[Pa·day]	Kelvin viscosity
η^M	[Pa·day]	Maxwell viscosity
ν	[-]	Poisson's ratio
ξ	[-]	Time effects parameter in Fokker shape function for subsidence bowl
ρ	[kg/m^3]	Density
σ	[Pa]	Stress
σ_{eff}	[Pa]	Stress difference between major and minor principal stress in BGR creep law
σ_D	[Pa]	Uniaxial compressive strength
σ_{ij}	[Pa]	Stress component acting in direction i on a plane perpendicular to the j-axis
σ_m	[Pa]	Mean stress (average principal stress)

σ_{max}	[Pa]	Strength of rock salt in utilization degree method
σ_{max}	[Pa]	Maximum effective strength
σ_t	[Pa]	Tensile strength in Drucker-Prager criterion for tensile failure
$\sigma_{t,max}$	[Pa]	Maximum principal stress tangential to cavern contour
σ_1	[Pa]	Major principal stress
σ_2	[Pa]	Intermediate principal stress
σ_3	[Pa]	Minor principal stress
σ^*	[Pa]	Reference stress in BGR creep law
$\Delta\sigma$	[Pa]	See σ_{eff}
σ_ϕ	[Pa]	Curvature parameter of strength envelope of Minkley model
σ_ψ	[Pa]	Curvature parameter of dilatancy function of Minkley model
τ	[Pa]	Shear stress
φ	[°]	Friction angle in Mohr-Coulomb failure criterion

Appendices

Appendix A: Detailed diagram of the process of geomechanical modelling and subsidence prediction……I

Appendix B: Process of building and running a model using DIANA……II

1. Introduction

Akzo Nobel Salt B.V. (referred to as AkzoNobel, which is the brand name) produces a total of around 6 million tons of salt on a yearly basis at three different production sites, namely Hengelo and Delfzijl in The Netherlands and Mariager in Denmark. Salt is extracted as brine from the subsurface by application of a solution mining method. In the plants at the different production sites, the brine is purified, evaporated and further processed to produce high quality salt (NaCl). The major part of the produced salt is used as chemical transition salt for the production of base chemicals. Other applications are in the food-processing industry, agriculture, road de-icing and consumer salt.

1.1. Project motivation

AkzoNobel mines salt from different types of salt deposits. The brine that is supplied to the Hengelo site is extracted from a bedded salt deposit. The Delfzijl and Mariager plants are supplied with brine from domal salt deposits. A new brine field will be developed near Haaksbergen in the coming years to secure brine supply to the Hengelo plant for the coming decades. The salt deposit near Haaksbergen is a pillow salt deposit, which is an intermediate type between bedded and domal salt deposits.

A geological model, a geomechanical model, a field lay-out and a subsidence prediction form (among others) the basis of the production plan for the future Haaksbergen field. In the past years each, of these components have been updated when new information became available from, for instance, seismic exploration and an exploration well.

For the geomechanical model, initially a generic cavern design was made to establish a set of safe dimensions for the caverns (underground openings that are created when salt is leached). As many caverns as possible were then planned in the initial geological model. At the end of the process a subsidence prediction was undertaken. Subsidence above salt caverns is caused by the creep behaviour of salt induced by stress relief, that makes the surrounding salt tend to slowly ‘flow’ cavern inwards. This way the cavern volume is reduced and this volume reduction is called cavern convergence. The outcome of the initial subsidence prediction was unacceptably high to AkzoNobel, namely around 0.6 m after 50 years (KBB, 2010).

In the meantime the geological model had been updated, as well as the generic cavern design, the field lay-out and the subsidence prediction. A seismic survey and an exploration well gave more insight in the geometry of the salt deposit and the properties of the Haaksbergen salt, this served as input for the updates. Despite the fact that AkzoNobel now has a production plan for the first phase of the Haaksbergen brine field with an acceptable amount of subsidence, questions remained within AkzoNobel’s Mining Technology Department (MTD) about the way a geomechanical model and subsidence prognosis are made. An additional aspect is AkzoNobel’s lack of experience with the development of mining activities in a pillow salt deposit. Questions such as: ‘Does a salt pillow require a different approach in the process of geomechanical modelling and subsidence prediction?’ and “Which factors influence the outcome of a geomechanical model and a subsidence prediction significantly?” were raised. This formed the motivation for this MSc thesis.

1.2. Research questions

From discussions on AkzoNobel's problem description, the following two main research questions for this thesis were distilled:

1. Which fundamental differences in the approaches to geomechanical modelling of salt deposits can be distinguished and how do these differences influence the results?
2. What is relevant from this, regarding geomechanical modelling and subsidence prediction of the future operation in Haaksbergen?

Answering these questions requires mainly information from literature and consultant reports on the geomechanical models and subsidence predictions that are used by AkzoNobel at the moment. The modelling aspect of this work adds a third research question:

3. Which factors influence the convergence of a cavern in salt and the subsidence that results from this?

1.3. Objectives

From the research questions that were described in the previous section, the two following objectives were formulated:

1. Analyze and explain the geomechanical models and subsidence predictions that AkzoNobel currently uses in its salt operations by means of a literature study.
2. Develop a geomechanical model to investigate how variation of different parameters influences cavern convergence and subsidence.

An initial objective was to develop a 3D model that contained the twelve caverns of the first phase of the Haaksbergen brine field. In the course of this project, this turned out not to be feasible within a reasonable timeframe.

1.4. Thesis outline

This thesis starts with background information about salt deposits and solution mining (Chapter 2) followed by the background of geomechanical modelling and subsidence predictions in salt mining operations (Chapter 3). This basic information is used in Chapters 4 to 7 where the geology, mining details, geomechanical models and subsidence predictions of AkzoNobel's salt activities are discussed. Chapter 8 explains how the geomechanical models, that were made to achieve the second objective (see 1.3), were set up. The outcome of these models is presented and discussed in Chapter 9. This thesis ends with a chapter on conclusions and recommendations (Chapter 10).

2. Salt deposits and solution mining

In this chapter the origin of salt deposits and the solution mining method are explained. The first section of this chapter is dedicated to the geology of salt deposits. In the second section the basic principles of the solution mining method are explained.

2.1. Geology of salt deposits

The characteristics of salt deposits as they are found today are determined by geological factors. Examples of these characteristics are mineral composition and the size and shape of the deposits. This section is divided in three subsections. In the first subsection a description of the deposition process of salt is given. This deposition process leads to some properties of salt that are markedly different than other rocks. The second subsection is dedicated to a description of these and other properties of salt. As will be explained, salt has a higher deformability than other rocks and the ability to flow under certain conditions. This is of importance in the last subsection on salt tectonics that explains under which circumstances salt deposits of different geometries were formed.

2.1.1. Deposition of salt

A rock salt formation is a (part of an) evaporite deposit that consists mainly of the mineral Halite (NaCl). Evaporite deposits originate from a body of mineral-rich water that is in a semi-isolated basin. Ochsenius (1877) proposed the barrier-basin concept that describes the deposition process. The fractional sedimentation theory was built on Ochsenius' concept and is most often used to describe the formation of rock salt (Jeremic, 1994). This theory is described in the following 5 phases:

1. A basin is isolated from the sea by a barrier. During periods of high sea level, water from the sea overflows this barrier and enters the basin.
2. During a subsequent period of lower sea level, water from the sea will not be able to overflow the barrier. The mineral-rich water in the basin is isolated from the sea during this period. By evaporation of water the concentration of the minerals in the basin increases. This will continue until the solubility limit of the mineral with the lowest solubility is reached.
3. When the solubility limit of a mineral is reached, it will precipitate on the bottom of the basin. Due to the different solubility limits of the different minerals, the minerals will precipitate in a sequence of increasing solubility. In general, the first minerals to precipitate are carbonates and gypsum, followed by halite. The sequence is closed by potassium and magnesium salts. Figure 1 illustrates that evaporation of a 300 m high column of seawater results in 4.8 m of evaporites, of which 3.7 m is halite.
4. During the process of water evaporation and mineral precipitation, the sea level may rise and fall again, supplying new water from the sea. From the changing composition of the water in the basin, the precipitation of minerals continues as soon as the solubility limit of a mineral is reached. The continuous supply of seawater to the basin (recharge), facilitates the formation of thick layers of evaporite deposits. A prerequisite is that the rate of evaporation exceeds the influx of sea water.
5. Due to geological phenomena like uplift or marine regression, the basin can become permanently isolated from the sea. By erosion of surrounding rock materials the evaporite

deposits can be covered by a layer of sediments, that protects the evaporites from dissolving. This way the evaporite deposit is conserved.

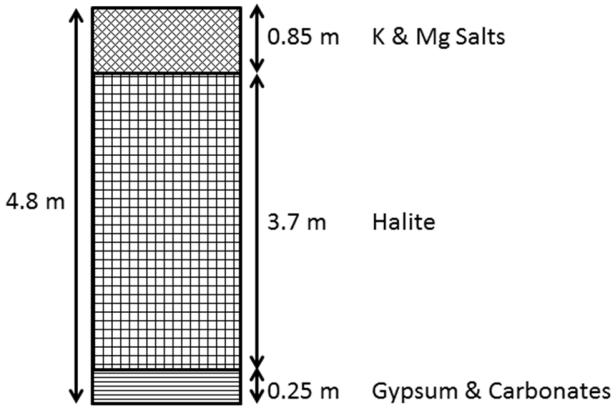

Figure 1: 4.8 m column of evaporites originating from a 300 m column of seawater, after Robertson Handford (1991)

The composition of an evaporite deposit corresponds to the mineral content of the sea water it originated from.

2.1.2. Salt properties

In the classification of rocks, rock salt belongs to the class of sedimentary rocks. But due to its way of deposition and its mineral composition, it has some properties that are distinct from other sedimentary rocks. Four properties are discussed here.

Sedimentation rate

Most sedimentary rocks are formed by deposition and accumulation of sediments, followed by compaction and cementation during diagenesis. Evaporites are a type of sedimentary rocks that are deposited by precipitation. The sedimentation rate depends on the conditions during precipitation and is in general much higher (up to 1000 times) (Schreiber & Hsü, 1980) than for other types of sedimentary rocks.

Deformation behaviour

Unlike most sedimentary rocks, rock salt does not deform in a brittle manner. Because rock salt has the ability to creep, it shows visco-elasto-plastic behaviour (Geluk *et al.*, 2003). Rocks that show brittle behaviour, show minimal deformation at increasing stress, until a maximum stress is reached and failure occurs. Creep behaviour is characterized by continuing deformation under a constant load. Therefore rock salt shows more deformation at increasing stress, but in general a state of failure (formation of fractures) is not reached.

Tightness

Rock salt formations usually have a very low porosity (0.1 to 1%) and low permeability (0.0001 to 0.01 millidarcy) (Jeremic, 1994). Therefore they are considered to be a very good flow barrier for instance for hydrocarbons. Besides the fact that rock salt formations can act as a 'seal' for oil and gas reservoirs, hydrocarbons and other fluids can also be stored in underground openings in rock salt.

Density

Rock salt has an average density of around $2.2 \cdot 10^3$ kg/m^3. This is in general higher than the density of unconsolidated sediments that lie close to the earth's surface and lower than the density of rocks that are situated at greater depths. Where the density of other sedimentary rocks increases with depth due to reduction of pore volume, the density of rock salt remains constant. When rock salt lies underneath for instance a sandstone formation that has a higher density of around $2.4 \cdot 10^3$ kg/m^3, it will have the tendency to migrate upwards. If there would be a discontinuity like a fault, rock salt has the ability to use this as an onset to slowly flow upwards. This gravitational flow movement of salt is called halokinesis, a term introduced by Trusheim (1957).

2.1.3. Salt tectonics

Salt deposits occur in various shapes and sizes. During the precipitation process, sequential layers of different minerals are formed. After burial, the evaporite deposits can be subjected to extensional as well as compressional regimes. These regimes govern halokinesis and result in shape-changes of evaporite deposits. The initial layered rock salt deposits can develop into salt pillows and subsequently into salt domes, due to the ability of salt to flow. These three types of deposits are discussed concisely below after Geluk *et al.* (2003) and they are sketched in Figure 2.

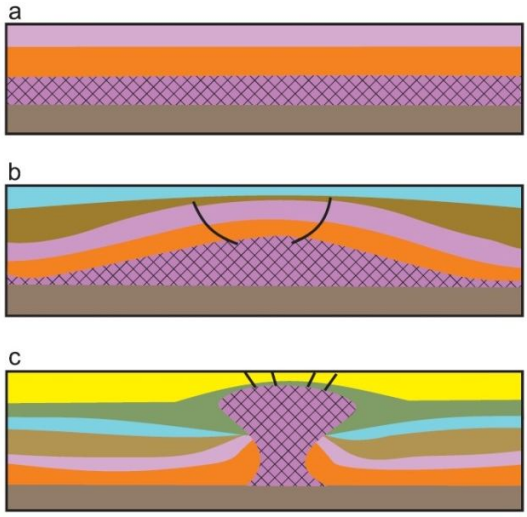

Figure 2: Bedded salt deposit (a), pillow salt deposit (b) and salt dome (c), (Geluk *et al.*, 2003)

Bedded salt deposits

Bedded salt deposits are more or less horizontal salt layers that reflect the conditions of their formation. The top and base of the salt layer are parallel and inter-bedded non-salt layers are parallel as well. Across a bedded salt deposit, the thickness of salt may vary and faulting can occur. However throughout the history of a bedded salt deposit there have been no factors that stimulated or allowed the salt to flow significantly.

Pillow salt deposits

A pillow salt deposit, is a bedded salt deposit that has developed a local thickening by mainly horizontal flow of salt. The opportunity for salt to accumulate in a certain location is usually created by faulting below the base of the salt deposits. Although accumulation of salt in the local thickening creates an extensional regime in the overlying beds, rock salt does not pierce through these layers during pillow formation, since the flow direction of salt is mainly horizontal in this stage (Lotze, 1957).

Domal salt deposits

During the formation of a salt dome, or salt diapir, the rock salt flows mainly in the vertical direction. Therefore the rock salt is able to pierce through the overlying layers. The debris that stay on top of the rock salt are called caprock and act as a battering-ram to create weakness zones in overlying layers (Jeremic, 1994), allowing the rock salt to flow further upwards. During dome formation, rock salt can flow up to the surface, but the flow can also terminate at depth. As is sketched in Figure 2 (c), the rock layers surrounding the dome are disintegrated by the formation process of the dome. Also the internal structure of rock salt that originally contained some inter-bedded layers can be disturbed to a severe degree.

2.2. Solution mining

Rock salt can be mined by application of a solution mining method. Water is injected into the salt formation via a well. In the salt formation the water dissolves rock salt to become brine. The brine is then transported to surface via the same well or another one. The cavity that is created is called a cavern. There are two modes of operation: top injection and bottom injection. Their characteristics, advantages and limitations are described in Geluk *et al.* (2003), a derived description is given here.

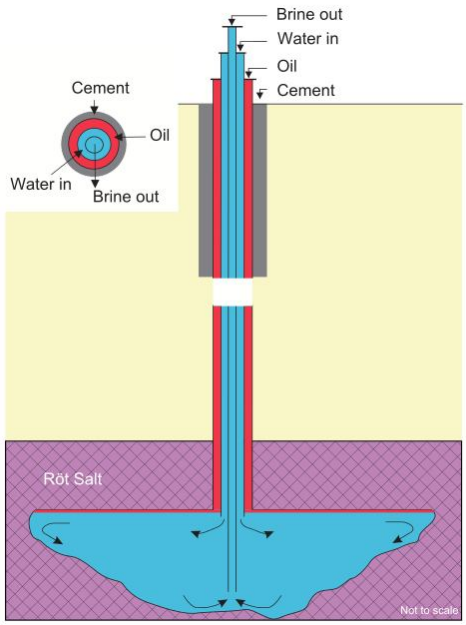

Figure 3: Schematic overview of a cavern and well operating in top injection mode (Geluk *et al.*, 2003)

The main characteristic of the top injection mode is that water is injected via the annular space between two production strings in the well. The water enters the cavern in the upper part. Brine is extracted via the inner production string that hangs near the bottom of the cavern, see Figure 3. Since brine has a higher density than the injected water, brine with the highest saturation will be at the bottom of the cavern. Producing brine with a high saturation limits evaporation cost in a later stage of the salt production process, because less energy is required to evaporate the water. On the other hand, due to temperature changes throughout the well, crystallization may occur that can clog the production string. The top injection mode is also known as the indirect circulation mode.

The bottom injection or direct circulation mode is characterized by the water injection via the inner production string that hangs lower than the outer production string via which the brine is extracted. It also applies to this mode that the brine with a higher salt content is at the bottom of the cavern. Since brine is extracted via the outer string that hangs higher than the inner string, weaker brine is produced.

In solution mining, usually bottom injection is applied during the first phase of cavern development. Later the operation mode is switched to top injection. In both operation modes the two production strings are hanging inside a cemented casing. Because of its lower density, water with low salt content will be in the upper part of the cavern, making vertical development of a cavern easier than horizontal development. To make sure the cavern also develops horizontally, a fluid is injected that floats on water and prevents contact between the water and the roof of the cavern. This forces the cavern to develop laterally. In most cases this fluid is oil. In Figure 3 it is illustrated that this oil sits in the annular space between the cemented casing and the outer production string.

In some salt operations caverns have more than one well. In the first phase of cavern development, there is no hydraulic connection between the wells. As soon as a connection is established one well functions as the injection well and another one as the production well (Jeremic, 1994).

Cavern development can be monitored with help of sonar equipment. A sonar tool that emits waves and records the echoed response is lowered into the cavern. When the travelling speed of waves in brine is known, the cavern dimensions can be derived from the measurements. To be able to do a sonar measurement, the cavern needs to be taken out of production. To have an idea on the volumetric development of a cavern during production, the flow from a cavern and brine saturation are measured. The maximum set of dimensions to which a cavern is allowed to develop is called the rock mechanical envelope. This is determined by geomechanical modelling before mining starts.

3. Foundations and principles of geomechanical modelling and subsidence predictions in salt solution mining operations

The mechanical behaviour of geological formations in the subsurface can be identified by means of a geomechanical model. Geomechanical models are often used in mining operations to gain insight in the response of a set of geological formations on the presence or creation of an underground opening. The maximum allowable dimensions at which stability of the underground opening can be guaranteed are usually based on the outcome of geomechanical models. This also applies to the caverns that are created during a salt mining operation.

In this chapter, first the foundations and principles of geomechanical modelling that are relevant in solution mining of salt are discussed. Starting with a section on the basic principles of rock mechanics, followed by sections on stress analysis and the characteristics of geomechanical modelling, the process of geomechanical modelling and its background are explained. The last subsection is dedicated to subsidence predictions in salt mining operations.

3.1. Rock mechanics

The basic principles of rock mechanics that are required to understand the concept of a geomechanical model are explained here. In the first subsection the terms stress and strain are discussed. This is followed by a subsection on elasticity and plasticity, where the difference between these phenomena is explained.

3.1.1. Stress and strain

Stress and strain are two important terms in rock mechanics. A stress σ is a force F divided by the area A on which the force is acting, see (Eq. 3.1).

$$\sigma = \frac{F}{A} \qquad \text{(Eq. 3.1)}$$

A body in the subsurface can be subjected to stresses of different origin. The overlying and surrounding rock mass cause a stress field. The excavation of an underground opening in a rock mass causes the stress field to change. Brady & Brown (2006) state that “excavating (or enlarging) any underground opening is mechanically equivalent to the application, or induction, of a set of forces distributed over the surfaces generated by the excavation.”

Strain is a change of dimensions relative to an initial dimension. An example is the measurement of the height of a rock sample in a lab test during which the sample is subjected to an increasing load that causes it to deform. The change of height Δh is measured and divided by the initial height h_0 to get a value for the strain ε, see (Eq. 3.2). So strain is a measure of deformation in a certain direction.

$$\varepsilon = \frac{\Delta h}{h_0} \qquad \text{(Eq. 3.2)}$$

When a material is subjected to a change of stress, it will deform as a reaction to this change. Different materials can show a different response to a change in stress. An equation that describes the relation

between stress and strain is called a constitutive law. Hooke's law (Eq. 3.3) is an example of a constitutive law (Brady & Brown, 2006).

$$\varepsilon = \frac{\sigma}{E} \qquad \text{(Eq. 3.3)}$$

(Eq. 3.3) shows that according to Hooke's constitutive law, strain is the division of stress by the elasticity modulus *E*, which is a material constant. Hooke's law is a simple constitutive law that describes a linear relation between stress and strain. Some materials show a non-linear response and therefore they require other constitutive laws.

3.1.2. Elasticity and plasticity

In rock mechanics, two kinds of deformation are distinguished: elastic and plastic deformation. An elastic deformation is reversible. This means that when a material has deformed elastically under a load, the material will return to its initial (undeformed) state after taking away the load. On the contrary, plastic deformation is irreversible. Once a material has deformed plastically it will not return to an undeformed state.

Figure 4 illustrates elastic and plastic behaviour in a stress-strain diagram. The different curves can be considered as examples of test results of strength test on rock samples. Starting from the initial situation with no stress and no strain (point A) the material starts to deform elastically. In the case of linear elasticity, stress and strain increase linearly (solid blue curve). When a material shows non-linear elasticity the curve that represents elastic behaviour is not a straight line in the stress-strain diagram. In Figure 4 the dashed blue line represents non-linear elastic behaviour.

It has been mentioned that elastic deformations are reversible, this is illustrated by the left hand dotted unloading-reloading curve in Figure 4. During a test, the rock sample can be unloaded by removing the applied stress at point B. The elastic reaction to unloading is that the strain returns to zero, as the stress does. After unloading, the sample is back in the initial situation (point A), this shows that elastic deformations are reversible.

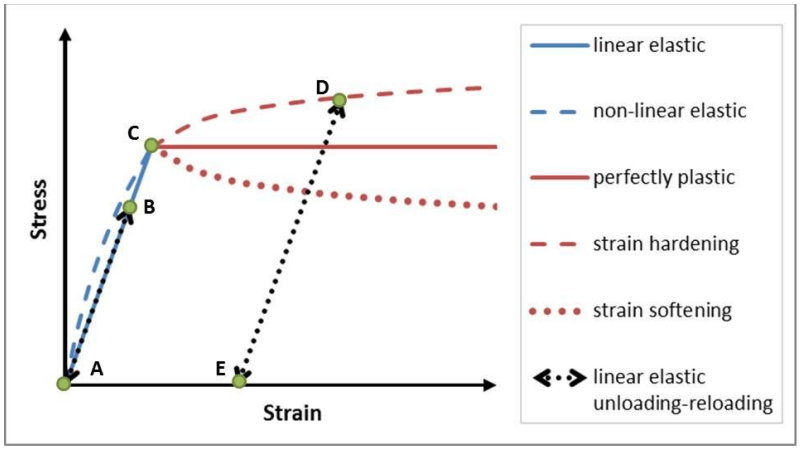

Figure 4: Sketch of elastic (blue) and plastic (red) behaviour with linear elastic unloading-reloading curves, after lecture notes 'Computer modelling of engineering materials' by M. Hicks (TU Delft)

The red curves in Figure 4 illustrate different types of plastic behaviour. At point C plastic behaviour starts. The solid red line represents perfectly plastic behaviour. The strength of the sample has been reached at point C. This means that any increase in stress beyond point C, results in an infinite amount of deformation. Two other types of plastic deformation are strain hardening (dashed red line) and strain softening (dotted red line). With strain hardening the material becomes stronger with increasing strain, for strain softening this is the other way around.

When some plastic deformation has already occurred, it is still possible to have an unloading-reloading cycle during a test. This is illustrated in Figure 4 with the right hand black dotted line. At point D the unloading starts, when the test is at point E all load has been removed. However not all deformations have recovered. This is because plastic deformation has occurred and this is irreversible. The amount of deformation that has been reversed is elastic deformation. The remaining deformation is plastic.

(Jeremic, 1994) describes the general deformation behaviour of salt. For salt there are two types of plastic deformation. The first type of plastic deformation is creep. Creep is a continuing deformation under a constant load. The basic difference in behaviour between materials with and without the ability to creep is illustrated with the very simple sketch in Figure 5.

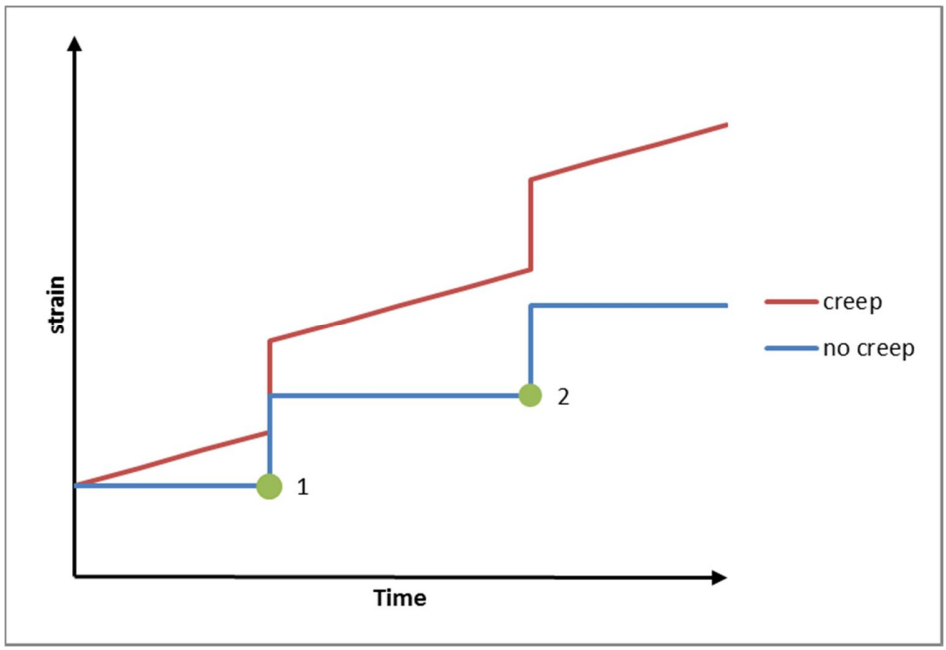

Figure 5: Basic difference in behaviour between creep and non-creep materials

The blue line represents a material that does not have the ability to creep, the red line represents a material that has the ability to creep. At two moments in time, indicated with the green dots labelled 1 and 2, the load on both materials is increased. For both materials this leads to an increase in strain. For the non-creeping material the strain remains at a constant level during the periods where the load is constant (between moments of load increment). In the red line it can be seen that the strain or deformation of the material that has the ability to creep, keeps on increasing during the periods of constant load.

The other type of plastic (irreversible) deformation is failure. In a state of failure fractures form under the prevailing stress state. An important difference between the two types of plastic deformation in salt mining is that creep always occurs. The amount of creep deformation depends on various factors like the temperature, load and salt specific properties, which will be discussed later. In contrast to creep deformation, failure does not always occur. Whether it occurs depends on salt specific properties and on the load to which salt is exposed.

3.2. Stress analysis

This section deals with the question how stress and strain are related and calculated. It is first explained how the magnitude and direction of stress are calculated. This is followed by a description of the material models that are used in geomechanical models of salt mining operations. A material model describes how a material deforms when it is subjected to a certain stress regime. When it is known how stress and strain can be calculated for certain materials, evaluation criteria are necessary to determine the boundary between acceptable and unacceptable stress states. The last subsection is dedicated to the evaluation criteria that are used to assess the outcome of geomechanical models of salt mining operations.

3.2.1. Stress components, principal stress and stress invariants

Brady & Brown (2006) describe how stress states can be expressed with respect to a chosen coordinate system. This is illustrated in Figure 6 in which all stress components that form a stress state are displayed. For example any stress σ_i on the top surface of the cube can be split into stress components in the *x*, *y* and *z* directions. The component of σ_i in the *z* direction is σ_{zz}, the one in the *x* direction is σ_{xz} and the one in the *y* direction is σ_{yz}.

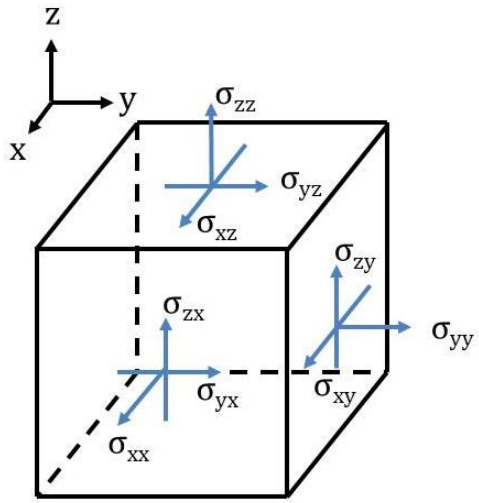

Figure 6: Components of stress acting on a cube in a Cartesian coordinate system

A stress matrix or tensor is a way to display a stress state. All components are incorporated in this matrix. (Eq. 3.4) shows how the stress components of Figure 6 are presented in matrix or tensor form.

$$[\boldsymbol{\sigma}] = \begin{bmatrix} \sigma_{xx} & \sigma_{xy} & \sigma_{xz} \\ \sigma_{yx} & \sigma_{yy} & \sigma_{yz} \\ \sigma_{zx} & \sigma_{zy} & \sigma_{zz} \end{bmatrix} \quad \text{(Eq. 3.4)}$$

This suggests that there are 9 independent components, but the moment equilibrium dictates that

$$\sigma_{xy} = \sigma_{yx} \qquad \sigma_{yz} = \sigma_{zy} \qquad \sigma_{zx} = \sigma_{xz} \quad \text{(Eq. 3.5)}$$

This changes the stress matrix into a matrix with six independent components instead of nine.

$$[\boldsymbol{\sigma}] = \begin{bmatrix} \sigma_{xx} & \sigma_{xy} & \sigma_{zx} \\ \sigma_{xy} & \sigma_{yy} & \sigma_{yz} \\ \sigma_{zx} & \sigma_{yz} & \sigma_{zz} \end{bmatrix} \quad \text{(Eq. 3.6)}$$

The stress components that act perpendicular to the surfaces are normal stress components. The ones that act along the surfaces are shear stress components. So σ_{xx}, σ_{yy} and σ_{zz} in (Eq. 3.6) are normal stress components and the others are shear stress components.

Since the choice of the orientation of the system of axes is arbitrary, it is possible to transform the stress components from a certain system of axes to a new orientation. If the orientation of the axes is chosen in such a way that the stress state can be expressed in normal stress components only, the axes are called the principal axes. The three remaining stress components are called principal stresses σ_1, σ_2 and σ_3. By convention σ_1 is the major principal stress, σ_2 is intermediate and σ_3 is the minor principal stress. Figure 7 illustrates the principal stresses in their system of axes, it is clear that there are only normal stresses and no shear stresses.

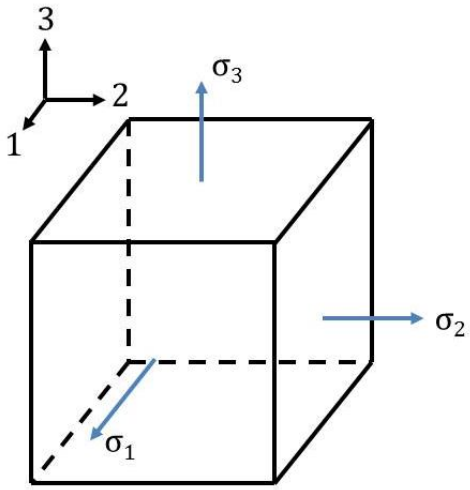

Figure 7: Principal stresses on a cube

To calculate a component of one stress state out of another, parameters are required that are independent of the orientation of the system of axes. The parameters that link any orientation of axes of any stress state with the corresponding principal stresses are called stress invariants. Because stress invariants are independent of the choice of axes, they are often used in the formulation of failure criteria.

3.2.2. Material models

Material models describe how materials behave under certain conditions. Some models only include (linear) elastic behaviour, some describe creep behaviour and others describe pre- and post-failure behaviour. In this subsection the material models are described that are regularly used in geomechanical modelling of salt solution mining operations.

Hooke's law

Hooke's law was mentioned earlier (see (Eq. 3.3) in section 3.1.1). It is used to represent linear elastic behaviour, not only for salt but also for other materials. The elasticity modulus that is the material parameter in Hooke's law is determined by results of strength tests on samples. Stress and strain are measured during the test. The gradient of the line that is the best fit of the measurements is the elasticity modulus E. This is illustrated in Figure 8.

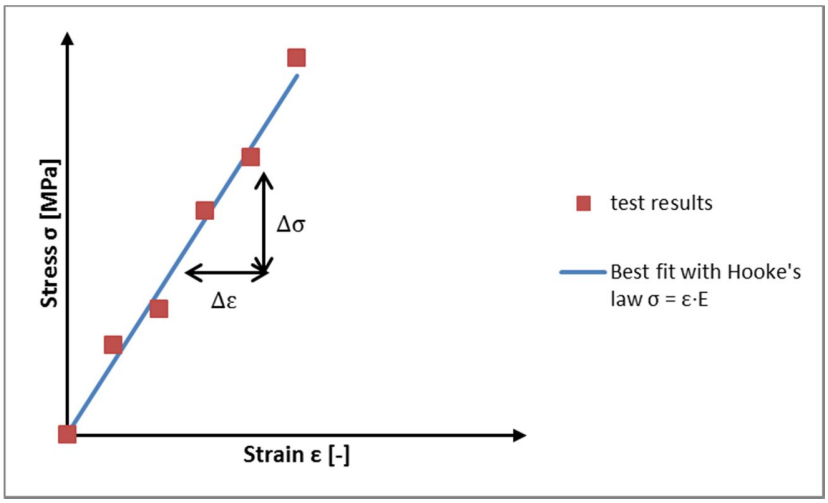

Figure 8: Hooke's Law's representation of elastic behaviour and fictional test results

Mohr Coulomb model

Mohr-Coulomb model is the name that is often used for the material model that is better referred to as 'linear elastic perfectly plastic'. It is a combination of linear elastic and perfectly plastic behaviour as indicated respectively by the solid blue and red lines in Figure 4. The point at which linear elastic behaviour ends and plastic behaviour begins, is determined by the Mohr-Coulomb failure criterion.

The Mohr-Coulomb failure criterion determines at which combinations of normal stress and shear stress failure occurs. During lab-tests on samples it is measured at which combinations failure occurs. A line can be plotted to get a best fit with the test results. Figure 9 illustrates this with fictional test results. The parameter c stands for cohesion. In the graph it is the intersection of the failure criterion and the shear stress axis. The angle φ is the friction angle and it is the slope of the line that represents the failure criterion. The equation of the failure criterion is (Eq. 3.7).

$$\tau = c + \sigma \tan \varphi \qquad \text{(Eq. 3.7)}$$

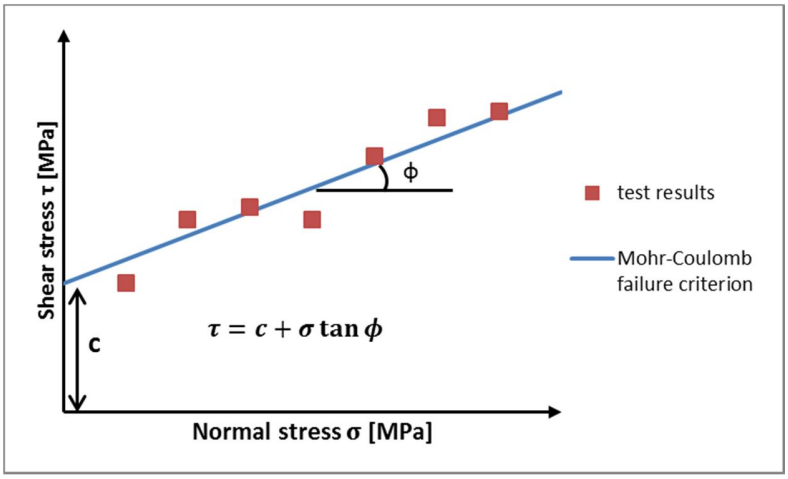

Figure 9: Mohr-Coulomb failure criterion and fictional test results

The Mohr-Coulomb model in this form is usually not applied to model salt behaviour. It is however used to model other, usually brittle materials that can overlay salt, as will be shown in later chapters.

Drucker-Prager model

The Drucker-Prager plasticity model (Drucker & Prager, 1952) was developed for materials that yield under shear loading. As will be shown later in chapters 4 to 7, this material model is used for materials that are often situated above salt deposits like anhydrite and claystone. In case the creep properties of the salt are very limited, it is also applied to salt. There are failure criteria for both shear (Eq. 3.8) and tensional (Eq. 3.9) failure.

$$\sqrt{J_2} = k_\varphi - \frac{q_\varphi}{3} I_1 \qquad \text{(Eq. 3.8)}$$

$$\frac{I_1}{3} \geq \sigma_t \qquad \text{(Eq. 3.9)}$$

The parameters J_2 and I_1 are deviatoric and normal stress invariants respectively. As described in 3.2.1 these stress invariants are independent of the chosen orientation of the system of axes and they are calculated from the principal stresses with (Eq. 3.10) and (Eq. 3.11).

$$I_1 = \sigma_1 + \sigma_2 + \sigma_3 \qquad \text{(Eq. 3.10)}$$

$$J_2 = \frac{1}{6}[(\sigma_1 - \sigma_2)^2 + (\sigma_1 - \sigma_3)^2 + (\sigma_2 - \sigma_3)^2] \qquad \text{(Eq. 3.11)}$$

The constants k_ϕ and q_ϕ in (Eq. 3.8) are material properties that can be determined from lab-test results. The constant σ_t in (Eq. 3.9) stands for the tensile strength of the material which can also be derived from tensile strength laboratory tests. Looking more closely at (Eq. 3.9) tells that tensile failure occurs when the average principal stress $I_1/3$ (See (Eq. 3.10)) is bigger than the tensile strength.

A graphic representation of (Eq. 3.8) is presented in Figure 10. Comparing this failure criterion to the above described Mohr-Coulomb criterion it can be learned from Figure 10 that the axes represent other parameters. The k_ϕ parameter is the intersection of the failure criterion and the $\sqrt{J_2}$ axis, like the cohesion c in the Mohr-Coulomb model. The gradient of the Drucker-Prager failure criterion is $q_\phi/3$. In

the Mohr-Coulomb criterion the slope is the friction angle φ. In some conventions the parameters have other symbols, for example k_ϕ can be just k, and $q_\phi/3$ is sometimes α.

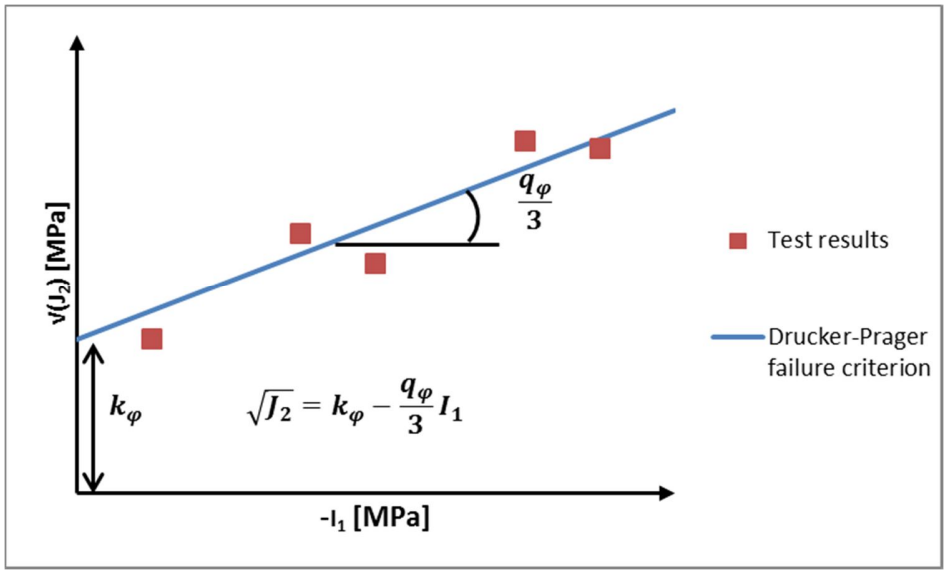

Figure 10: Drucker-Prager shear failure criterion and fictional test results

BGR creep model

The material model that Bundesanstalt für Geowissenschaften und Rohstoffe uses to model the behaviour of salt is referred to as the BGR creep model. It is a combination of Hooke's law for linear elastic behaviour and BGR's creep law (Eq. 3.12) (BGR, 2004a).

$$\dot{\varepsilon}_{cr} = A_1 \cdot e^{-\frac{Q_1}{RT}} \cdot \left(\frac{\sigma_{eff}}{\sigma^*}\right)^{n_1} + A_2 \cdot e^{-\frac{Q_2}{RT}} \cdot \left(\frac{\sigma_{eff}}{\sigma^*}\right)^{n_2} \qquad \text{(Eq. 3.12)}$$

With

$\dot{\varepsilon}_{cr}$	Creep rate	[d^{-1}]
A	Salt specific parameter	[d^{-1}]
Q	Activation energy	[kJ/mol]
R	Gas constant	[kJ/mol·K]
T	Temperature	[K]
σ_{eff}	Effective stress (difference between major and minor principal stress)	[MPa]
σ^*	Reference stress	[MPa]
n	Stress exponent	[-]

(Eq. 3.12) is often referred to as BGRb. Most often BGRb is applied with the value 0 for A_2, this reduces the complete second term to zero. The remaining first term is often referred to as creep law BGRa. The BGR creep model is only suitable to model stationary or secondary creep. This is creep with a constant creep rate.

To determine the values for these parameters for a specific salt deposit, creep tests are carried out on rock salt samples. During a creep test the value of σ_{eff} or $\Delta\sigma$ (the difference between axial and radial stress on the sample) is kept constant, the creep deformation is measured in time and the creep rate of each test is determined from this. In Figure 11 each of these (fictional) test results is displayed as a red square. The blue line is the best fit with these results with a certain set of values for the parameters A_1, n_1 and Q_1. For T the temperature at which the creep test was carried out has to be filled in. The gas constant R is a physical constant that has the value $8.314 \cdot 10^{-3}$ kJ/mol·K. The reference stress σ^* is 1 MPa.

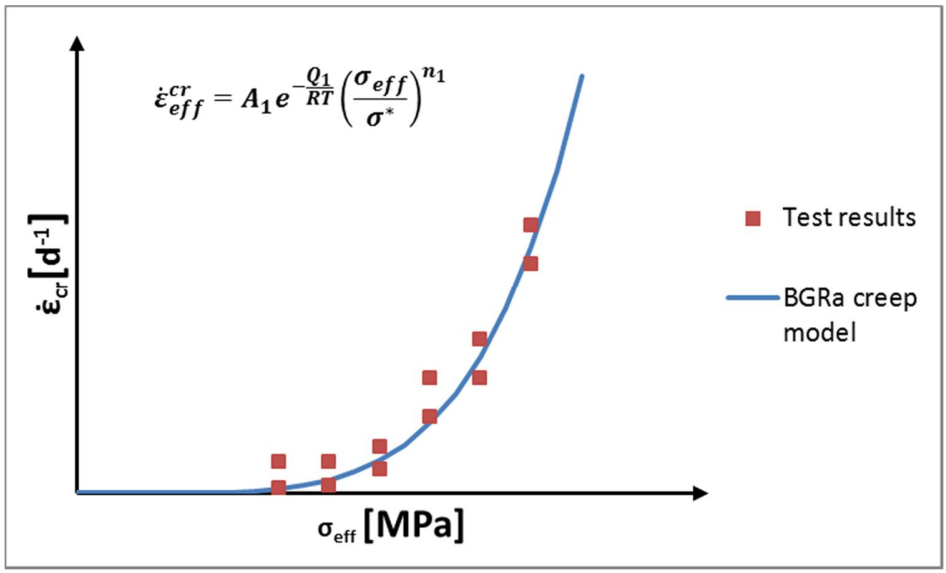

Figure 11: BGRa creep model and fictional test results

When BGRb is used with a non-zero second term, a more precise fit can be obtained. This gives a more accurate representation of the creep behaviour. However in a geomechanical model it is not always convenient to have a large number of parameters, because it increases the complexity of the model.

Fokker creep model

For secondary creep the Fokker creep model (Fokker, 1995) uses the same creep law as BGRb, see (Eq. 3.12). The extra element of the Fokker creep model is that it can also implement primary creep. Primary creep is creep that occurs just after a change of the load. So the effect of primary creep can be seen just after the start of a creep test when the loads have just been applied. This is illustrated in Figure 12 where the creep deformation during a fictional creep test is plotted against time. First the creep deformation increases rapidly, so the creep rate is high. Later on, the daily increase of creep deformation becomes constant (constant creep rate i.e. secondary creep).

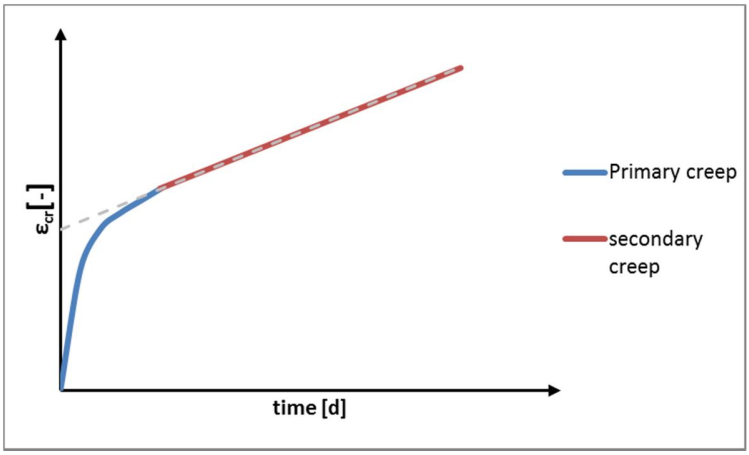

Figure 12: Sketch of fictional creep test results that show primary and secondary creep

In the equation that is used for primary creep, see (Eq. 3.13), it can be seen that primary creep does not only depend on the effective stress, but also on strain ε and the strain exponent β.

$$\dot{\varepsilon}_{cr} = A \cdot e^{-\frac{Q}{RT}} \cdot \left(\frac{\sigma_{eff}}{\sigma^* \cdot \varepsilon^{\beta}}\right)^{n} \qquad \text{(Eq. 3.13)}$$

Minkley model

The Minkley material model is a visco-elasto-plastic softening model (Minkley *et al.*, 2001) that was developed for salt and potash mining. A schematic representation of this model is shown in Figure 13.

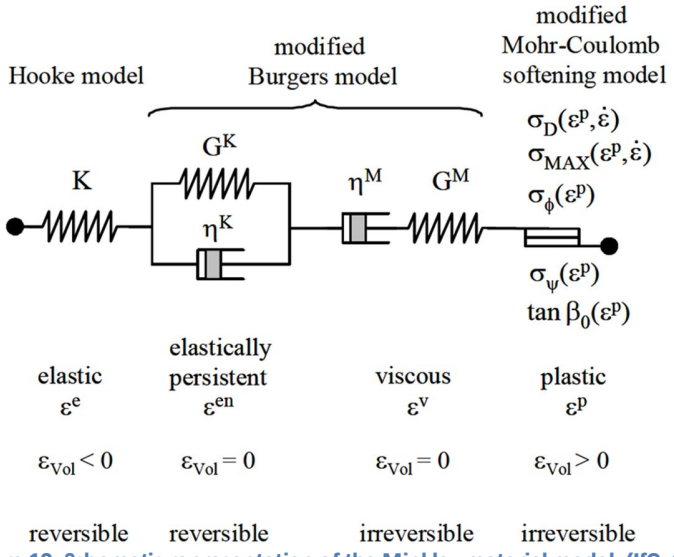

Figure 13: Schematic representation of the Minkley material model, (IfG, 2010)

IfG (2010) gives a brief description of the features of this model. It tells that linear elasticity is built into the model by implementation of Hooke's law. In the schematic representation this is the spring on the left hand side. The modified Burgers model consists of two parts. The first part is the Kelvin model that represents primary creep by a spring and dashpot in parallel. In the second part a dashpot and spring are in series. This is the Maxwell model that implements secondary creep into the Minkley model. Finally, a modified Mohr-Coulomb softening model represents tertiary creep in the model. When tertiary creep occurs, there is an acceleration in the creep rate that leads to failure (Jeremic, 1994).

3.2.3. Evaluation criteria

Evaluation criteria are used to assess whether the stress states that result from geomechanical modelling are acceptable or not. The evaluation criteria that are used in modelling studies of salt solution mining operations are discussed in this subsection.

Dilatancy boundary & short term strength

The dilatancy boundary and short term strength are often combined evaluation criteria, because they define the compressibility, dilatancy and failure behaviour of the rock salt. The concept of the dilatancy boundary (Cristescu & Hunsche, 1998) describes the stress states at which rock salt starts to dilate. The short term strength after (Hunsche *et al.*, 1994) is actually a failure criterion for rock salt. Since it is often used as an evaluation criterion in combination with the dilatancy boundary, it is discussed in this subsection.

Both the dilatancy boundary and the short term strength can be derived from triaxial strength tests on rock salt samples. In Figure 14 the course of the axial deformation during a fictional test is on the horizontal axis. The blue curve represents the volumetric strain during the test. Volumetric strain ε_{vol} is the summation of the three principal strains ε_1, ε_2 and ε_3. Just after the start of the test there is a negative volumetric strain which indicates that the sample is compressed. The stress state during this phase is therefore in the compressibility domain. After the volumetric strain has reached a minimum the sample starts to dilate. This minimum (green circle) is the at the dilatancy boundary. This means that at this point there is a transition from compression to dilation.

The red curve represents the differential stress (difference between axial and radial stress on the sample) and it is plotted with respect to the right hand vertical axis. The dilatancy boundary is reached at a differential stress that is indicated with the green dotted circle. Failure occurs at the end of the test, see orange circle. The corresponding differential stress is going to be a point on the short term strength curve.

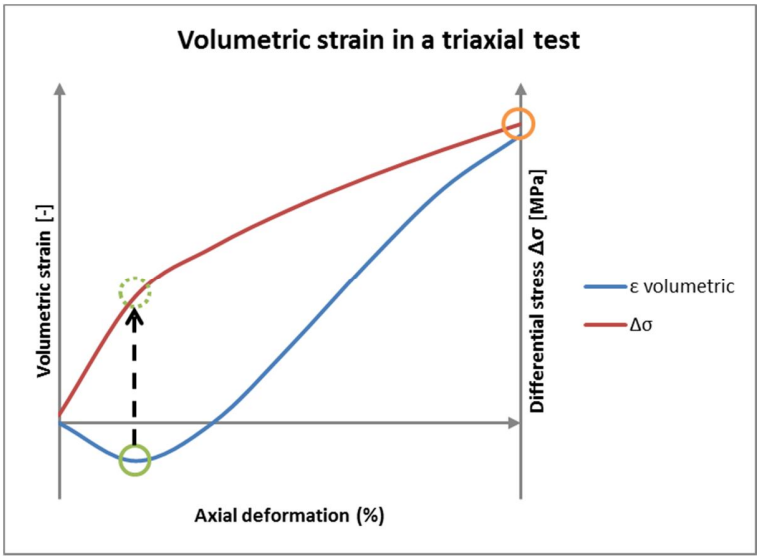

Figure 14: Curves of volumetric strain (blue) and differential stress (red) during a fictional triaxial test

The dilatancy boundary and short term strength curve are plotted in a diagram that has stress invariants on both axes, see Figure 15. Therefore the stress states at which dilatancy starts and at which failure occurs need to be converted to the corresponding normal and deviatoric stress invariants $-I_\sigma$ and $\sqrt{(II_S)}$. These points are indicated again with a green dotted circle and orange circle respectively. The other points can be viewed as results of tests on other samples of the same salt. A diagram that contains the dilatancy boundary and the short term strength curve, with the stress invariants $-I_\sigma$ and $\sqrt{(II_S)}$ on the axes is called an invariant diagram.

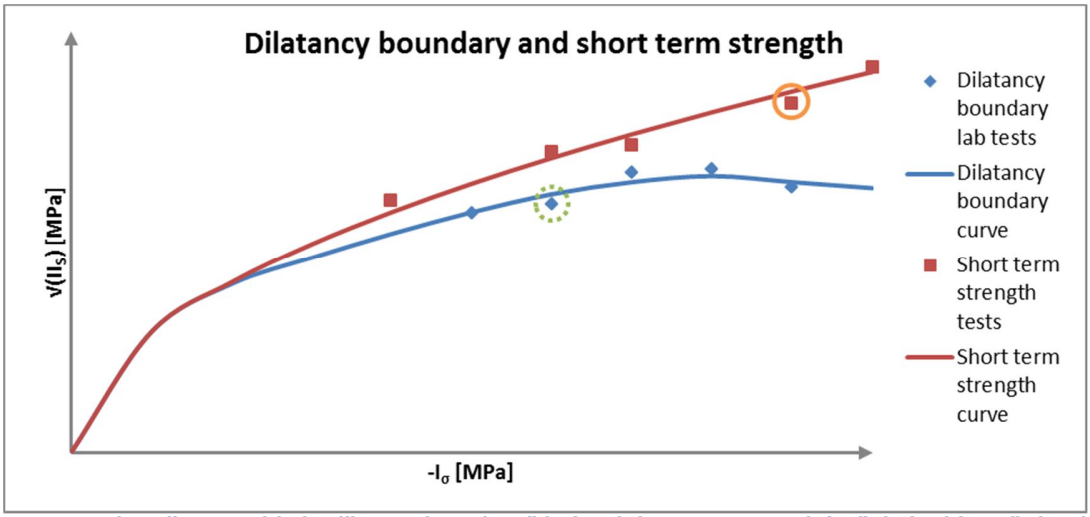

Figure 15: Invariant diagram with the dilatancy boundary (blue) and short term strength (red) derived from fictional test results

The equation for the dilatancy boundary is (Eq. 3.14).

$$\sqrt{II_S} = f_1 I_\sigma^2 + f_2 I_\sigma \qquad \text{(Eq. 3.14)}$$

By means of curve fitting the values of the salt specific parameters f_1 and f_2 can be determined.

The equation of the short term strength curve has more parameters, only the equation (Eq. 3.15) is given here. Reference is made to Hunsche *et al.* (1994) for more information on the parameters. Also here a best fit with the results of the lab tests is needed.

$$\sqrt{II_S} = -agh\left(\frac{|I_\sigma|}{\sigma^*}\right)^p \sigma^* sign(I_\sigma) + c \qquad \text{(Eq. 3.15)}$$

The area under the blue curve in Figure 15 is called the compressibility domain. All stress states under this curve only cause compression in salt. The area above the red curve is the failure area of the dilatant domain. Any stress state in this area leads to immediate failure. The area between the two curves is a transition area in the dilatant domain. At a stress state between these curves, salt is dilating. There is no immediate failure, but this can be expected on the longer term.

To use both curves as evaluation criteria, the stress states of elements in the model can be plotted in the invariant diagram. Every point that falls in the compressibility domain meets the evaluation criterion of the dilatancy boundary and the short term strength criterion.

Utilization degree or η-method

The η-method after Lux (1984)is an inverse safety factor. A safety factor is basically strength divided by stress. As long as the strength of a rock is bigger than the load that it experiences, the safety factor will be higher than one. In the η-method the load is divided by the strength. For example if it is set that the salt around a cavern may be loaded (or utilized) up to 30% of its strength, the η-value is 30%, see (Eq. 3.16). Where σ is the stress and σ_{max} the strength of the rock salt.

$$\eta = 100 \cdot \frac{\sigma}{\sigma_{max}} \qquad \text{(Eq. 3.16)}$$

If the stress states are plotted in an invariant diagram, and η = 30% is used as a criterion, the stress states would all have to be underneath an imaginary line at 30% of the red line in Figure 15. If the points that represent the stress states are under this line, the utilization degree criterion is met.

Fracturing criterion

The fracturing criterion is a very simple criterion that states that n_{FRAC} must be equal to or larger than 1, see (Eq. 3.16). This means that the internal pressure in the cavern p_i (in the brine) may never exceed the value of the minor principal stress σ_3. When p_i would be bigger than σ_3, fractures would be created at the cavern contour, making it less stable.

$$n_{FRAC} = \frac{\sigma_3}{p_i} \geq 1 \qquad \text{(Eq. 3.17)}$$

3.3. Geomechanical modelling

The steps that are generally taken in building, running and analyzing the results of a geomechanical model are described in this section first, followed by a description of different model types and their applications.

3.3.1. Process of geomechanical modelling

A flow diagram of the different components of a geomechanical modelling process is shown in Figure 16. It should be noted that this is a generalized flow-diagram. This means that any specific study can deviate from this diagram.

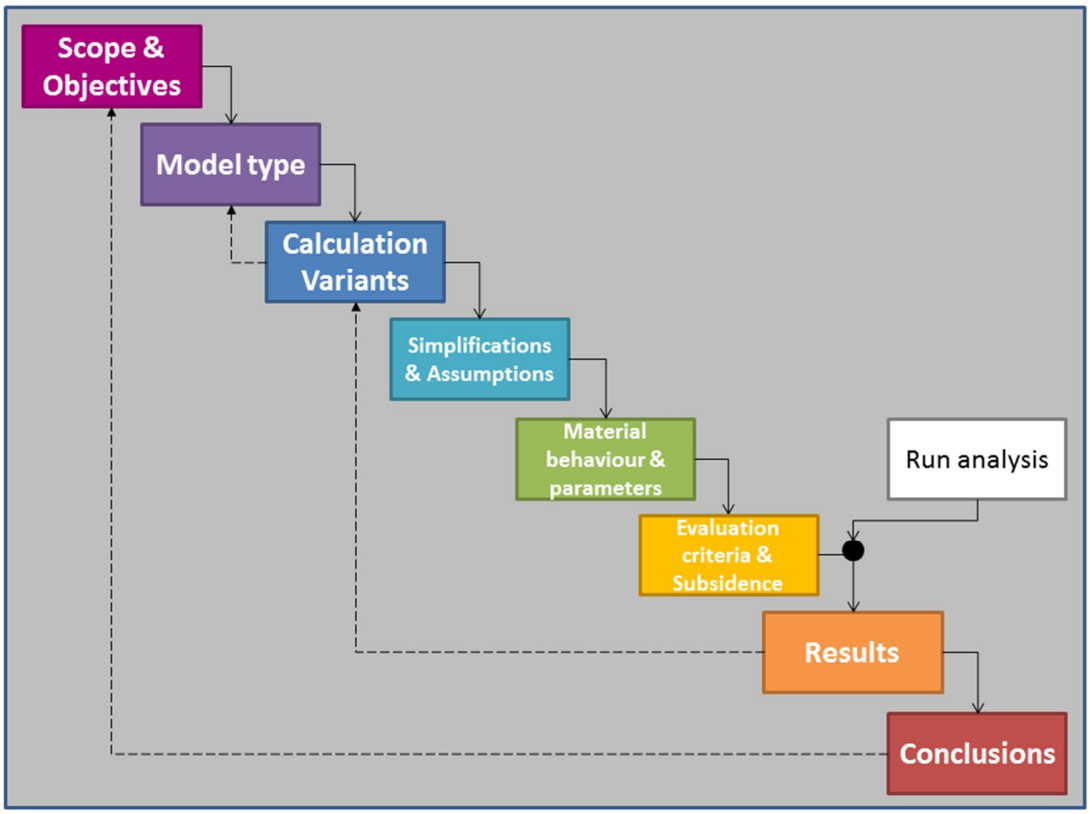

Figure 16: Flow diagram of the steps in a geomechanical modelling process

At the start of the process the scope and objectives are set. This way it is determined which answers or insights the work should provide and which aspects are taken into consideration and which are left out. The scope and objectives determine largely how choices are made later on in the process.

In the second step the model type that is most suitable to answer the questions is selected. Questions that are relevant here are:

- How many caverns need to be modelled?
- To which extent are symmetry axes present?

The calculation variants that will be modelled will all differ from each other in one or more aspects. The amount of variants and the way they differ depends largely on the objective of the study. For example

when the effect of the cavern diameter on stability needs to be investigated, different calculation variants will contain caverns with different diameters.

Simplifications and assumptions are usually implemented in the model to avoid to make an unnecessarily complex model that takes much time to run an analysis. An example of a simplification is to implement a geological layer that varies in thickness in practice, as a layer of constant thickness. An example of an assumption is to assume a constant temperature.

In the material behaviour and parameters step it is decided which material models will be used to calculate the response of a material to a certain stress. These material models require input parameters that are representative for the specific materials.

Evaluation criteria have to be set to decide whether certain stress conditions are acceptable or not. Also a method to implement a subsidence prediction needs to be established (if this is required from the scope and objectives of the study).

After running the analysis for the different calculation variants, in the final steps of the process the results are compared. Sometimes a new calculation variant is necessary. The conclusions of the comparison are drawn and often recommendations for further research are made.

In Appendix A the different aspects of each step are presented in a diagram. The descriptions in chapter 4 to 7 of the geomechanical models that AkzoNobel uses currently, follow the structure of this diagram.

3.3.2. Model types

It is important to discuss the different types of models and the corresponding characteristics to understand why a specific type of model is chosen for a certain purpose. The descriptions in this subsection are derived from DIANA (2011).

Plane Strain

The plane strain model owes its name to its characteristic that all strain components in the direction perpendicular to the plane in which the 2D model is drawn are zero. Usually the model is drawn in the *x*-*y* plane implying that strain components in the *z* direction are zero. The elements do not have a thickness in the *z* direction, because they are assumed to be infinite in this direction. This model type is therefore very suitable to model structures that have a very large dimension in the *z* direction compared to the *x* and *y* direction, like a tunnel. All loads in the model have to act in the *x*-*y* plane.

A cavern that would be modelled in a plane strain analysis would be infinitely long, which is not the case in practice. However, this implies that this approach to model one or more caverns is very conservative. If the outcome of the analysis is acceptable, then it is shown in a very simple way that the design meets the evaluation criteria.

Axisymmetric (2.5D)

An axisymmetric model is built in 2D, like the plane strain model. Also here, all loads have to act in the *x*-*y* plane. One of the axes in the model is the rotation axis. The elements in the model are axisymmetric

and form ring-like elements when they are rotated around the axis. This type is very suitable to model objects with a circular cross-section, for instance storage tanks.

Modelling a cavern in an axisymmetric analysis is more realistic than in a plane strain analysis, because rotation around the axis results in the actual shape of the cavern, rather than an infinitely long tunnel. For this reason, the model gives more realistic (less conservative) results. This way a more optimal design for the dimensions of the cavern can be calculated. It is however only suitable to model a single cavern, because a second cavern in the model would become a ring-like tunnel when it is rotated around an axis. Apart from this, a large degree of symmetry, of for example the geology, is required, to be able to make a realistic representation of the geological situation.

3D

A 3D model can be used for any purpose. It is built in 3D and loads can be applied in any direction. The elements in the model are defined by nodes that have *x*, *y* and *z* coordinates and are therefore neither infinitely long in a direction, nor rotated around an axis to form ring-like elements. 3D elements produce large systems of equations, making a 3D analysis very time-consuming. For this reason they are only used when the other types of models are not suitable. Sometimes a 3D model is built of a part of the area of interest, this part needs to be representative or for example mirror-symmetric with respect to the rest of the area.

The three types of geomechanical models were discussed in order of increasing complexity. This means that in this order the time to build a model increases, as well as the required calculation time to run an analysis. If a plane strain model can prove that a certain design of a cavern, or cavern field matches the criteria for stability and/or subsidence, a plane strain analysis should be undertaken. This requires the least time and therefore it costs the least money, and still it meets the criteria. On the other hand it is a conservative approach. With a more sophisticated axisymmetric or 3D model it is possible to prove that a design with a higher extraction grade would be possible (bigger caverns or narrower spacing) that still meets the criteria.

3.4. Subsidence prediction

Currently two analytical methods are in use to predict subsidence caused by AkzoNobel's salt mining activities. The subsidence predictions for the Heiligerlee and Zuidwending brine fields are carried out by the BGR who implemented the Eickemeier model into their own software. For the Hengelo brine field and also the future Haaksbergen brine field, the analytical subsidence prediction implemented in software called Salt-subsid was used. These methods show some differences and some similarities that will be discussed. Here, both methods will be referred to as the BGR and Salt-Subsid methods respectively. The BGR method will be explained to quite a detailed extend in subsection 3.4.1. In subsection 3.4.2 the similarities and differences with the Salt-subsid method will be discussed.

It has to be noted here that, although analytical subsidence predictions are generally accepted in salt solution mining, it is also possible to do a numerical subsidence prediction. This is common in the oil and gas industry, for example Kenter *et al.* (1998).

3.4.1. BGR method

The BGR method of subsidence prediction is used to predict subsidence over the Heiligerlee and Zuidwending brine fields. It is incorporated in a 5 year cycle of measuring surface subsidence, fitting the parameters of the Eickemeier model to match the results to come to an updated subsidence prediction that is in line with the latest measurements. At the moment AkzoNobel is in the second cycle of updating the prognosis.

The Eickemeier model that forms the basis of the subsidence predictions consists of three aspect. This can be seen in (Eq. 3.18) for the predicted subsidence (*s*) in place (*x*,*y*) and time (*t*) for a single cavern (Eickemeier, 2005).

$$s(x,y,t) = a \cdot f(x,y) \cdot V_K(t) \qquad \text{(Eq. 3.18)}$$

The factor *a* determines the portion of each cubic meter of cavern volume reduction that contributes to the subsidence bowl at surface, so *a* ranges between 0 and 1.The function *f(x,y)* is the unit shape function of the subsidence bowl that determines the subsidence at every combination of *x* and *y* coordinates. The function $V_K(t)$ is the convergence volume that changes over time and depends on the convergence rate.

The unit shape function *f(x,y)* that represents the general form of the Gaussian bell curve is taken from the Fokker subsidence model (Eickemeier, 2005). The function is given by (Eq. 3.19) that represents the bell shaped curve.

$$f(x,y) = \frac{\xi \cdot \delta}{2 \cdot \pi^{\left(1-\frac{2}{\delta}\right)} \cdot R^{\frac{4}{\delta}} \cdot \Gamma\left(\frac{2}{\delta}\right)} \cdot \exp\left(-\pi \cdot \xi^{\frac{\delta}{2}} \cdot \frac{((x-x_K)^2 + (y-y_K)^2)^{\frac{\delta}{2}}}{R^2} \right) \qquad \text{(Eq. 3.19)}$$

Where

$$R^2 = z^u \cdot z^o \cdot \cot^2 \beta \qquad \text{(Eq. 3.20)}$$

The parameters and units in these formulas are listed below. Figure 17 illustrates the physical meaning of the parameters.

$f(x,y)$	Value of bell curve at location x,y	[m/m^3]
ξ	Time-effects parameter	[-]
δ	Shape adjustment factor	[-]
$\Gamma(x)$	Gamma function that represents the generalized factorial	[-]
x_K	x coordinate of cavern axis	[m]
y_K	y coordinate of cavern axis	[m]
x	x coordinate of desired location	[m]
y	y coordinate of desired location	[m]
z^u	Depth of cavern bottom	[m]
z^o	Depth of cavern roof	[m]
β	Angle between horizontal and the cone determining the boundary of the subsidence bowl at surface	[°]

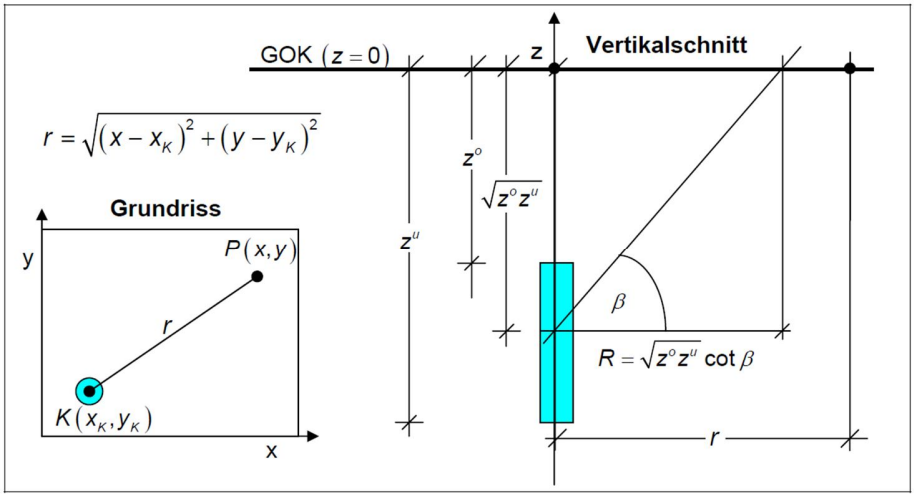

Figure 17: Illustration of parameters used in the unit shape function, as a plan view (left) and cross section (right), (BGR, 2006)

When δ = 2 and ξ = 1 the unit shape function is equal to the one in the Schober & Sroka model (Eickemeier, 2005).

The volume convergence function $V_K(t)$ of a cavern gives the development of the convergence volume in time and was taken from the Schober & Sroka model (Eickemeier, 2005). Since salt mining activities are considered, only the convergence volume function during leaching is shown here (Eq. 3.21), from BGR (2006).

$$V_K(t) = \dot{V}_P \left(t - \frac{1}{k}(1 - \exp(-k \cdot t)) \right) \qquad \text{(Eq. 3.21)}$$

$V_K(t)$	Convergence volume in time	[m^3]
$\dot{V}_P$	Production rate	[m^3/day]
k	Convergence rate	[day^{-1}]
t	time	[day]

The unit of time is chosen as days, any other time unit could have been chosen as long as it is used consequently.

A formula to determine the convergence rate for cylindrical caverns has been developed by Bérest *et al.* (2001) in which the creep law BGRa can be recognized, see (Eq. 3.22)

$$k = \sqrt{3}\left(\frac{\sqrt{3}\cdot(p_{lith}-p_i)^n}{n\cdot\sigma^*}\right)A\cdot\exp\left(-\frac{Q}{R_m T}\right) \qquad \text{(Eq. 3.22)}$$

k	Convergence rate	[day^{-1}]
p_{lith}	Lithostatic pressure	[MPa]
p_i	Internal cavern pressure	[MPa]
n	Stress exponent	[-]
σ^*	Reference stress	[MPa]
A	Salt specific creep factor	[day^{-1}]
Q	Activation energy	[kJ/mol]
R_m	Gas constant	[kJ/mol/K]
T	Temperature	[K]

Since this formula contains some depth-dependent input parameters (p_{lith}, p_i and T), it is advised to divide cylindrical caverns with a large height into units that all have a reference depth (BGR, 2006). The lithostatic and internal pressure and the temperature are calculated for this depth. These values are representative for the corresponding units of the cavern.

With this method, the subsidence bowl that each cavern causes is calculated. With the software ProSub the subsidence bowls that all caverns are causing at their specific locations are added to get the subsidence bowl of the entire brine field. For comprehensive visual presentation, the contour lines of the subsidence bowl are usually plotted on a topographical map with help of a Geographic Information System (GIS), in this case this is done with Tecplot.

To be able to update subsidence predictions with measured subsidence, BGR developed the software FitPar. With this program the input parameters of the subsidence prediction can be fitted to match the measurements applying the least square method. This has been done for both the Heiligerlee and Zuidwending brine field. Not all parameters were varied to get the best fit, 2 out of 7 were varied, the other 5 remained fixed, see Table 1 (BGR, 2007).

	Heiligerlee	**Zuidwending**
a [-]	0.95	0.95
β [°]	45	45
ξ [-]	1.0	1.0
δ [-]	1.923	1.833
A [day^{-1}]	0.5094	0.3618
Q [KJ/mol]	54	54
n [-]	5	5

Table 1: Subsidence prognosis parameter values of the Heiligerlee and Zuidwending brine field, the parameters in white rows were fixed, the parameters in blue rows were varied, (BGR, 2007)

3.4.2. Salt-subsid method

The Salt-subsid method is in many aspects similar to the BGR method. It also uses the factor *a* that determines the portion of subsurface volume loss that is translated to surface. However, Salt-subsid offers different options for the unit shape function. The unit form function that is described in the BGR method is among the options. The volume convergence function differs from the one in the BGR method. It is expressed as the following (RESPEC, 2010a)

$$C(t) = y_{ss}t + y_0(1 - \exp(-\beta_C t)) \qquad \text{(Eq. 3.23)}$$

$C(t)$	Convergence volume in time	[m^3]
y_{ss}	Steady state convergence rate	[day^{-1}]
t	time	day
y_0	Transient convergence rate	[day^{-1}]
β_C	Transient convergence duration parameter	[-]

The feature that it is possible to have a steady state and a transient volume convergence makes this method more advanced. However, in the BGR method the convergence rate is directly related to the creep law, which makes it possible to put creep parameters determined from lab tests into this model. In the Salt-subsid method it is always required to work with a convergence rate that is often calculated, instead of creep properties that are derived from measurements.

Just like in the BGR method it is possible to divide caverns into units and assign different parameters to the units. Also Salt-subsid is able to fit parameters on basis of measured subsidence using the least square method. So it offers the possibility to update a subsidence prediction based on measurements.

A big advantage of using Salt-subsid is that is does not only give the amount of subsidence and the subsidence rate as an output. It is also able to calculate horizontal and vertical strains and tilt. These quantities are often used so assess the possibility of damage to infrastructure and buildings at surface.

Besides this, Salt-subsid also has options to display results graphically in 2D and 3D. So everything can be done in one environment, where the BGR method uses 3 different codes (ProSub, FitPar and Tecplot).

4. Hengelo brine field

In the following chapters (4 to 7) the geology, mining method, geomechanical model and subsidence prediction of AkzoNobel's current brine fields will be discussed. The general information from chapters 2 and 3 will now be applied to the salt mining operations in Hengelo, Delfzijl and the future brine fields of Cheshire (potentially) and Haaksbergen (certain). AkzoNobel also operates a brine field in Mariager Denmark. Both from a geological and mining technology point of view, this brine field is similar to the Delfzijl brine fields. Therefore it wouldn't add value to this thesis to elaborate on the Mariager brine field.

Production from the Hengelo brine field started in the nineteen thirties, when the original salt evaporation plant in Boekelo was moved to a site in Hengelo along the Twentekanaal that was constructed at the same time. The brine field has developed over the years and at the moment it is mainly situated in the municipality of Enschede. Figure 18 gives an overview of the location of AkzoNobel's mining permits in the Twente region. Currently, salt is mined from the Twenthe-Rijn, Uitbreiding Twenthe-Rijn and Twenthe-Rijn Helmerzijde permits. These mining permits belong to the Hengelo brine field. The future Haaksbergen brine field will be developed in the Isidorushoeve mining permit.

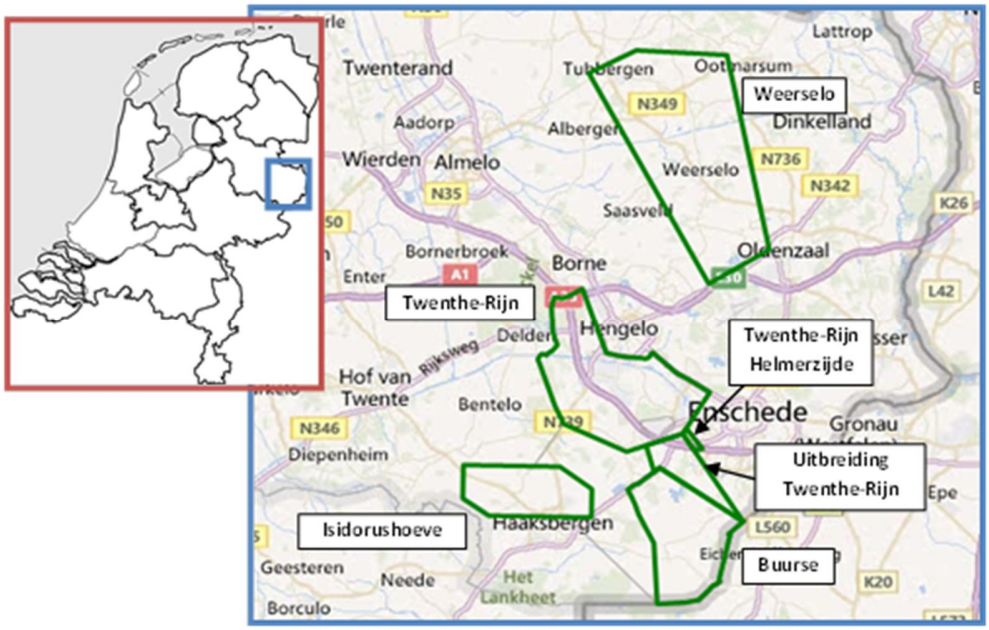

Figure 18: Location of AkzoNobel's mining permits in Twente in 2012

4.1. Geology

In the Hengelo brine field, salt is mined from the bedded Röt salt Formation (Upper Buntsandstein) which is part of the Upper Triassic. Its average thickness is 50 m and the depth of the layer varies between 350 and 425 m. The Röt evaporites are situated on top of the Solling claystone and start with the so-called base anhydrite. On top of the base anhydrite four salt layers have been deposited (A, B, C and D). The salt layers are separated by layers of claystone that contain some anhydrite. Salt layer A is

the deepest and most important layer because it has a high purity and it is 25 to 30 m thick. The salt deposit is inclined 6° SSW (AkzoNobel, 2003).

Above the evaporites there is a 180 m thick claystone layer called the Upper Röt Claystone, that contains some gypsum and anhydrite layers. On top of this, the limestone and dolomite of the Muschelkalk Formation can be found varying in total thickness from 0 to 100 m in the area. The Muschelkalk Formation is separated from the overlying Tertiary deposits by the Base Tertiary Unconformity. The Tertiary deposits consist of 70 to 110 m of unconsolidated claystone of the Dongen Formation dating from the Eocene. A second unconformity separates the 10 to 40 m thick Quarternary clays and sands from the Tertiary deposits (AkzoNobel, 2003).The geology of the Hengelo brine field is illustrated with a West-East cross-section in Figure 19. The thickness in the cross section may differ from the above mentioned values which are average thicknesses.

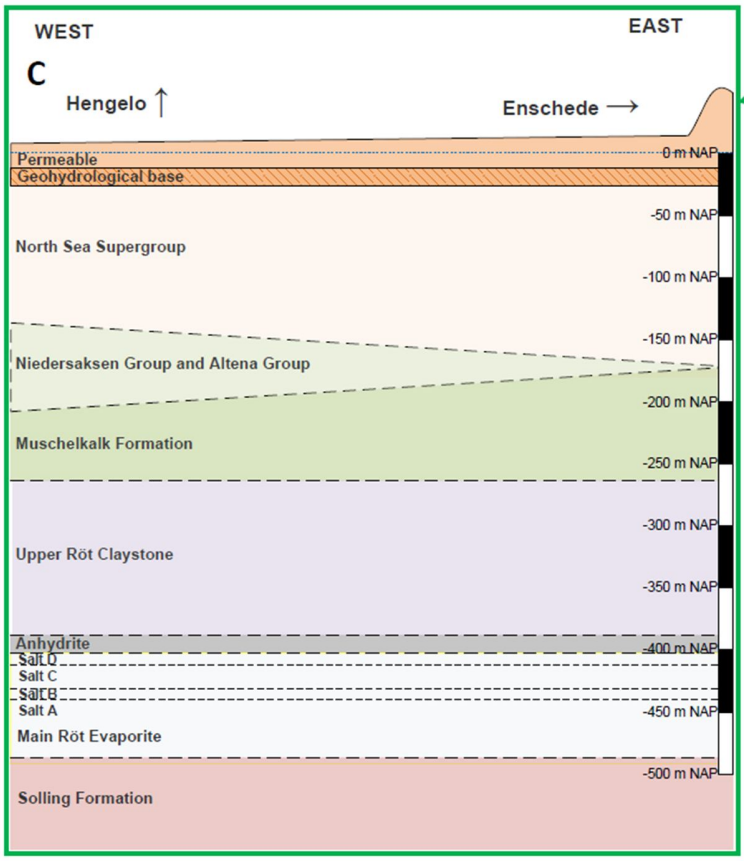

Figure 19: Cross section of the geology of the Hengelo brine field, (Drost, 2012)

4.2. Mining

Since the nineteen thirties the development of caverns has changed due to increasing knowledge and experience in the leaching process as well as technological improvements. The caverns in the Hengelo brine field can be divided into four categories that are illustrated in Figure 20.

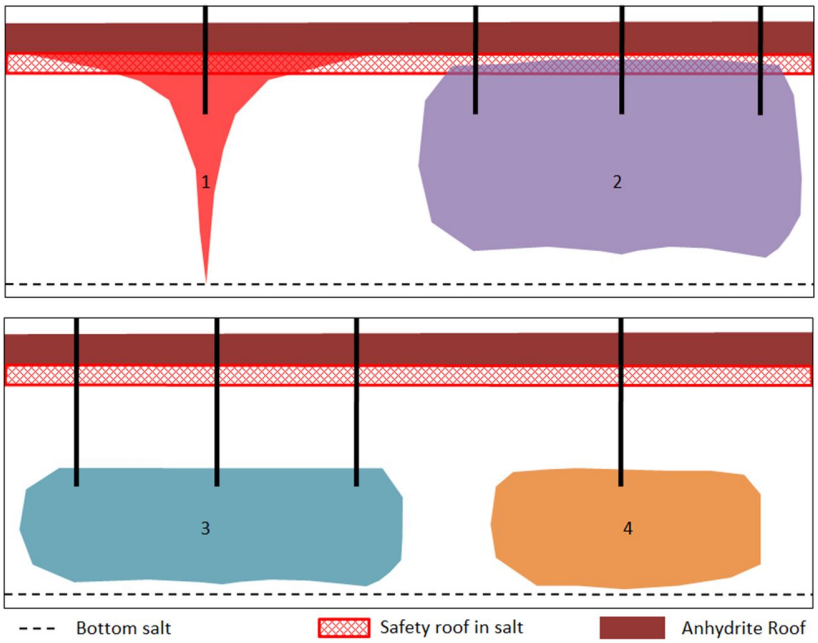

Figure 20: Four cavern categories in the Hengelo brine field: (1) Early SCCs, (2) Early MCCs, (3) Modern MCCs, (4) Modern SCCs

Caverns of the first category were developed up to the end of the nineteen fifties. They were developed with a single well (Single Completion Caverns, or SCCs). Since there was no technical solution available to stimulate the horizontal development rather than vertical, the caverns soon reached the top of the salt deposit. Here they started to develop laterally and hydraulic connections were created between neighbouring caverns.

In the development of the second category caverns, in the nineteen sixties and seventies, the fact that caverns could make a hydraulic connection was used to upgrade recovery. Multiple wells (two or three) were drilled per cavern (Multi Completion Caverns MCCs). After a hydraulic connection was established, one of the wells was used for injection, the other for production. This way the salt between the wells could be mined more efficiently. Especially when blanket oil was introduced, as mentioned in 2.2. The caverns were developed as large as possible and no safety roof was left behind in the salt layer.

In the transition from caverns of category 2 to 3, the concepts of a 5 m safety roof and 'inherently safe' caverns were introduced. This limited the height to which a cavern was allowed to develop. The concept of an inherently safe cavern takes into account that when the roof of the cavern collapses, the bulking factor of the consolidated overburden guarantees that an upwards migration of the cavity will not reach the base of the unconsolidated Tertiary. This way, formation of significant subsidence and sinkholes is prevented.

In the past ten years, new caverns were developed with the above mentioned 5 m safety roof and the concept of 'inherently safe' caverns using a single well (modern SCCs). The main advantage of developing a cavern with only one well is that the level of the blanket oil that is necessary to control cavern development is easier to monitor. This implies that cavern development of these SCCs is controlled more effectively compared to the MCCs of category 2 and 3.

In Figure 21 it can be seen that the oldest caverns of category 1 (red) are situated in the vicinity of the evaporation plant in Hengelo (black). New caverns are developed at an increasing distance from the plant. Since nowadays all new wells that are developed are SCCs, only the details of the solution mining process of this category (4, orange) will be discussed here.

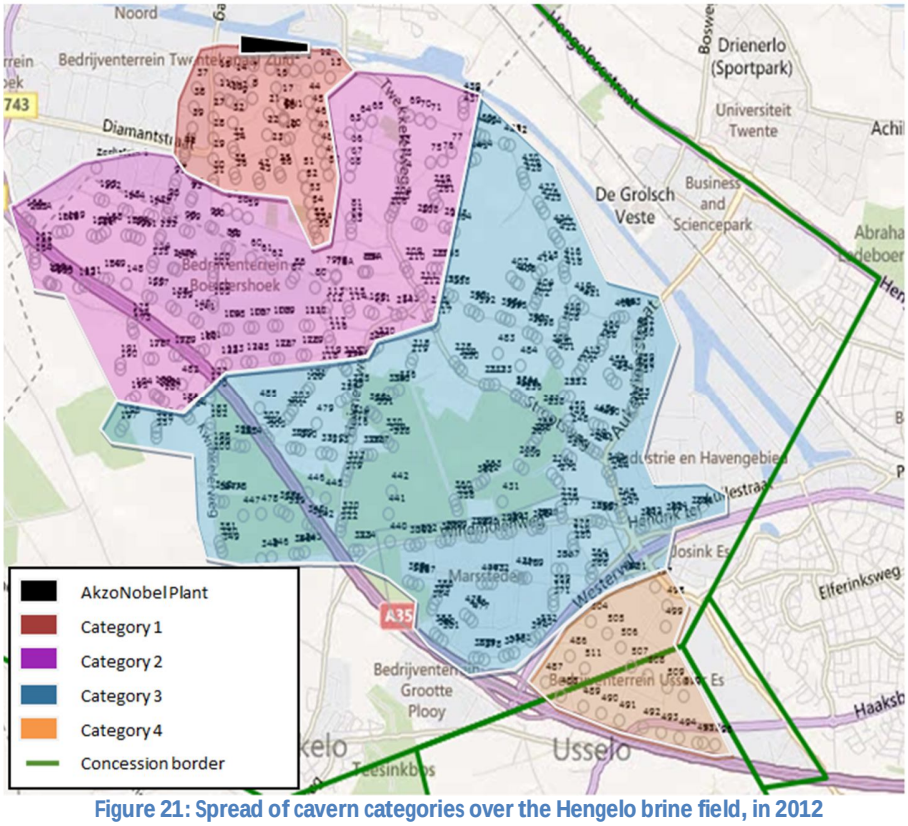

Figure 21: Spread of cavern categories over the Hengelo brine field, in 2012

SCCs are developed in three stages, starting with the sump phase. During the sump phase an undercut for the cavern is created so the development is mainly horizontal. At the end of the sump phase the cavern has a diameter of around 80 m and a height of 2.5 m in the centre. The level of the blanket oil that controls the vertical development of the cavern is monitored with a Blanket Control System (BCS). The sump phase takes about 14 months during which the cavern produces brine at a flow of 20 m^3/h. At the end of this phase a cavern has produced 11,000 tons of salt (AkzoNobel, 2012).

The following phase is the First Main Leaching Stage (1st MLS). During this stage the cavern height is allowed to increase 7 m. The flow is increased from 20 to 30 m^3/h and at the end of this phase the cavern has produced 150,000 tons of salt in total. During the Second Main Leaching Stage (2nd MLS) the cavern is allowed to expand to a diameter of 120 m and to a final height between 25 and 30 m, that varies with the thickness of the salt (AkzoNobel, 2012).

Between every phase a work-over is done. During a work-over the production strings are removed from the well. A sonar measurement is carried out to check the development of the cavern. To start the next phase, the production strings are placed back in the well and they are hung at the required depths.

4.3. Geomechanical model

In this section the geomechanical models of the SCCs in Hengelo brine field are discussed. The SCCs are arranged in parallel rows as much as possible. This can be seen in Figure 22, where the wells in the Usseleres area are marked. This field lay-out required two different geomechanical models, a first one for the row pillars (pillars between the rows) and a second one for the in-line pillars that separate the caverns in the row.

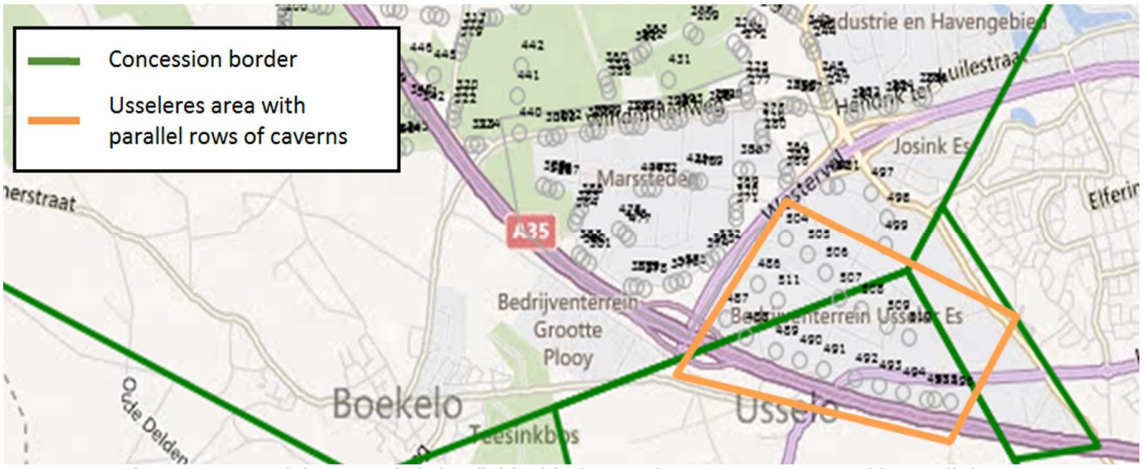

Figure 22: Part of the Hengelo brine field with the Usseleres caverns arranged in parallel rows

4.3.1. Row pillars

BGR conducted a study on the stability of the row pillars. The study is described in this subsection following the flow-diagram that was introduced in subsection 3.3.1. All information about this model is taken from BGR (2004b).

Scope and objectives

The objective of this study is to investigate the degree to which row pillars are loaded by means of finite element modelling. Row pillars are pillars between the rows in which caverns are aligned as indicated in Figure 23.

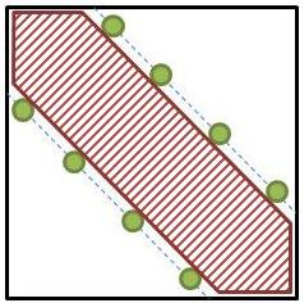

Figure 23: Plan view of caverns represented by wells (green dots) that are aligned in rows with row pillars in between (indicated in red)

Model type

The stability of row pillars is assessed with a 2D plane strain model. Half a cavern is modelled because a vertical axis of symmetry runs through the middle of the cavern. In Figure 24 the complete model can be seen as well as a magnification of the zone around the half-cavern in the model. A consequence of the choice for a 2D plane strain model, is that the model is infinite in the direction perpendicular to the modelled plane. For this model it means that the cavern is infinitely long in the direction of the row. This implies that there are no in-line pillars that separate the caverns in the rows from each other, and therefore the in-line pillars are assumed not to carry any load. BGR used their own finite element program named ANSALT to do the calculations.

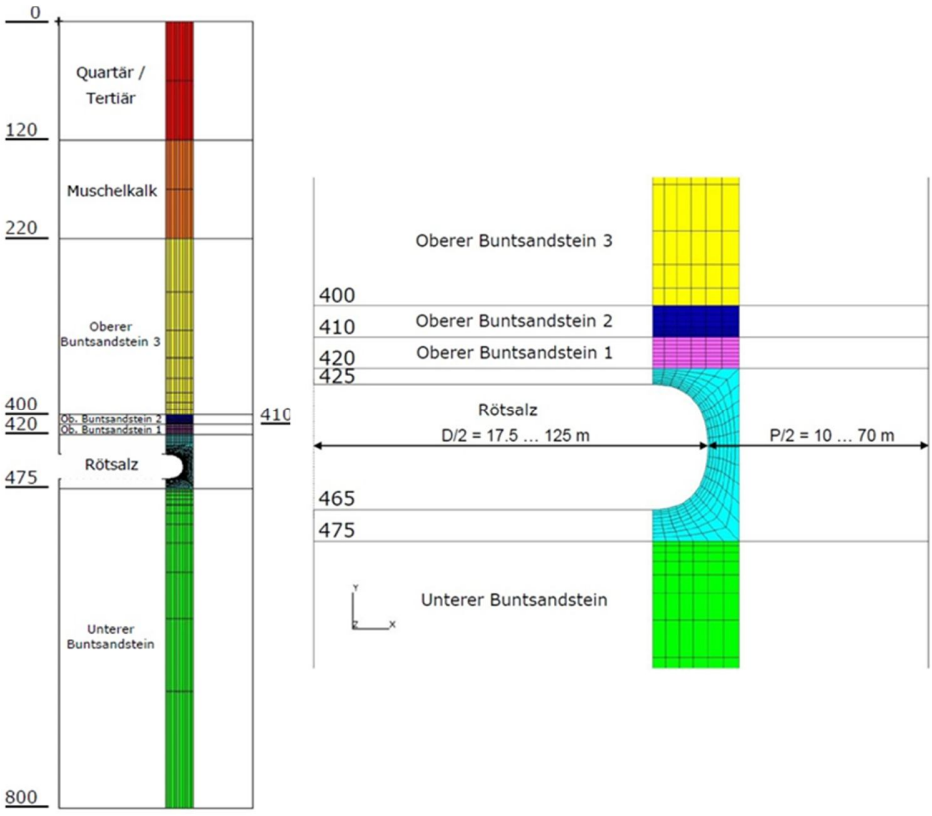

Figure 24: Complete geomechanical model (left), magnification of zone around cavern (right), (BGR, 2004b)

Calculation variants

In this study three calculation variants have been assessed, a base case and two alternatives.

Base case:	Cavern height of 40 m and intact anhydrite above the salt, indicated with Oberer Buntsandstein 1 in Figure 24.
Alternative 1:	Cavern height of 40 m and sliding planes in Oberer Buntsandstein 1
Alternative 2:	Cavern height of 20 m and intact Oberer Buntsandstein 1

From this brief description of the calculation variants it is clear that the effects of cavern height and fractured anhydrite above the salt on the load of the row pillars are investigated. Each variant is calculated a number of times with different combinations of cavern diameter and pillar width.

Simplifications and assumptions

The vertical dimensions of the model extend from 0 (surface level) to a depth of 800 m. Depending on the specific combination of pillar width and cavern diameter, the horizontal dimensions of the model are adjusted. In every calculation half the cavern diameter *D* and half the pillar width *P* are modelled. It can also be seen in Figure 24, that the division of the model into elements (or the mesh) is much finer near the cavern, than towards the upper and lower edges of the model.

Boundary constraints

The boundary constraints limit the degrees of freedom at the boundary. The nodes (corners of the elements) that lie on the vertical boundaries of the model are fixed horizontally, so they can only move vertically along the boundary. At the bottom of the model, the nodes are fixed vertically, so they can only move horizontally.

Geology

Figure 24 shows how the different geological layers are implemented into the model. All layers have different material properties and their own thickness. It is assumed here that all layers have a constant thickness throughout the extent of the model and that they are all perfectly horizontal. In practice this is not the case, because the thickness of all layers, as well as the height of the ground level varies. Moreover the salt layer is inclined slightly, as mentioned before this inclination is 6° SSW. This model also assumes that there is 10 m of salt between the bottom of the cavern and the underlying layer the Unterer Buntsandstein. When a well is drilled, it is always drilled until the Unterer Buntsandstein is reached. Also the bottom of the cavern is not developed 10 m above the base of the salt layer, because the inner production string is hung 0.5 m above the base of the salt layer during the sump phase (AkzoNobel, 2012). For these two reasons the modelled 10 m of salt below the bottom of the cavern, do not match with the situation in practice. Also an important simplification is that the entire Röt salt layer is considered homogeneous, where in practice it is built up of salt layers A to D that are separated by claystone layers.

Cavern development

In practice a SCC is developed in a period of 10 to 15 years (AkzoNobel, 2012). In this period the cavern develops from zero cubic meter volume to its final dimensions. In the geomechanical model this is highly simplified. Initially there is no cavern and the vertical stress is equal to the lithostatic stress that can be calculated at each depth with the density and thickness of each overlying layer. From the point in time when the model starts to run, the cavern is incorporated into the model at its full dimensions instantaneously. However, the pressure within this cavern is lowered gradually, from lithostatic to hydrostatic pressure in one year time. This is illustrated by Figure 25 in which the pressure at a depth of 425 m (roof of cavern), is displayed over time.

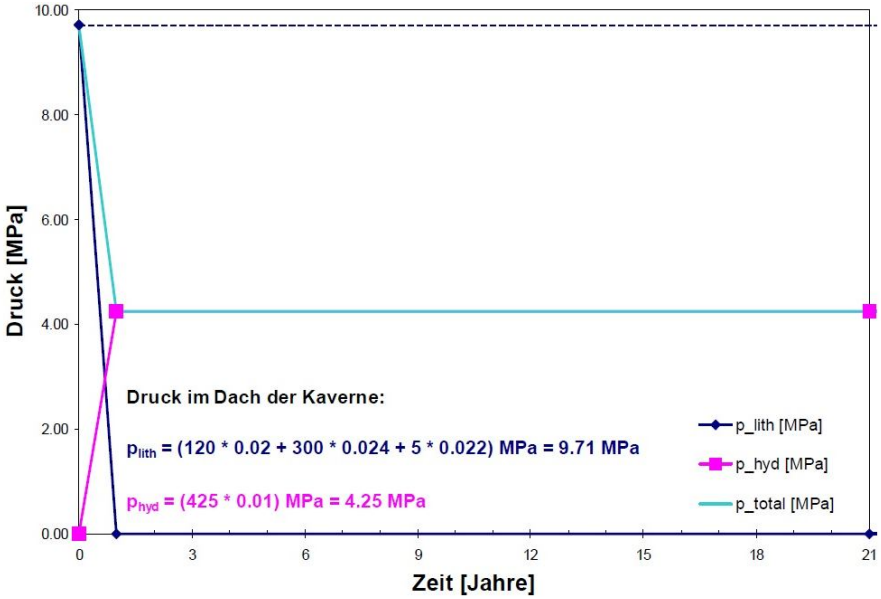

Figure 25: Pressure at 425 m depth where the roof of the cavern is situated, (BGR, 2004b)

The dark blue curve represents the lithostatic pressure that is decreased from 9.71 MPa to 0 in the first year of the cavern's life. The pink curve shows that the hydrostatic pressure is increased from 0 to 4.25 MPa, where the pressure gradient of water is used (0.01 MPa/m) instead of that of brine (0.012 MPa/m), which is a conservative approach. The light blue curve is the summation of the other two. It shows that in 1 year time the pressure drops from lithostatic to hydrostatic values and remains constant afterwards. This approach to implement the development of a cavern differs largely from the situation in practice. However this model is calculated over a period of 200 years to assess long term stability, in which the gradual development of a cavern over 10 to 15 years is not relevant over such a long time span. This way the model is kept simple.

Temperature

Temperature variations are not considered in this model. It is assumed that the temperature is 25 °C throughout the entire model and during the complete modelling period. So the effect of increasing temperature with depth is neglected, as well as the effect of the temperature of the injected water.

Material behaviour and parameters

Material models

In the report that was written about this study, it is not mentioned which material model is used to model the behaviour of the non-salt layers. Considering the parameters that are listed in Table 2, it is assumed here that their behaviour is modelled linear elastically. An exception is the material model that is used for Oberer Buntsandtein 1. The Drucker-Prager model was used for this formation that consists of anhydrite.

The constitutive law that is used to model the creep behaviour of salt is the BGRa creep law.

Material Parameters

The material parameters of all materials in the model are listed in Table 2. Table 3 lists the parameter values of the Drucker-Prager model and the BGRa creep law. For the Drucker-Prager model there are pre-failure and post-failure values of α and k. The pre-failure set is used for intact anhydrite and the other set is for fractured anhydrite.

Stratigraphy	Lithology	E [MPa]	ρ (kg/m³)	ν [-]	K_0 [-]
Quatär & Tertiär	Sand and clay	34	2000	0.33	0.493
Muschelkalk	Claystone, limestone, dolomite	5500	2400	0.45	0.818
Oberer Buntsandstein 3	Claystone	5500	2400	0.33	0.493
Oberer Buntsandstein 2	Claystone	5500	2400	0.33	0.493
Oberer Buntsandstein 1	Anhydrite	15500	2400	0.33	0.493
Rötsalz	Röt salt	25000	2200	0.25	1.0
Unterer Buntsandstein	Claystone	5500	2400	0.33	0.493

Table 2: Material parameters of different geological layers of the row pillar model, (BGR, 2004b)

Drucker-Prager parameters		
	Pre-failure	**Post-failure**
α [-]	0.4448	0.3338
k [MPa]	4.888	3.666
BGRa parameters		
A [day^{-1}]	0.5	
Q [kJ mol^{-1}]	54	
R [KJ mol^{-1} K^{-1}]	8.31441	
T [K]	298	
σ* [MPa]	1	
n [-]	5	

Table 3: Drucker-Prager parameters for Oberer Buntsandstein 1 and BGRa parameters for Röt salt, (BGR, 2004b)

Evaluation criteria and subsidence prediction

Evaluation criteria

To evaluate the long-term stability of the modelled row pillars, the stress states are plotted in the invariant diagram. The points need to be in the compressibility domain, i.e. below the dilatancy boundary. The short term strength is also plotted in the invariant diagram. A utilization degree of η = 25%, 30% and 35% are applied because this is the range of η that is used for storage caverns. Since this cavern will only be used for brine production this is a conservative evaluation criterion.

Subsidence Assessment

This model does not include a subsidence analysis. The subsidence assessment of the Usseleres area of the Hengelo brine field is discussed in section 4.4.

Results

The results of this study are presented in the form of cavern diameter *D* versus pillar width *P* diagrams. From each *P-D* combination, the stress states of the elements after 200 years were plotted in the invariant diagram. Depending on the position of the points in the diagram with respect to the η-curves for 25, 30 and 35%, the overall utilization degree for each *P-D* combination was determined. For the base case this lead to the diagram in Figure 26 at *t* = 200 years. *D* is on the horizontal axis, *P* on the vertical. From this diagram it can be derived that if a utilization degree of η = 30% would be allowed and a cavern of 120 m diameter would be desired, the pillar width would have to be nearly 70 m (indicated by arrows).

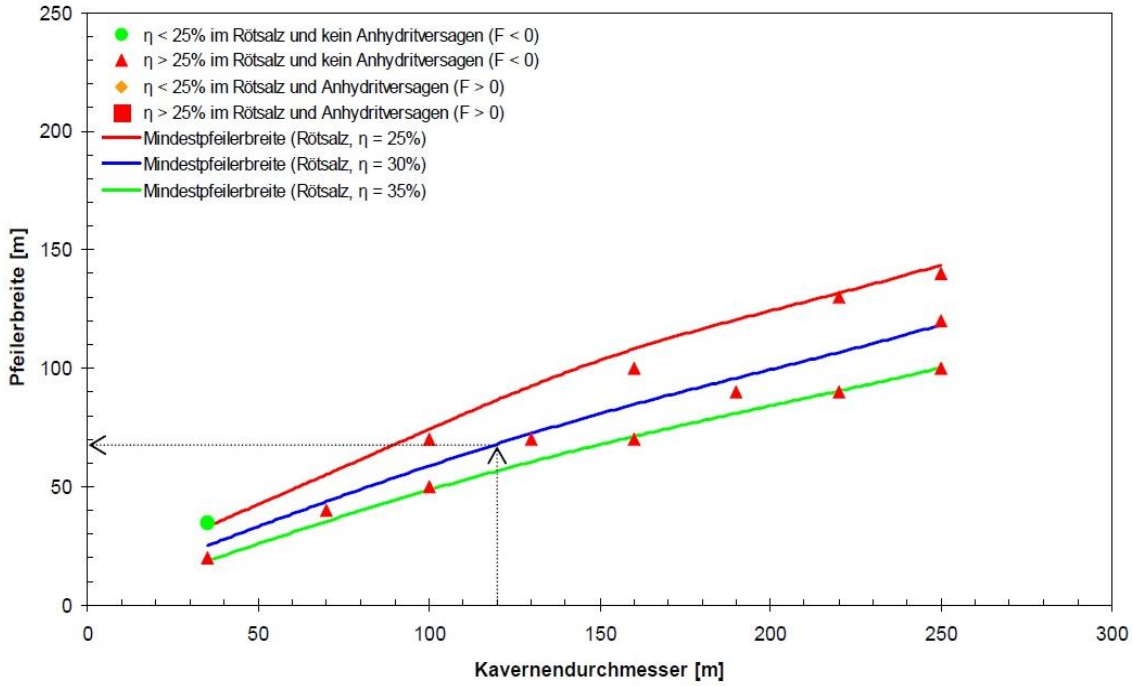

Figure 26: Result of P-D combinations for base case after 200 years, (BGR, 2004b)

Conclusion and recommendations

Diagrams like Figure 26 are produced for alternative 1 and 2. It is concluded from the results of alternative 1, that the failure of anhydrite hardly influences the behaviour of salt. However, if it is required to prevent anhydrite failure in case of fractured Oberer Buntsandstein 1, the required pillar width roughly doubles. The results of alternative 2 indicate that in case the cavern height is limited to 20 m, the required pillar width decreases with 10 to 20 m.

4.3.2. In-line pillars

BGR also conducted the study on the in-line pillars that will be discussed in this subsection. Again all information is taken from the report that was written about this study by BGR (2004c). In-line pillars are the pillars between the caverns in a row, indicated in red in Figure 27. The details of this study show many similarities with the row pillar study that was described in the previous subsection. Therefore only the differences between both models will be discussed in this section.

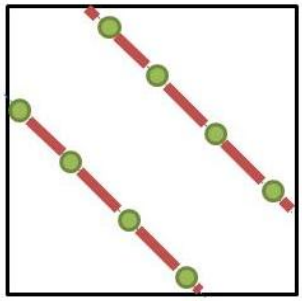

Figure 27: Plan view of row configuration of cavern wells (green dots) with in-line pillars (red)

Scope and objectives

The objective of this study was to determine the minimum pillar width of the in-line pillars to guarantee stability.

Model type

Unlike the model for the row pillars, this in-line pillar model is 3-dimensional. Two quarter caverns are incorporated into this model, as is shown in Figure 28. Again BGR used their own ANSALT software to do the calculations.

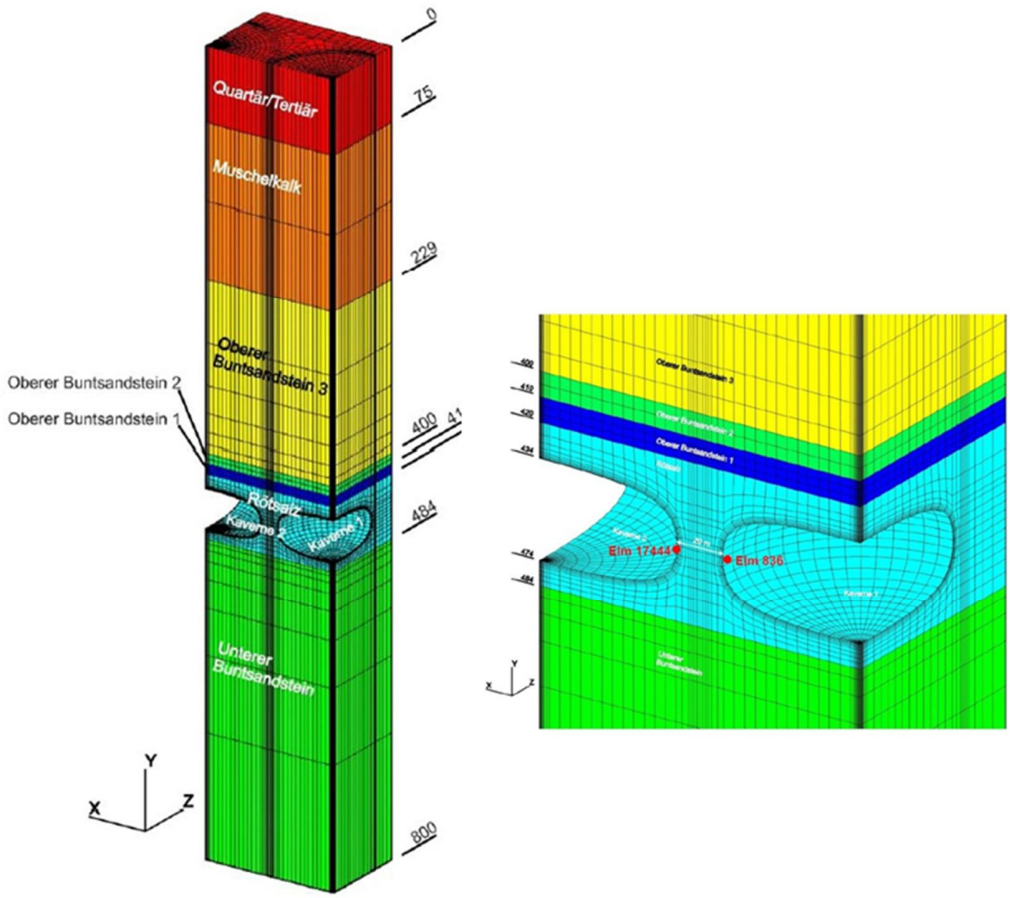

Figure 28: The entire 3D in-line pillar model (left) and a magnification of the zone around the caverns (right), (BGR, 2004c)

Calculation variants

There are 4 calculation variants, namely one base case and 3 alternatives. The difference between the calculation variants lies in the pillar widths and cavern diameters. The specific dimensions of each variant are listed in Table 4. The base case has a thin row pillar, alternative 1 has a wider row pillar, alternative 2 has a wider in-line pillar and the last alternative has a smaller cavern diameter. In all variants the caverns have a height of 40 m.

Calculation Variant	Row pillar width (m)	Cavern Diameter (m)	In-line pillar width (m)
Base Case	68	120	20
Alternative 1	272	120	20
Alternative 2	272	120	40
Alternative 3	272	80	20

Table 4: Calculation variants in in-line pillar study, (BGR, 2004c)

The purpose of having two caverns in the model is mainly to investigate the effects of pressure variations in one cavern on the stress state around both caverns. Initially, in both caverns the pressure is lowered in one year from lithostatic to hydrostatic pressure plus the production pressure in the network to which the caverns are connected, which is 2 MPa.

In Figure 29 below it can be seen that in cavern 1, which is the right hand cavern in Figure 28 (right), the 2 MPa production pressure is released for 1 year in every cycle of 5 years. This is done to simulate the effect of a work-over. Before and during a work-over the cavern is taken out of production. It is disconnected from the network and therefore the 2 MPa production pressure is released. In cavern 2, the left-hand cavern in Figure 28 (right), the pressure is constantly the hydrostatic pressure plus the production pressure after the first year has passed. Note that the hydrostatic pressure is calculated with the pressure gradient of water (0.01 MPa/m) for cavern 1 and with the pressure gradient of brine (0.012 MPa/m) for cavern 2.

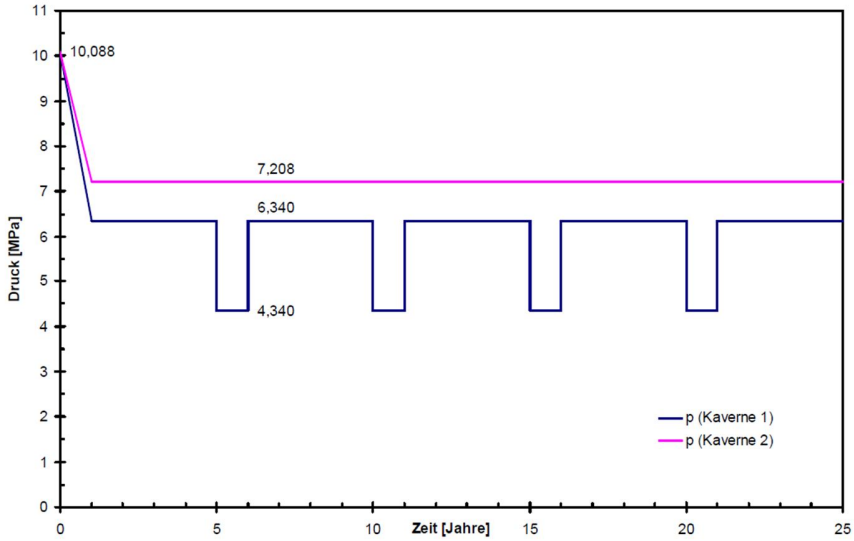

Figure 29: Pressure variations in time in cavern 1 with work-overs (blue) and cavern 2 without work-overs (purple), (BGR, 2004c)

Simplifications and assumptions

Dimensions and mesh

The horizontal dimensions (*x* and *z* in Figure 28) depend on the specifications of the calculation variants. The row pillar width determines the *z* dimension, the in-line pillar width determines the *x* dimension and the cavern diameter influences both the *x* and *z* dimension. In the vertical direction (*y*) the model extends from ground level at 0 m to 800 m depth. Again, the mesh is finer near the caverns and coarser towards the edges of the model.

Boundary constraints

In a 3D model the boundary constraints are similar to a 2D model. The only difference is that the side boundaries are not completely fixed horizontally. They are only fixed in the direction perpendicular to the boundary surface.

Geology

The geological layers that are present in the model are the same as in the row pillar study, however thicknesses and depth intervals have changed. Table 5 lists the depth intervals and thickness of all layers in both models, the values that do not correspond are shaded in blue. There is no reason mentioned in the report for the differences. Despite the changes the salt layer still has its top at 420 m depth, but its

thickness changes from 55 to 64 m. Since the stress state of the pillar is the object of study, this is a change that can have a serious influence on the results. The salt roof is now significantly thicker, namely 14 m instead of 5 m. Again the 10 m of salt below the bottom of the cavern that are modelled, are not present in reality.

Row pillar model (BGR, 2004b)		Stratigraphy	In-line pillar model (BGR, 2004c)	
Depth interval (m)	Thickness (m)		Thickness (m)	Depth interval (m)
0	120	Quartär & Tertiär	75	0
120				75
120	100	Muschelkalk	154	75
220				229
220	180	Oberer Buntsandstein 3	171	229
400				400
400	10	Oberer Buntsandstein 2	10	400
410				410
410	10	Oberer Buntsandstein 1	10	410
420				420
420	55	Rötsalz	64	420
475				484
475	325	Unterer Buntsandstein	316	484
800				800

Table 5: Thickness and depth intervals in row and in-line pillar models, differences in blue shading

Cavern development

The volumetric development of the caverns is similar to that of the row pillar method by lowering the pressure. Differences were already discussed under the heading 'calculation variants' where the pressure graphs are shown, see Figure 29.

Temperature

Temperature effects are also not taken into account in this model. The temperature remains constant at 25 °C.

Material behaviour and parameters

This aspect of the model shows many similarities with the row pillar model. All material parameters are the same and can be found in Table 2. The creep law that is implemented is again BGRa and the same values for input parameters are used.

Since the previous study showed that the behaviour of salt is not influenced significantly by the failure of the Oberer Buntsandstein 1 Formation, this is not considered in this study.

Evaluation criteria and subsidence prediction

Apart from the utilization degree criterion and the dilatancy boundary and short term strength, a criterion is used of the same character as the fracturing criterion that is discussed in 3.2.3. It is however formulated slighty different. It states that the maximum principal stress that acts tangential to the cavern contour ($\sigma_{t,max}$) must always be larger than the sum of the brine pressure ($p_{hydrostatic}$) and the production pressure ($p_{production}$), see (Eq. 4.1).

$$\sigma_{t,max} > p_{hydrostatic} + p_{production} \qquad \text{(Eq. 4.1)}$$

Here $p_{hydrostatic} + p_{production}$ is equivalent to p_i in (Eq. 3.17) and $\sigma_{t,max}$ is equivalent to σ_3. Where the fracturing criterion in 3.2.3 only specifies that the internal pressure must be compared to the minor principal stress, here it must be the largest principal stress that is acting tangential to the cavern contour.

Just like in the row pillar study, subsidence is not taken into account.

Results

The utilization degree and fracturing criterion are the criteria to evaluate the results with the varying pressure in time. In Figure 30 the utilization degree is plotted for four moments in time for the base case. Just before the first time that the 2 MPa production pressure is released (a), the utilization degree is maximum 14%. In cavern 1 (right), where the hydrostatic pressure is lower because it is calculated with the pressure gradient of water, the utilization degree is higher than in cavern 2 (left) where the pressure gradient of brine is used. Because of the higher pressure gradient of brine, the fluid in cavern 2 is more capable of 'supporting' the cavern contour.

Just after release of production pressure (b), the utilization degree at the contour of cavern 1, exceeds 30%, which is the maximum allowed value. However, directly beyond the cavern contour, it decreases quite rapidly. In the in-line pillar the maximum value of η is 18%, which is allowed.

Due to stress redistributions the situation at the cavern contour becomes more balanced towards the end of the year of pressure release. In (c) it can be seen that the maximum value of η at the contour has reduced to 22%. Also beyond the cavern contour the utilization degree decreases. However in the in-line pillar the maximum value of η remains 18%.

Just after the production pressure is applied again, the utilization degree at the contour of cavern 2 is higher than in cavern 1. Apparently the fact that the pressure is increased in the neighbouring cavern, results in a higher loading of the contour of cavern 2. The maximum value remains 14%, which is equal to the situation before the production pressure was released.

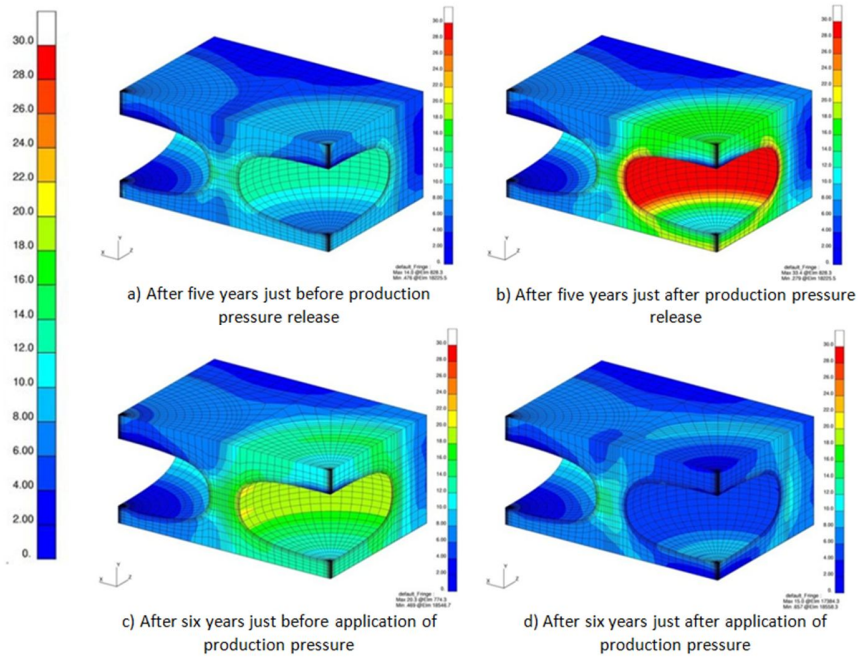

Figure 30: Utilization degree at different points in time, (BGR, 2004c)

Figure 31 shows a similar graph for the development of the fracturing criterion through time at the same elements in the base case. It shows that the criterion is never violated in cavern 2, but it is violated already after the second re-application of production pressure in cavern 1. Therefore it can not be guaranteed that no fractures will form.

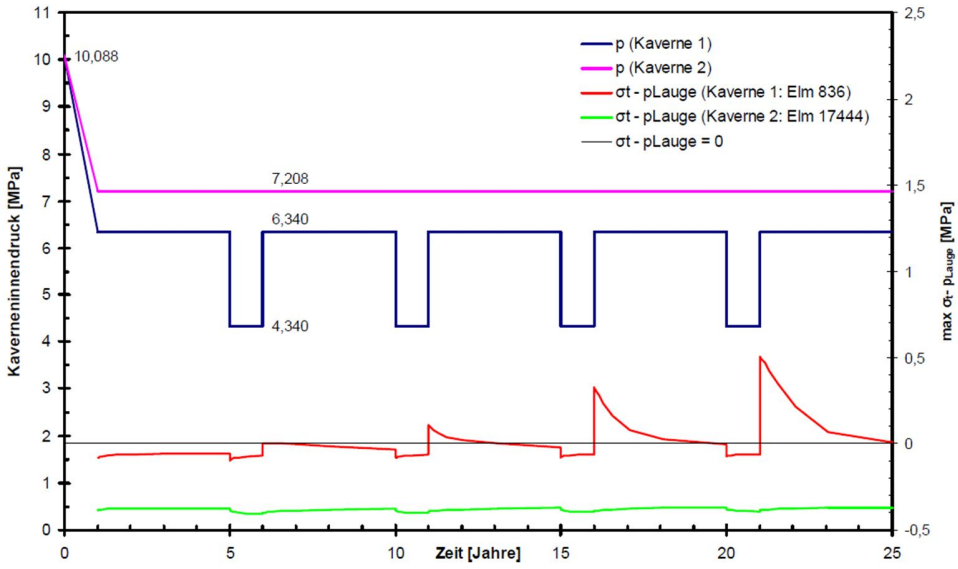

Figure 31: Development of the fracturing criterion in time with the pressure cycles in red for cavern 1 and green for cavern 2, (BGR, 2004c)

Conclusion and recommendations

When the results for the base case are compared to the other variants, it is concluded that taking a wider in-line or row pillar, does not influence the situation at the cavern contours that are in some cases violating the utilization degree and/or fracturing criterion. However, it does have a positive effect on the situation in the centre of especially the in-line pillars. A smaller cavern diameter does have a positive effect on the utilization degree at the cavern contour.

4.4. Subsidence prediction

The subsidence prediction for the Usseleres area was carried out by RESPEC. RESPEC used the Salt-subsid method to make an analytical subsidence prediction. In this analysis only the y_{ss} convergence parameter was determined specifically for the Hengelo brine field. The other parameters were assigned standard values. Like the angle of the subsidence cone (always 45°) and the translation factor *a* that gives the portion of subsurface volume reduction that is translated to surface (in this analysis it is always 1). Apart from the y_{ss} parameter, a table of details per cavern is used as input into the model. The required details are volume, depth and well coordinates (RESPEC, 2010b).

The determination of y_{ss} was based on earlier subsidence measurements in the Hengelo brine field. The calculated subsidence rate is 0.4 mm/year (RESPEC, 2008). To relate this to the geomechanical model, a BGR study on the relation between extraction grade and subsidence rate was referred to. This study resulted in the relation that is presented in Figure 32 that shows that the subsidence rate starts to increase severely at extraction grades higher than 30%. Although the extraction grade of the Hengelo brine field varies with the different phases of field development throughout the years, it is certain that it is smaller than 30%. This is the extraction grade that matches a subsidence rate of 0.4 mm/year (RESPEC, 2008).

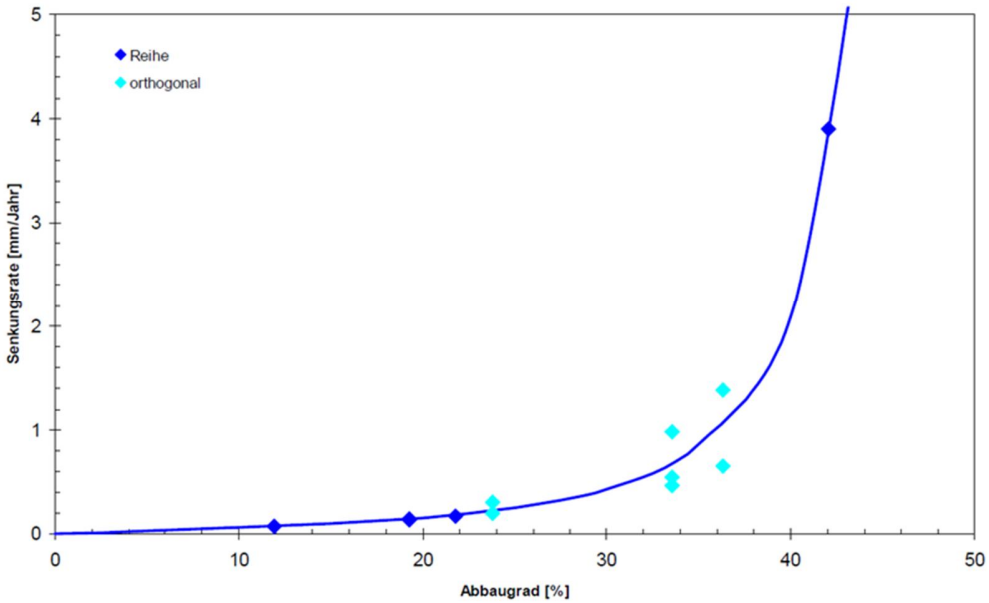

Figure 32: Relation between extraction grade and subsidence rate after 100 years, for row configurations in dark blue, (BGR, 2003b)

By variation of the input parameter y_{ss} a subsidence prediction of the existing field was carried out using Salt-subsid. The parameter was varied until a satisfying match with the measured subsidence in the existing field was reached with a value of y_{ss} = 0.00008 m^3 of yearly volume loss per cubic meter of cavern volume. Using y_{ss} = 0.00008 y^{-1} as input value, a subsidence prediction was done for the Usseleres area.

Among the outputs were a map with the contour lines of the subsidence bowl that shows that the biggest subsidence will be 49 mm after 100 years. The modelled strain maxima were 24 microstrain in extension and 38 microstrain in compression where strains higher than 1000 microstrain generally start to cause damage (RESPEC, 2010b).

5. Delfzijl brine fields

AkzoNobel's salt plant in Delfzijl is supplied with brine from the Heiligerlee and Zuidwending brine fields. The Heiligerlee brine field is close to the town of Winschoten and lies in the mining permit Adolf van Nassau III. East from the town of Veendam lies the Zuidwending brine field in the extension of the Adolf van Nassau III mining permit. Figure 33 provides an overview of the locations.

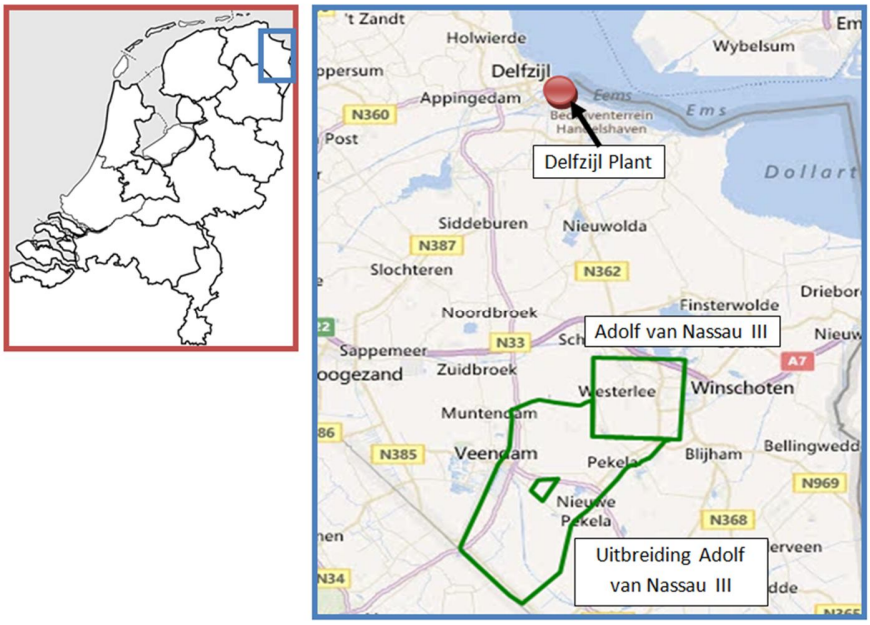

Figure 33: Location of the Adolf van Nassau III mining permits and the Delfzijl plant

In the early nineteen fifties the presence of a salt dome, that had already been indicated by gravimetric and seismic exploration, was proven by exploration wells that were drilled near Winschoten. In 1959 the Delfzijl plant started processing brine from the first wells that were drilled in the Heiligerlee brine field. In 1967 the mining permit was extended to develop a new brine field when another salt dome was found near Zuidwending (Wassmann & Brouwer, 1987).

5.1. Geology

The caverns of both the Heiligerlee and Zuidwending brine field are situated in Zechstein salt domes. In the central parts of both domes, which is where the caverns are situated, there is mainly salt of the Stassfurt series that is also known as Z2 series. The younger Zechstein formations occur at the flanks of the domes (AkzoNobel, 2008a, AkzoNobel, 2008b). Cross sections through the Heiligerlee (a) and Zuidwending (b) brine fields are presented in Figure 34.

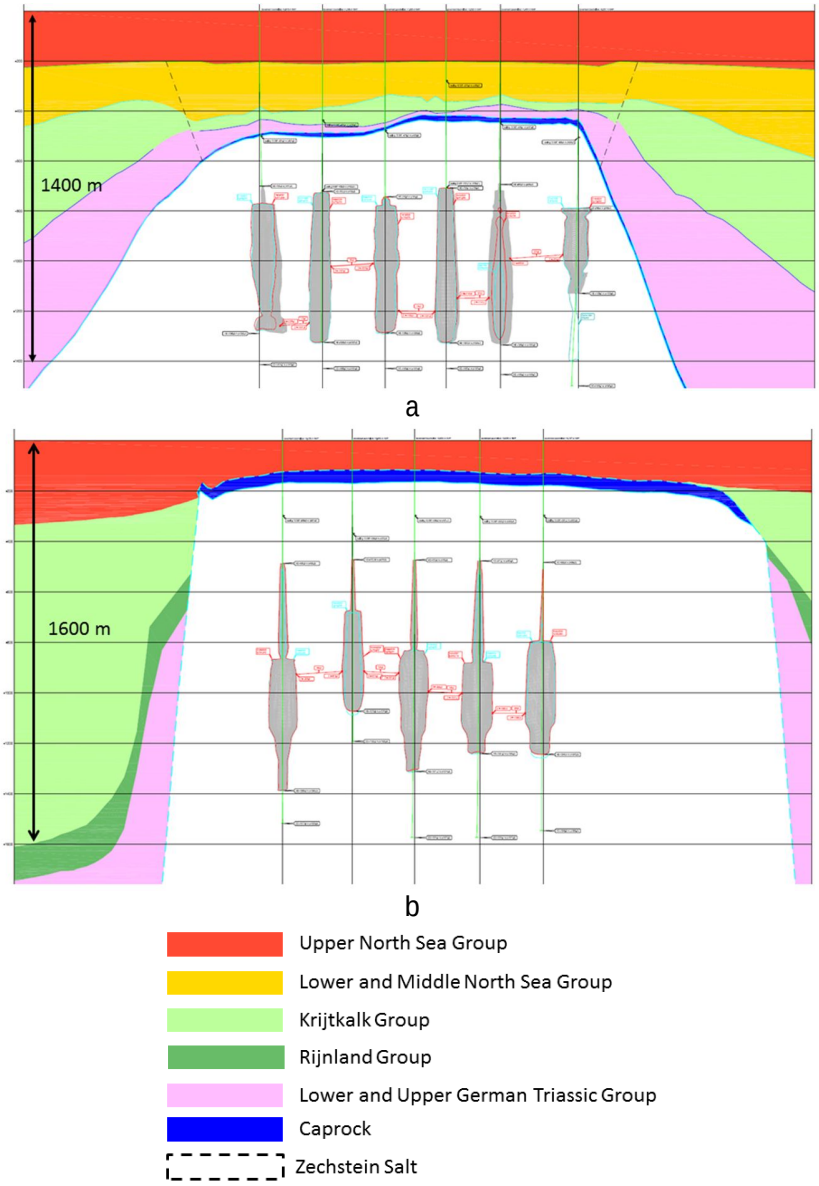

Figure 34: Cross sections through the Heiligerlee (a) (Oranjewoud, 2007) and Zuidwending (b) (Oranjewoud, 2008) brine fields

The Heiligerlee salt dome is developed in NNW-SSE direction. The top of the dome is found at a depth of 410 to 510 m. The top of the caprock lies at a depth between 380 and 490 m, so this caprock has an average thickness of 25 m. The top of the Zechstein formations are found much deeper around the salt dome, namely at 2500 m depth. The depth of the base is around 2800 m. The salt dome is overlain by the Lower and Upper German Triassic Group (10 to 30 m thick) and the 30 to 100 m thick "Krijtkalk" Group that contains deposits of Cretaceous and Tertiary age. This is overlain by the deposits of the 150 m thick Lower and Middle North Sea Group and a 200 m thick layer of Upper North Sea Group deposits (AkzoNobel, 2008a).

The Zuidwending dome is 'boomerang-shaped' and the caverns are situated in the northern part. The top of the salt dome is found at a depth of around 200 m. The top of the caprock is found at depths between 110 and 140 m and the caprock is 60 to 70 m thick. Around the salt dome, the top of the Zechstein formations lies at a depth of roughly 2700 m and the base at 2900 m. Apart from the caprock, the salt dome is only overlain by the deposits of the Upper North Sea Group up to the surface (AkzoNobel, 2008b).

5.2. Mining

Due to their shape, salt domes are very suitable for the development of long vertical cylindrical caverns. These caverns are 125 m in diameter and their development starts with a sump phase during which bottom injection is applied. The caverns can be developed up to a height of hundreds of meters and therefore they obtain a much larger volume per cavern than in the Hengelo brine field. There is not a big difference between the combined annual brine production of the Heiligerlee and Zuidwending brine field compared to the Hengelo brine field. Because the amount of brine that can be produced per cavern is much bigger in Heiligerlee and Zuidwending,the number of caverns is much smaller. In Heiligerlee there are 12 caverns and there are 8 caverns in the Zuidwending brine field. Not all caverns are active, some are not producing due to operational restrictions and there is also a cavern that is used for nitrogen storage.

Since the amount of caverns is much smaller than in the Hengelo brine field, the flow per cavern is significantly higher. This requires production strings with a bigger diameter. For example combinations of 7 and 10¾ inch or 6 $^{5}/_{8}$ inch and 9 $^{5}/_{8}$ inch productions strings are used. Where in Hengelo, a typical combination is 4.5 inch inner and 7 inch outer production strings.

As well as in the Hengelo brine field the development of caverns is monitored with regular sonar measurements. At the end of work-overs production strings are hung at new depths to allow the cavern to develop to new dimensions. Production is also monitored by online flow and pressure meters and saturation measurements.

East of the Zuidwending brine field, caverns have been leached for gas storage in the 'Aardgasbuffer Zuidwending' project. AkzoNobel has supervised the drilling and leaching process. The gas-filled caverns are now operated by Gasunie and Nuon. The weak (undersaturated) brine that was produced by these caverns during the leaching process was pumped into caverns of the 'regular' Zuidwending brine field to become saturated. The natural gas buffer project is mentioned here, because the geomechanical model of the storage caverns differs from the ones that were developed for the brine fields of Heiligerlee and Zuidwending. These models will be discussed in the next section.

5.3. Geomechanical model

The geomechanical models of the Heiligerlee and Zuidwending brine fields are discussed here, as well as the geomechanical model of the natural gas storage caverns.

5.3.1. Heiligerlee and Zuidwending brine fields

The caverns in the salt domes of Heiligerlee and Zuidwending were originally planned and developed with the following guidelines that were established by Mr. Politiek and that were approved by the State Supervision of Mines (SSM) (BGR, 2002).

1. Maximum cavern diameter is 100 m.
2. Minimum pillar width between two adjacent caverns is 150 m.
3. Minimum thickness of salt in the roof of the cavern is 200 m.
4. Minimum pillar width between cavern and flank of dome is 200 m.

The topics of the geomechanical studies that were carried out for these brine fields were driven by the questions that were raised at different periods in time for specific reasons.

1. Before the nineteen nineties some studies were carried out to answer incidental questions, for example about underground storage possibilities.
2. In the nineteen nineties the possibility to enlarge cavern diameters from 100 to 125 m, to be able to mine more salt from existing caverns, was investigated.
3. In 2002 a study was carried out to decide whether the roof of the cavern should be raised from the 700 to 800 m depth range where the roofs were at that time to 400 m depth, that was already allowed by SSM.
4. Another study in 2002 was done to support further spatial planning of the brine fields, to create a favourable situation for limitation of cavern convergence from a surface subsidence point of view.
5. When borehole deviation measurements indicated that the boreholes were not perfectly vertical, there were concerns about the actual width of pillars between caverns. This led to investigations of pillar loading in 2003.
6. A methodology was developed to measure and monitor subsidence and to update subsidence predictions with the latest measurements. There is an update every 5 years.

From the nineteen nineties on, studies were carried out by BGR. Although there is quite an amount of studies that were carried out and the nature of the questions that gave rise to the studies differs in all cases, the approach that was used to do the geomechanical modelling is quite similar in most of the cases. Because of these similarities, a more general description of the models is given here, instead of describing all studies and all calculation variants separately. Moreover, there are some similarities with the modelling approach of the SCCs in the Hengelo brine field that is described in chapter 4.3.

Scope and objectives

As explained in the introduction to this section the objectives of the studies were based on questions that were of special relevance at that time. On one hand it concerned the stability of caverns depending

on the (enlarged) dimensions of the caverns and the bearing elements (pillars and roof). On the other hand the convergence (rate) of caverns was studied because this is the cause of surface subsidence.

Model type and calculation variants

All studies, whether cavern diameter, pillar width or field lay-out are considered, contain different calculation variants that are modelled with the most suitable type of model. For example a single cavern is modelled in an axisymmetric model and a hexagonal cavern field, or a row configuration of caverns is modelled with small 3D models that contain parts of a number of caverns. These models can be mirrored to create the complete field. This is illustrated in Figure 35, that shows a plan view of a cavern field with a triple row configuration. By 3D modelling of the yellow part that contains a half-cavern and a quarter - cavern and using the symmetric lay-out of the field, the entire field can be reconstructed by mirroring the yellow blocks.

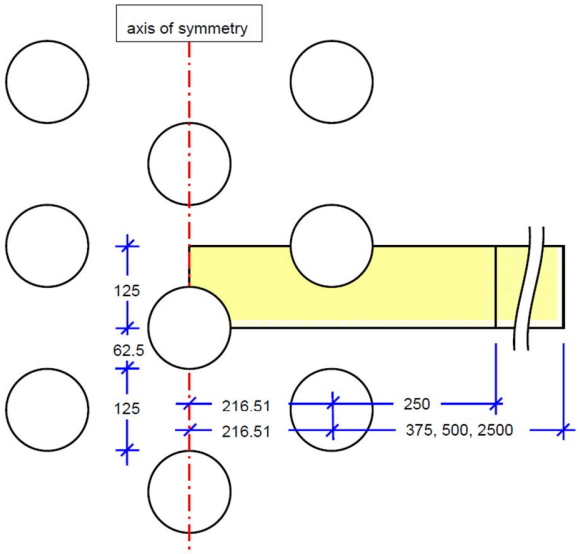

Figure 35: Portion of a triple row cavern field that is 3D modelled, with help of symmetry the entire field is built up by mirroring the yellow block, (BGR, 2002)

Depending on the objective of the study, relevant parameters are varied. Examples are cavern diameter, pillar width, creep parameters et cetera. In some cases sealing of a cavern is also modelled. All calculations are carried out with BGR's ANSALT finite element code.

Simplifications and Assumptions

Dimensions and mesh

Generally the vertical dimensions of the models extend from surface level down to 3 km depth, like in the study by BGR (2000). The horizontal dimensions depend on the desired cavern lay-out to be modelled. It can extend for example 3 km from the outermost row of caverns to the edge of the model. Since in both the Heiligerlee and Zuidwending brine fields the existing caverns are in different stages of development, it is considered in each study how to choose the dimensions of one cavern that represents all caverns in the field. In some studies the maximum allowed dimensions are chosen. This modelled cavern volume is then much higher than the real cavern volume at that time. In another study the average dimensions and depth interval of the caverns at that time were used, like in some calculation

variants in the study by BGR (2003a). In all cases the modelled caverns are perfectly cylindrical. Since the reports about the modelling studies say nothing about meshing and because they lack images of the models such as Figure 24, nothing can be said about the mesh that is applied to these models.

Geology

The geology that is represented in the models is usually very simple. For example the Heiligerlee diameter enlargement study considers a 500 m thick layer of Quarternary deposits and caprock that are represented by one set of parameters. From 500 to 3000 m depth a body of rock salt is modelled. The flanks of the dome are only incorporated into the models in a few cases, for example when pillar widths are very large in one calculation variant in the study by BGR (2002). In all models the rock salt is considered homogeneous.

Cavern development

The method of implementation of cavern development into the models is very similar to the way it is done in the models that are described in 4.3.1 and 4.3.2. Instead of taking 1 year time to let the pressure decrease from lithostatic to hydrostatic values, 3 years are taken, as shown in Figure 36. In some calculation variants, caverns are sealed after 30 years of production. The pressure in the cavern builds up, first with increasing pressure gradient, later with a constant pressure gradient, as determined from pressure build-up tests in the Heiligerlee I cavern, (BGR, 2000).

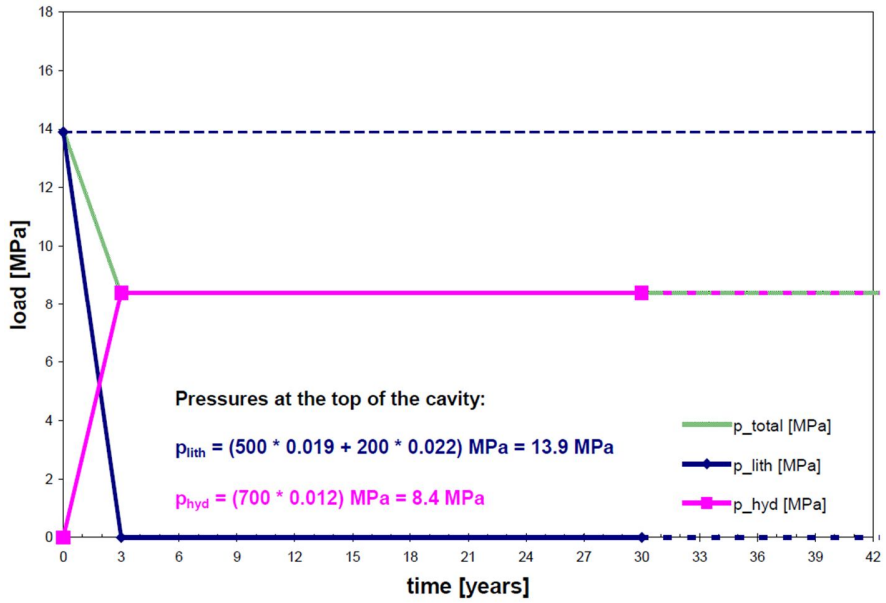

Figure 36: Pressure variation in time to simulate cavern development in the Heiligerlee brine field, (BGR, 2000)

Temperature

Temperature effects are also considered in the Heiligerlee and Zuidwending models. During production, relatively cold water is injected. As a reaction to this rock salt contracts, limiting cavern convergence. When a cavern is sealed the temperature increases again to geothermal values. This makes the rock salt and brine expand and this leads to a pressure build-up in the cavern. Just like pressure, temperature is a function of time and depth. The temperature curve that was used for the Heiligerlee diameter

enlargement study is presented in Figure 37. In the first 3 years the temperature decreases linearly to 35 °C. Afterwards it approaches 31 °C asymptotically.

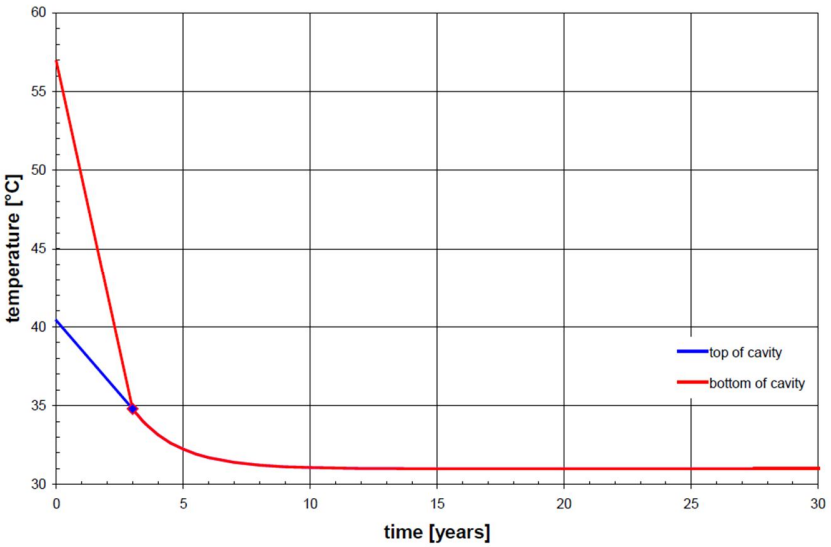

Figure 37: Temperature functions in time for bottom (-1450 m) and top (-700 m) of modelled Heiligerlee caverns (BGR, 2000)

Material behaviour

Material models and parameters

A good example of a table of material parameters is taken from the Zuidwending field optimization study by BGR (2002), see Table 6. The material behaviour of all non-salt layers is considered linear elastic. The creep behaviour of salt is modelled using the BGRa creep law, which is the same as for the Hengelo brine field. However it can be seen that for the *A* parameter, there are other values based on lab tests on the rock salt of the Zuidwending salt dome. The effect of variation of this parameters is investigated because two different values were used. Furthermore it can be seen in Table 6 that the effect of the rock adjacent to the dome is taken into account in at least one of the calculation variants.

	Quarternary	Adjacent rock	Rock salt	Brine
	Elastic parameters			
E [MPa]	100	12000	25000	-
K [MPa]	-	-	-	2000 (4000)
ν [-]	0.33	0.25	0.27	-
α_T [1/K]	1E-05	1E-05	4E-05	1.4E-04
ρ [kg/m³]	1900	2200	2200	1200
	Steady state creep parameters			
A [1/d] (normal/high)	-	-	0.18/0.72	-
Q [kJ/mol]	-	-	54	-
R [kJ/mol/K]	-	-	8.3143E-03	-
σ* [-]	-	-	1	-
n [-]	-	-	5	-

Table 6: Material parameters for Zuidwending field optimization study, (BGR, 2002)

Evaluation criteria and subsidence prediction

Evaluation criteria

For rock salt the stress states are evaluated with the dilatancy boundary and the long term strength. In pillars the rock salt is also evaluated with the utilization degree. Stability of non-salt materials is not considered in these studies.

Subsidence prediction

Apart from cavern and pillar stability all studies say something about subsidence. In some cases the effect of pillar widths on convergence rates and surface subsidence (vertical displacement at the top of the model) are taken into account. In other models the effect of the lay-out of a cavern field is considered (hexagonal grid or multiple rows).

Results, conclusions and recommendations

All studies contain a number of different calculation variants that are compared in the concluding chapters of the reports. In some cases they are compared on the basis of the stress states around the caverns. In most cases the convergence rates and surface subsidence are considered to compare the results of different calculation variants.

An example is shown in Figure 38 where the thicker lines represent the relation between subsidence rate and pillar widths for a triple row configuration. The green one is for low, the red one for higher values of creep parameters. To put the results in perspective, the outcome of the single cavity and infinite field variants are plotted as well. The lower red and green line are for single cavities, the upper for infinite fields. A conclusion that can be drawn from this figure is that at lower pillar widths (500, 750 and 1000 m, which is already higher than realistic in the field) the subsidence rate of a triple row configuration is very close to that of an infinite field.

The violet triangle on the right-hand border of the graph represents the calculation variant with 5000 m wide pillars and adjacent non-salt rock at 500 m distance from the outer row, with low creep properties. It is clear that taking the adjacent rock into consideration does not have a significant effect on the subsidence rate. This is just one example of how the results of different calculation variants are compared to come to conclusions.

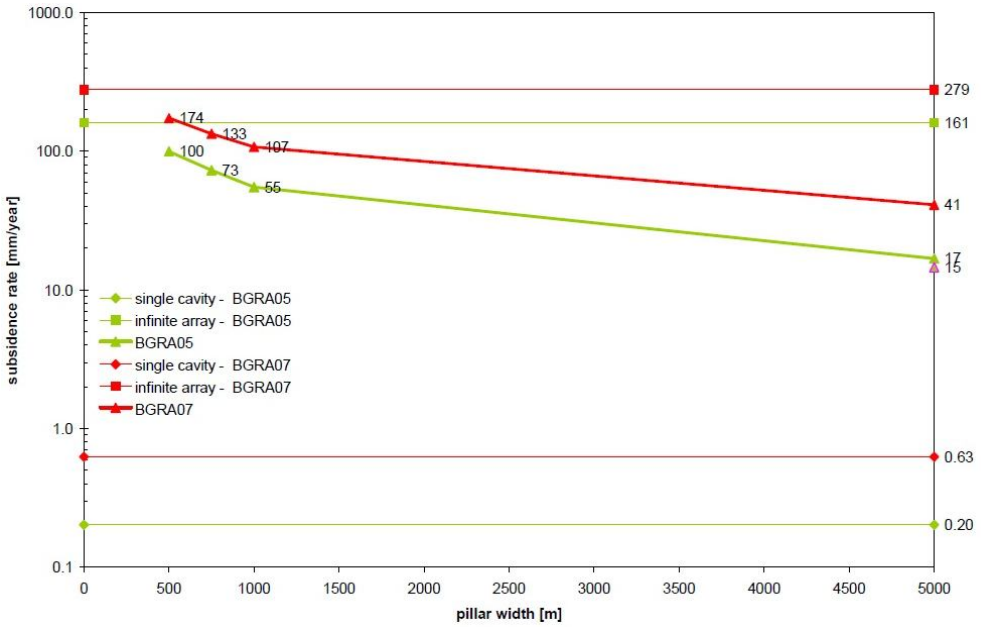

Figure 38: Subsidence rates resulting from varying the pillar width and creep properties in Zuidwending brine field (BGR, 2002)

5.3.2. Gas storage Zuidwending

So far the description of the modelling processes for both the Heiligerlee and Zuidwending brine fields, as well as for the SCCs in the Hengelo brine field have been quite similar. Although the salt deposits that the models were applied to differ largely (domal and bedded), the approach was generally the same. This is due to the fact that the same consultant (BGR) was hired to do the work. Based on their experience, BGR has developed a certain approach to go through the modelling process. Moreover they use their own software (ANSALT) and their own creep model (BGRa).

For the modelling process of the Aardgasbuffer Zuidwending (Natural gas buffer Zuidwending) that lies next to AkzoNobel's Zuidwending brine field, the German Institut für Gebirgsmechanik (IfG) was hired by AkzoNobel and the two other parties in the project: Nuon and Gasunie. Like BGR, IfG has developed their own approach to the modelling process on basis of their experiences. The following description of the geomechanical model of the Aardgasbuffer Zuidwending will show some differences with the BGR models. All information is taken from the report by IfG (2009).

Scope and objectives

The purpose of the geomechanical modelling work was to:

1. Obtain dimensions of long-term stable caverns
2. Obtain operation parameters of the gas buffer, maximum and minimum pressure, withdrawal and injection rates and the allowed time to operate at a minimum storage pressure.
3. Assess gas permeability of surrounding salt
4. Develop a convergence prognosis and its influence at surface
5. Rock mechanical consequences of the worst case scenario: a blow-out

For the purpose of this work only the objectives 1, 3 and 4 are considered.

Model type

Two types of models have been used in this study. First, half a cavern was modelled in an axisymmetric model. Later a 3D model with one half-cavern and two quarter-caverns was created. With the symmetry properties of this block it is possible to reconstruct the entire field in a hexagonal pattern. To illustrate both model types the axisymmetric model is presented in Figure 39 and the 3D model in Figure 40. FLAC is the program that was used to do the calculations.

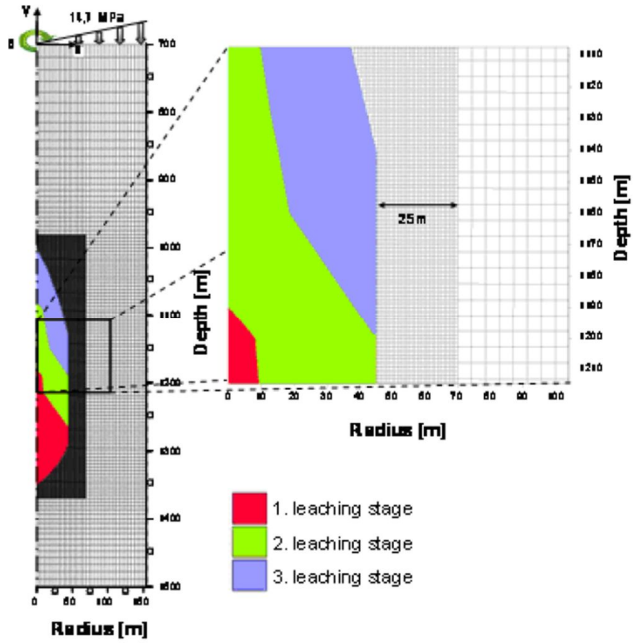

Figure 39: Axisymmetric model of a single cavern for the Aardgasbuffer Zuidwending, (IfG, 2009)

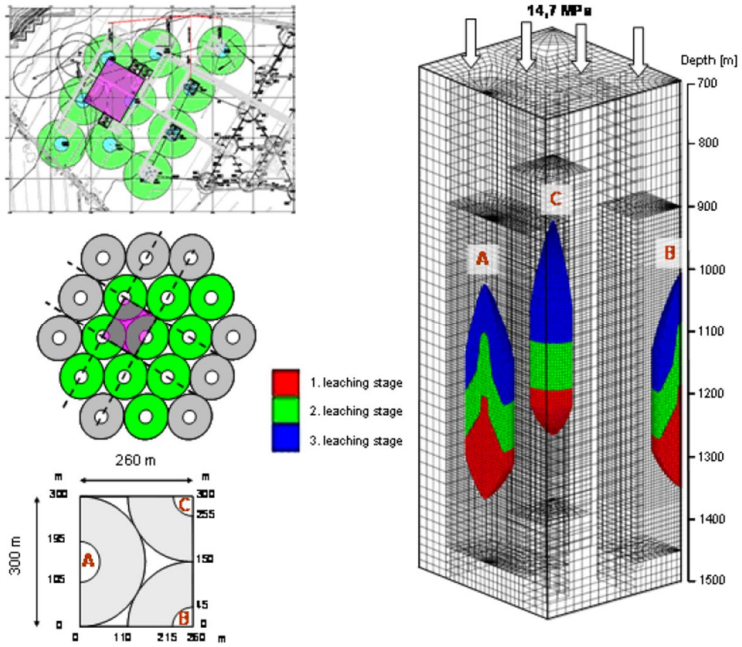

Figure 40: 3D model of Aardgasbuffer Zuidwending (right), planned cavern field (upper left), approximation hexagonal field (middle left) and plan view of the selected portion of the field (lower left), (IfG, 2009)

Calculation variants

Calculation variants for gas storage caverns can be divided into two categories. The first category applies to the leaching operation to develop the cavern to its full dimensions. Basically there is only one calculation variant in this category. In the second category different operation scenarios are considered. For example different minimum and maximum pressures are put in, or different amounts of injection/withdrawal cycles per year are applied. These scenarios are all simulated in an axisymmetric model. The calculation variants in which the effect of different operation modes in neighbouring caverns is investigated, are carried out in 3D models.

Simplifications and assumptions

Dimensions and mesh

Both the axisymmetric and 3D model extend from a depth of 700 m down to 1500 m, see Figure 39 and Figure 40. The axisymmetric model is 70 m wide. The 3D block is 300 x 260 m wide. The models don't extend to the surface. Therefore the presence of the overlying rock salt and overburden is simulated by applying a pressure determined by the specific weight and thickness of the materials to the upper surface of the models. As can be seen in both Figure 39 and Figure 40 the mesh that divides the modelled face or volume into elements is fine near the cavern and it gets coarser towards the edges.

Boundary constraints

The same boundary constraints are applied to both the axisymmetric and the 3D model as in the models discussed in previous sections. In both models the bottom boundary is fixed vertically and the side boundaries are fixed in the direction perpendicular to the boundary.

Geology

The entire model is situated in a body of rock salt, therefore the only material that is modelled is rock salt. It is considered homogeneous.

Cavern development

The development of a cavern is simulated by deleting groups of rock salt elements in 3 stages. In Figure 39 and Figure 40 (right) these three phases are coloured red, green and blue. Each time a portion of a cavern is removed, a brine pressure is applied to the new cavern contour. The brine pressure is calculated with a gradient of 0.012 MPa/m and is specific for each depth.
The shape of the cavern is not purely cylindrical this time. The lower part is parabolic with a maximum diameter of 90 m. This sump phase extends from a depth of 1350 m to 1290. The next part is cylindrical and extends from 1290 to 1125 m depth. In the final phase, a dome shaped roof is leached at a depth interval from 1125 to 1000 m. The black area in Figure 39 is the rock mechanical envelope inside which the cavern needs to stay. It can be seen in Figure 40 that the pillar thickness is 210 m.

Temperature

The variation of temperature T with depth y is built into the model by application of the geothermal gradient with (Eq. 5.1).

$$T(y) = 291 + 0.022 \cdot y \qquad \text{(Eq. 5.1)}$$

This represents a temperature of 291 K, or 18 °C at surface and an increase of 0.022 K per meter of depth increase. The temperature effects of leaching with cold water and later injection and extraction of gas are not taken into account, because they are considered only of influence at the cavern contour.

Material model and parameters

Material models

Since the only material that is present in the model is rock salt, only one material model is needed. The Minkley material model is used here to simulate the behaviour of salt.

Material parameters

The Minkley material model requires quite some input parameters. The values that were used in this model are derived from lab tests on cores of the Zuidwending salt. For the parameters that depend on the value of the plastic strain see Table 7. The input parameters for Burger's material model that is part of the Minkley model are also derived from the lab tests, but conservative values are used in the models. They are listed in Table 8.

ε_p [%]	σ_D [MPa]	σ_{MAX} [MPa]	σ_ϕ [MPa]	σ_Ψ [MPa]	$\tan\beta_0$ [-]
0	5.0	40.0	8.0	-	-
0.2	7.8	41.0	7.1	8.0	0.08
0.5	11.4	42.0	7.1	8.5	0.12
1	14.0	45.0	7.5	8.0	0.16
2	18.0	46.0	7.0	7.0	0.20
3	-	-	-	6.5	0.25
5	22.0	50.0	6.0	6.0	0.30
10	0.0	52.0	2.0	2.86	0.89

Table 7: Minkley model parameters depending on plastic strain, (IfG, 2009)

G^M [GPa]	K [GPa]	η^M [MPa·d]	m [MPa^{-1}]	G^K [GPa]	η^K [MPa·d]
12	20	$1.08 \cdot 10^8$	0.34	63	$4.1 \cdot 10^5$

Table 8: Minkley model parameters, (IfG, 2009)

Evaluation criteria and subsidence prediction

Evaluation criteria

The calculation variants or operation scenarios of the gas storage caverns are evaluated on 3 criteria:

- Gas tightness criterion (applicable to the zone above the last cemented casing shoe)
- Permeability criterion (similar to the fracturing criterion)
- Utilization degree

The gas tightness criterion requires a sufficiently thick zone above the last cemented casing shoe where (Eq. 5.2) is valid. It states that the maximum operation pressure p_{max} of the gas storage may not exceed 85% of the radial stress σ_{xx} acting on the salt-cement-tubing contact.

$$\frac{p_{max}}{0.85} \leq \sigma_{xx} \qquad \text{(Eq. 5.2)}$$

The limit of the permeability or fracturing criterion lies at 25 m. This means that around each cavern there needs to be a 25 m thick zone where this criterion is met. This criterion for gas storage is however not the same as in (Eq. 3.17). In this case it is (Eq. 5.3), which means that the minimum principal stress σ_3 in a zone of at least 25 m thickness must be 10% higher than the maximum operation pressure p_{max}.

$$\frac{\sigma_3}{p_{max}} \geq 1.1 \qquad \text{(Eq. 5.3)}$$

The utilization degree criterion is violated in this case when η > 40% at cavern contour and/or when η > 25% in the bearing elements, such as in pillars or in the salt roof

Subsidence prediction

Based on the calculated volume convergence in the modelling study, and vertical displacement at the top of the model, subsidence is assessed. On one hand there is a volume convergence during the leaching process that takes 3 years. On the other, hand there are different values of volume convergence for all operation scenarios.

Results, conclusions and recommendations

To evaluate whether the different operation scenarios meet the set criteria, images like Figure 41 are made from each scenario. The left-hand image shows that there is a tight zone of 55 m thickness in the roof and 62 m in the pillar. The middle image shows that the permeability is increased near the cavern contour, but this is limited to the zone near the cavern. The utilization degree can be read on the right-hand picture. At the cavern contour it does not exceed the limit of 40% and in the pillar it is less than 25%. In all scenarios, calculated with axisymmetric or 3D models, the criteria remain unviolated.

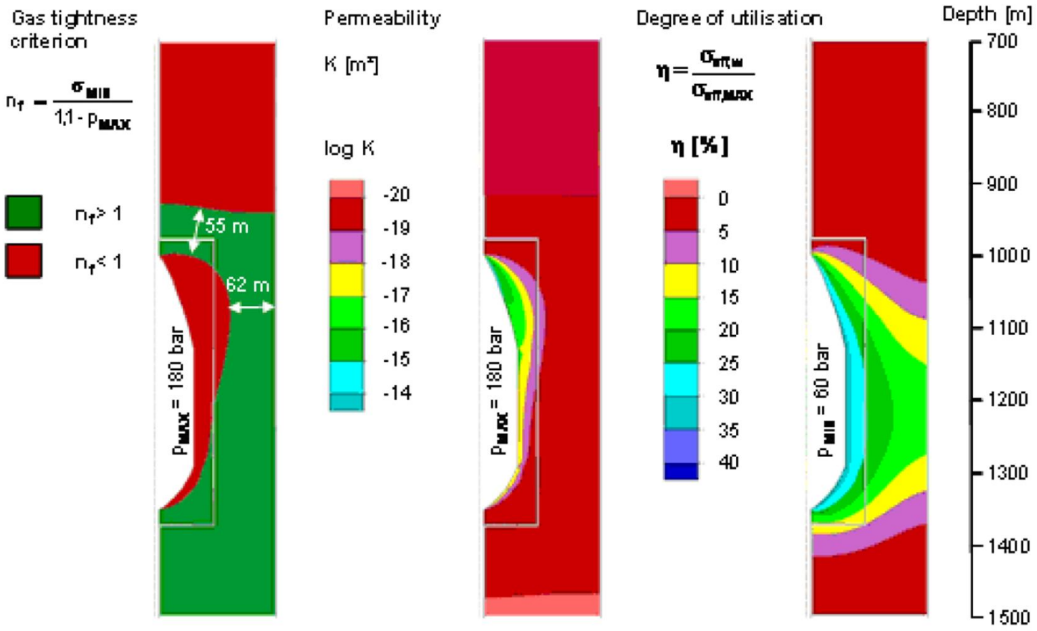

Figure 41: Results after 10 years of storage operation for an operation scenario (1), (IfG, 2009)

The subsidence that is measured after completion of the leaching operation is 4.7 cm at the top of the model with a yearly volume convergence of 2.6 promille. Volume convergence predictions from the

axisymmetric and 3D models that calculated the same scenarios returned very similar results. The factors that cause higher convergence rates are a lower minimum storage pressure and a higher number of injection/withdrawal cycles. A lower minimum pressure means less resistance to cavern convergence. A high number of pressure cycles leads to more primary creep that has a higher creep rate than stationary creep that occurs under constant pressure.

5.4. Subsidence prediction

The official subsidence prediction of the gas storage project has not yet been determined. Since the operatorship of the caverns is transferred from AkzoNobel to Nuon and Gasunie at the start of the first gas fill, AkzoNobel is not responsible for the subsidence predictions any more. In fact the subsidence prediction method for the Heiligerlee and Zuidwending brine fields has already been described in subsection 3.4.1 on the BGR method.

6. Cheshire

AkzoNobel is involved in the development of a gas storage project in Cheshire (UK). The project is in the feasibility study phase. A geomechanical study has been carried out by Atkins. Because the project is in an early phase, only information on the geology and geomechanical model are given in this chapter. There are no details yet about the future leaching process of the caverns.

6.1. Geology

The description of the local geology is derived from the report written about the geomechanical model by Atkins (2012) and is therefore concise.

Gas storage caverns will be leached in the Northwich Halite Formation of Triassic age. The salt deposit is bedded and consists of a top and a bottom sequence of rock salt with interbedded thin layers of mudstone. The two sequences are separated by the 'Thirty foot Marl' mudstone. The thickness of the halite formation is 220 to 230 m in the area. Halite is the main mineral, but there is also 24% mudstone in the formation.

The rock salt formation is underlain and covered by the Sidmouth Mudstone. This is a sequence of mudstone and siltstone. The Sidmouth Mudstone above the salt has an average thickness of 115 m. A deposit of Quarternary age with a thickness of 18 m covers the Sidmouth Mudstone. The Quarternary deposit is glacial till that contains sandy clay and gravel.

In general the layers dip 3 °C towards the Southeast. Although there are large faults at a distance of the site, no indications of significant faulting was found in borehole data or on maps of the site.

6.2. Geomechanical model

The geomechanical study for the Cheshire project was carried out by Atkins. Atkins has experience with salt mining activities in this area and their approach to the geomechanical model is again different than that of the consultants that were mentioned before. Although AkzoNobel is not active in this area (yet), the geomechanical model is discussed here because of the different approach compared to AkzoNobel's current activities. All information is retrieved from the report by Atkins (2012).

Scope and objectives

The geomechanical study was carried out to assess the following three matters of stability.

1. The possibility of collapse of the cavern roof
2. The possibility of collapse of the pillars between the caverns by shear failure
3. The structural interaction between adjacent caverns

Model type

Two 2D plane strain models were used to investigate the points mentioned in the previous subsection. One of these models is shown in Figure 42. This 2D plane strain approach returns more conservative results than an axisymmetric model would, based on results of other relevant studies (Atkins, 2012). The resulting stress states from this model will therefore be an overestimation. Atkins used Phase2 to do the calculations.

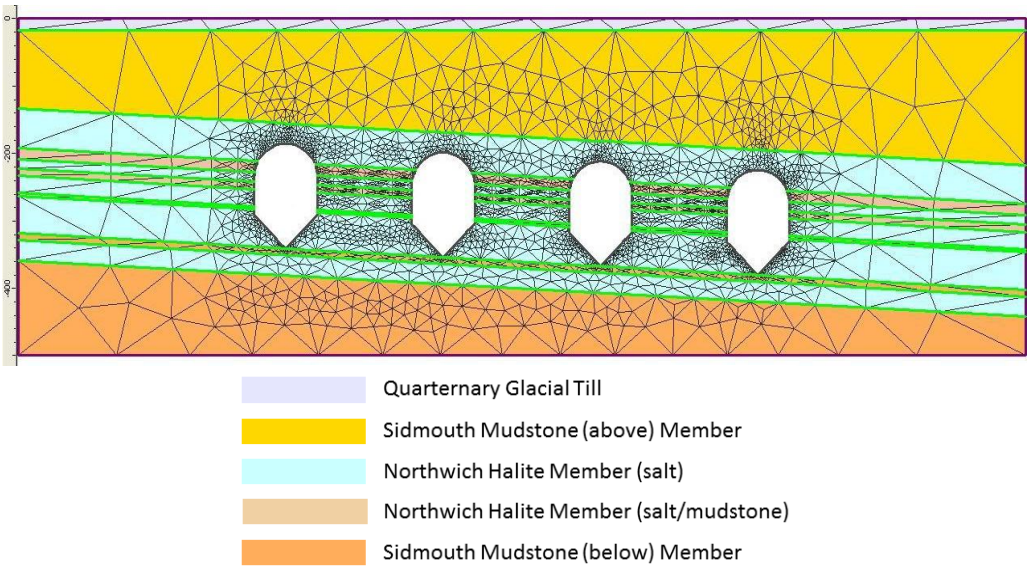

Figure 42: 2D model with 4 caverns aligned in a row, (Atkins, 2012)

Calculation variants

Just like in the geomechanical study of the gas storage project in Zuidwending, field lay-out parameters are not varied. This means that the cavern and pillar dimensions as well as the material properties are fixed. However there are different calculation variants that simulate different loading scenarios (brine pressure, gas fill pressure, the maximum and minimum operation pressure, not necessarily the same situation in all caverns).

Simplifications and assumptions

Dimensions and mesh

The 2D plane strain model in Figure 42 extends from surface (0 m) to a depth of 500 m. In the vertical direction it is 1600 m wide. A second cross section that contains 5 caverns in another row stretches from 0 to 550 m depth and is 2000 m wide in the horizontal direction. Figure 42 shows that the mesh divides the model into triangular elements that are small near the caverns and larger towards the edges of the model.

Boundary constraints

The nodes at the bottom boundary of this model are fixed in the vertical direction and the nodes at the sides in the horizontal direction. The top of the model is free to move in any direction.

Geology

The implementation of different geological layers is also illustrated in Figure 42. From the bottom of the model there is a layer of Sidmouth mudstone, followed by an alternation of rock salt and salt-mudstone of the Northwich Halite Formation in varying thickness. Because the average thickness of the salt-mudstone beds that separate the rock salt layers varies from 4.44 to 16.64 m the presence of these layers is not neglected. The average thickness of the rock salt layers varies from 14.28 to 58.32 m. A second layer of Sidmouth mudstone with an average thickness of 115.40 m covers the uppermost rock salt layer. A Glacial till layer of Quarternary origin with an average thickness of 18 m throughout the area

is at the top of the model. Although the interfaces between the different geological layers are straight lines (simplification) the slight dip of the layers is taken into account in the model.

Cavern development

The whole process of cavern development during the leaching operation is not implemented into the model. This means that the caverns are present instantaneously in the model at their full dimensions (100 m diameter and 150 m height). In one calculation variant the caverns are modelled with the internal pressure of a brine column. This corresponds to the state after completion of the leaching operation. Everything that happened before is not modelled. Neither the volumetric development of a cavern, nor the change of pressure from lithostatic to hydrostatic.

Temperature

Temperature effects are not considered in this model. Under the following heading it will be shown that the choice of the material models that are independent of temperature, implied that temperature effects could be left out of consideration.

Material behaviour and properties

Material models

The point where this study differs most from other studies is that the material model chosen to represent the behaviour of salt does not take creep into account. This choice is supported by the fact that the Northwich Halite Formation is characterized by low creep strain and the stress caused by overburden is limited due to shallow depths. Salt behaviour is modelled with the non-linear Drucker-Prager material model which is suitable for materials that yield under shear loading. This model is also used for the mudstone layers. For the glacial till the Mohr-Coulomb model was used.

Material parameters

The Drucker-Prager and Mohr-Coulomb material models require different parameters. The values are derived from numerous investigations by the University of Newcastle upon Tyne over the last 30 years. Also densities are required to determine the lithostatic stress, as well as elastic parameters for the elastic behaviour of the materials. All parameters are listed in Table 9.

	Glacial Till	Sidmouth mudstone (above salt)	Northwich salt	Northwich salt-mudstone	Sidmouth mudstone (below salt)
ρ [Mg/m^3]	1.90	2.48	2.18	2.34	2.50
E [GPa]	0.004	19.830	36.540	28.230	19.920
ν [-]	0.250	0.249	0.270	0.255	0.240
σ_t [MPa]	0.000	4.373	1.840	3.100	4.360
c [MPa]	0.03	-	-	-	-
φ [°]	26	-	-	-	-
q_ϕ [-]	-	0.976	0.756	0.968	1.180
k_ϕ [MPa]	-	2.582	8.268	5.479	2.689

Table 9: Material parameters of the geological layers in the model (Atkins, 2012)

Evaluation criteria and subsidence prediction

Evaluation criteria

The evaluation criteria in this model are based on safety factors or strength factors. To answer the question whether the stress states that result from the model are acceptable, the strength factor is calculated. Three different cases can be distinguished.

1. Tensile failure occurs when the minimum principle stress σ_3 (which is negative in compression) has a higher absolute value than the tensile strength σ_t (that is negative by convention). When $|\sigma_3| \geq |\sigma_t|$ the strength factor is set to -1, which means tensile failure is expected.
2. Shear failure occurs when the strength factor is between 0 and 1. The strength factor is calculated with the following formula

$$Strength\ factor = \frac{shear\ strengh}{shear\ stress} = \frac{k_\varphi + q_\varphi \frac{I_1}{3}}{\sqrt{J_2}} \qquad \text{(Eq. 6.1)}$$

3. No failure occurs when the strength factor is higher than 1

Subsidence prediction

Subsidence is not assessed in this model. Since creep is not taken into account, cavern convergence is considered not to occur, so it does not cause surface subsidence.

Results, conclusions and recommendations

For each loading scenario the major and minor principle stress contours across the model are plotted, as well as a distribution of the strength factor across the model. The minor principal stress contours indicate for all loading scenarios that the stresses in the cavern roof are compressive, so roof collapse due to tensile failure is not expected. The strength factors in the pillars are also higher than 1 in all cases, so shear failure is also not expected.From the results of the load case where not all caverns were under equal pressure it is derived that no structural interaction occurs between the caverns.

7. Future Haaksbergen brine field

The salt reserves in the mining permits where salt mining currently takes place in Twente will be depleted within 20 years. AkzoNobel has looked for salt mining possibilities in an area close enough to Hengelo to make it feasible to lay pipelines from and to the plant. Northwest of the town of Haaksbergen (around 10 km south of Hengelo), a pillow salt deposit was identified that was subject to more detailed geological research.

A geological study, including a seismic survey and an exploration well, was carried out simultaneously with a generic rock mechanical cavern design, production planning and field lay-out and a subsidence prediction. Based on the updates of the geological model of the salt pillow after the seismic survey and the exploration well, the production plan, field lay-out and subsidence prediction were updated. Since the future Haaksbergen brine field will be geomechanically modelled later on in this work, the geological model of this area will be discussed in more detail than has been done for the other brine fields. All information is extracted from the final report of the geological study by MWH (2011b).

7.1. Geology

The salt pillow near Haaksbergen consists of the Zechstein Z1 Formation, that is also known as the Werra Formation. It has a ridge that extends in the WNW-ESE direction where the salt is at its thickest and its top lies at the smallest depth. This is clearly visible on the maps in Figure 43 and Figure 44.

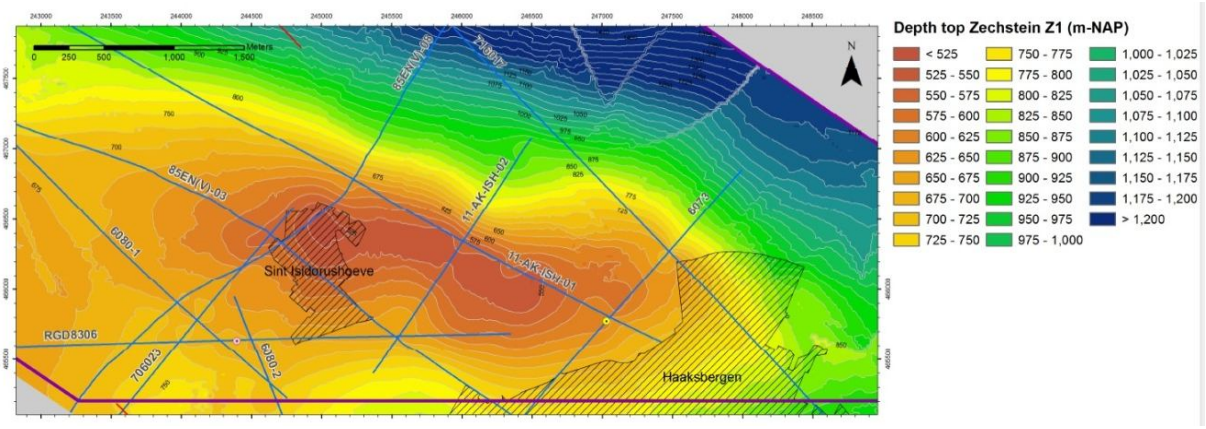

Figure 43: Map of depth of top Z1 Formation in the Haaksbergen salt pillow, (MWH, 2011b)

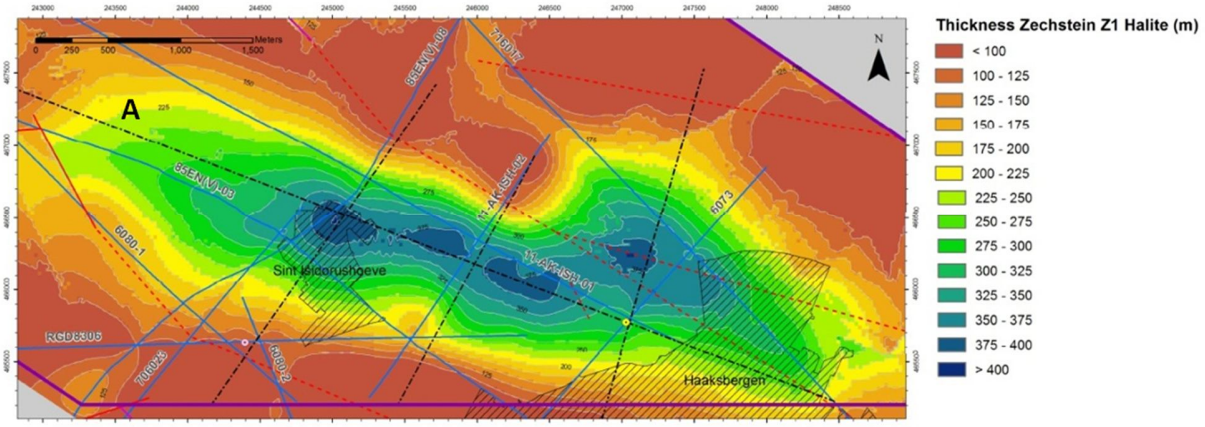

Figure 44: Map of thickness of Z1 Formation in the Haaksbergen salt pillow, (MWH, 2011b)

As can be seen in Figure 44, the thickness of the Z1 salt varies largely throughout the area, from less than 100 m, to over 400 m in the ridge of the pillow. This thickness variation is clearly visible on a profile along the dashed black line indicated with A in Figure 44, this profile is presented in Figure 45.

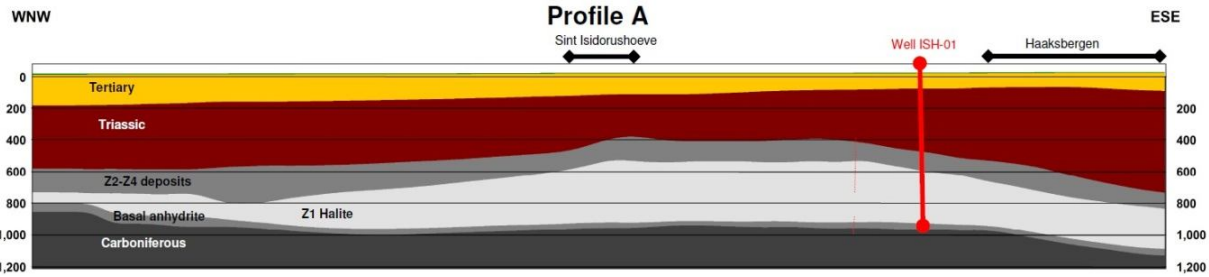

Figure 45: Profile through the Haaksbergen salt pillow, (MWH, 2011b)

The exploration well ISH-01 has been drilled through the Z1 Werra Formation until the Basal anhydrite was reached. Therefore the exploration well did not give information about the Carboniferous that lies underneath the Zechstein formations. However there is an exploration well that was drilled in the past by the Nederlandse Aardolie Maatschappij (NAM) at 2.5 km distance. This well was drilled to reach the Carboniferous deposits and a lithology description says that underneath the Zechstein deposits there are very thin layers of the Coppershale Member (2 m) and Slochteren Formation (1 m), both of Permian age. Deeper, the Carboniferous Tubbergen Formation was found which mainly consists of sandstone.

Between the Carboniferous and Z1 salt, there is the Basal anhydrite that occurs at the base of the Zechstein deposits and is some tens of meters thick. It is overlain by the salt layer of interest, the Z1 salt that varies in thickness from less than 100 m towards the edges of the pillow to more than 400 m in the centre. The Z1 salt is covered by the Z2 to Z4 series that are 100 to 200 m thick and complete the Zechstein deposits. In the exploration well ISH-01 only the Z2 Stassfurt and Z3 Leine Formations were found.

On top of the Zechstein deposits there are thick layers of Triassic deposits. Above the centre of the salt pillow they are 250 to 300 m thick, towards the edges the thickness is up to 600 m. The Triassic deposits

that were found in the exploration well existed mainly of siltstone and claystone and some oolitic limestone, that belong to the Lower Buntsandstein Formation.

The Triassic deposits are unconformably overlain by Tertiary deposits that belong to the North Sea Supergroup and consist of 50 m of sand and 60 m of clay in the exploration well. The Tertiary deposits vary in thickness from 100 to 200 m and are overlain by some thin deposits of Quarternary age.

7.2. Mining

The future Haaksbergen caverns will be leached via wells that will be equipped with a combination of a 7 inch inner string and a 10¾ inch outer string. Injection of water will take place via the annular space between the outer and inner strings and extraction of brine will be via the inner string. Since the depth and thickness of the salt pillow differs per location, all caverns will be developed to a different height. In the generic cavern design, a minimum of 10 m of salt is left at the base of the Z1 salt layer and a minimum of 70 m of salt will be kept in the roof.

During the sump phase the cavern will be developed to a maximum diameter of 125 m and a height of 35 m, this will result in a cone-shaped sump phase. Depending on the local thickness of the salt, a cylindrical part will be developed subsequently. In the last phase of the life-time of a cavern a dome-shape roof with a radius of 62.5 m will be leached. A representation of this cavern design is given in Figure 46 (right) The described dimensions and shape form the so-called rock-mechanical envelope. In practice these ideal shapes will not be reached, but it is essential that the cavern stays within this envelope to guarantee cavern stability. Blanket oil will be used to control cavern development.

7.3. Geomechanical model

The process of geomechanical modelling and subsidence predictions for the future Haaksbergen brine field has gone through several phases. First a generic cavern design was made based on material parameter values from literature. A field lay-out of caverns in a hexagonal grid was made based on a first geological model. The subsidence prediction for this cavern field by KBB (2010) indicated very large amounts of subsidence (0.6 m in 50 years). The subsidence prediction and the geomechanical model were updated after the geological model was improved by the results of a seismic survey and an exploration well. From the exploration well also material properties for the salt became available.

IfG has made the geomechanical model and carried out lab test on the salt cores from the exploration well. KBB was hired to do the subsidence prediction based on the field lay-out and production planning that were developed by the German underground engineering consultant DEEP.

Scope and objectives

The purpose of the studies by IfG (2010) and IfG (2012a) was to establish a geomechanical model with a generic cavern of appropriate dimensions on which the complete cavern field could be based. The volume convergence that resulted from this study was an input parameter to make the most realistic subsidence prediction. In the following description mainly the geomechanical models will be discussed. Subsidence will only be discussed in the parts that are specifically on subsidence.

Model type

The geomechanical model is an axisymmetric model that incorporates half a cavern and half a pillar horizontally. The model boundary that is at the axis of the cavern is the rotation axis. The other vertical boundary acts as a symmetry axis. When the model is mirrored in this axis the presence of a neighbouring cavern is simulated. FLAC was used to do the geomechanical calculations.

Calculation variants

There are basically two models with two calculation variants each. The first model is the initial generic cavern, the second one is the new generic cavern that was developed after several updates of the geological model and the production plan. In the first model only one set of dimensions for the generic cavern is assessed by IfG (2010). In the second model some adjustments have been made to make the model match with the new geological model and material parameters. This resulted in a new convergence rate. Since only a short memo was written by IfG (2012a) about the new model, it is assumed that all differences between the two models are mentioned in this memo. Every aspect that remained unaddressed is assumed to be equal to the first model. The two calculation variants in each model differ in wellhead pressure. One variant has no extra well head pressure, so the pressure in the cavern is the pressure of the brine column only. The other variant has 5 MPa of well head pressure that is added to the brine pressure.

Simplifications and assumptions

Dimensions and mesh

The first model contained half a cavern and half a pillar in a 158 m wide model, see Figure 46 (left). In the vertical direction the model extended from 500 to 1100 m depth. The top of the model was in the Lower Buntsandstein Formation, the bottom in the Upper Carnboniferous formation that lies underneath the salt. Since 500 m of overlying materials are not physically modelled, they are represented by a pressure of equal magnitude that is applied to the top of the model (IfG, 2010). The second model contains a cavern of 125 m diameter and the model extends from 0 m at ground level to 1300 m depth IfG (2012a). Since there are no pictures available from the meshed models, nothing can be said about the applied mesh here.

Boundary constraints

The boundary conditions of this model are the same as in all of the other models. The vertical and bottom boundaries are fixed in the direction perpendicular to the boundaries.

Geology

The first model started at the bottom with a 100 m thick layer of Carboniferous from 1100 to 1000 m depth followed by 50 m of Z1 anhydrite, 270 m of Werra salt, 140 m of other Zechstein deposits and 40 m of Lower Buntsandstein, see Figure 46 (left). The second model is much more general. From a depth of 1300 m to 1017 m there is the ‘underlying formation’. The salt extends from 1017 to 642 m and from 642 depth to surface level there is the ‘overlying formation’, see Figure 46 (right). It represents one of the largest and deepest caverns in the field (IfG, 2012b). Horizontally the model has a radius of half a cavern and half of the new pillar width of 450 m. The pillar width has been increased to calculate a new volume convergence. The updated production plan shows that instead of each cavern having 6

neighbours in a hexagonal field pattern, the new cavern will have maximum 4 neighbours. This is simulated by applying a bigger pillar width between the caverns (IfG, 2012b). In both models all materials are considered homogeneous.

Cavern development

The volumetric development of the caverns is not implemented in both models. From the first moment the caverns are present in the models at their full dimensions. The pressure of a brine column acts on the cavern contours. The magnitude of this pressure varies with depth, but not with time. In the variants with a well head pressure, 5 MPa is added to the brine pressure.

As can be seen in Figure 46, the cavern designs are not the same in both models. In the first model the lower part of the cavern is 30 m high and shaped parabolically to a diameter of 135 m. On top of this there is a 70 m high cylindrical part and a 65 m high parabolic roof. Below the cavern 35 m of salt are left and 70 m above the roof. In the second model the lower part is conical and over a height of 35 m the diameter is developed from 0 to 125 m. Then an almost 200 m high cylindrical part follows and the roof is dome-shaped with a radius of 62.5 m. There is 10 m of salt left below the bottom of the cavern and 70 m above the roof.

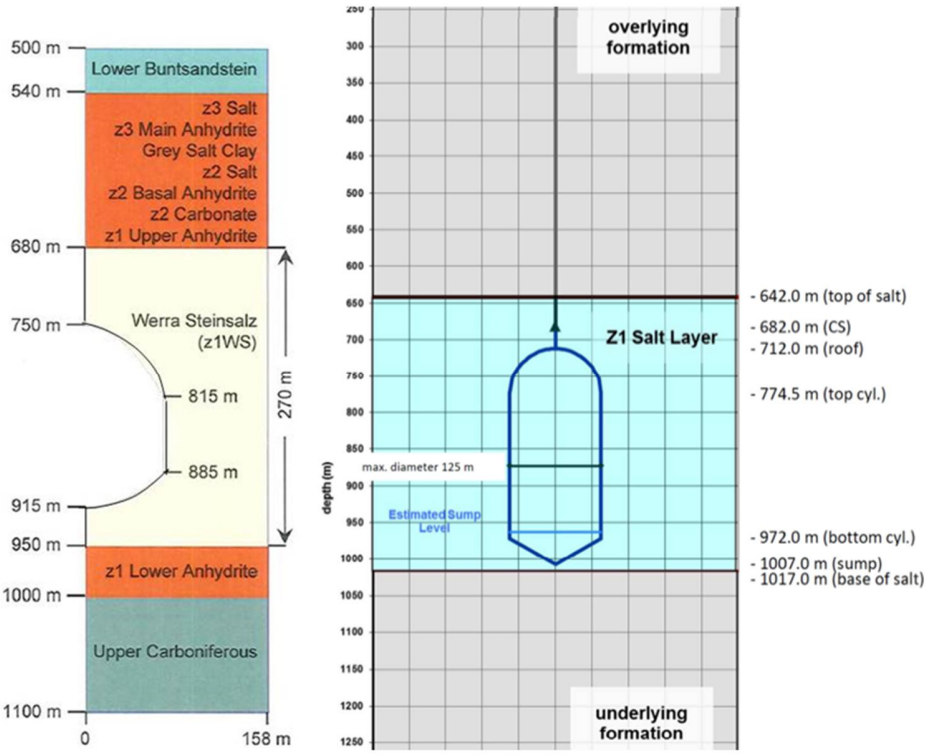

Figure 46: Sketches of first (left, (IfG, 2010)) and second Haaksbergen model (right, (IfG, 2012a))

Temperature effects

In the reports by IfG (2012a) and IfG (2010) it is not mentioned that temperature effects are considered in the models.

Material behaviour and parameters

Literature values were used for the material model parameters in the first model. In the second model the values for salt were updated with the results from tests on the Haaksbergen salt from the exploration well. Table 10 and Table 11 list the strength and creep parameter values that were used in the first model. The Mohr-Coulomb parameters for the non-salt materials were a cohesion of 5 MPa and a friction angle of 45°.

ε_p [%]	σ_D [MPa]	σ_{MAX} [MPa]	σ_ϕ [MPa]	σ_Ψ [MPa]	$\tan\beta_0$ [-]
0	4.0	31.2	1.1	0.2	00
0.2	-	-	-	2.0	1.50
1	16.8	33.6	2.2	1.2	2.20
2	20.4	36.0	3.0	1.1	2.95
3	22.0	36.4	3.0	-	-
5	-	-	-	1.0	4.0
7	24.3	43.6	3.8	-	-
10	19.2	37.2	0.6	-	-
13	0	46.4	0.8	-	-
15	0	92.0	5.0	-	-

Table 10: Literature strength parameters for rock salt used in the first Haaksbergen model, (IfG, 2010)

G^M [GPa]	η^M [MPa·d]	m [MPa^{-1}]	G^K [MPa]	η^K [MPa·d]
$1.0 \cdot 10^4$	10^7	0.3	$6.3 \cdot 10^4$	$1.7 \cdot 10^5$

Table 11: Literature creep parameters for rock salt used in the first Haaksbergen model, (IfG, 2010)

The different strength and creep parameters that resulted from lab tests on rock salt from the exploration well, are listed in Table 12 and Table 13.

ε_p [%]	σ_D [MPa]	σ_{MAX} [MPa]	σ_ϕ [MPa]	σ_Ψ [MPa]	$\tan\beta_0$ [-]
0	8	40	8	-	-
0.2	12	42	8	0.25	1.8
0.4	-	-	-	0.4	2.0
0.5	14	43	8	-	-
1	20	40	16	-	-
2	25	44	8	0.6	2.5
4	28	45	3	0.8	2.8
8	2	50	0.8	2.5	1.8
12	0	58	1.2	2.2	2.0

Table 12: Strength parameters for rock salt used in the second Haaksbergen model, (IfG, 2012b)

η^M [MPa·d]	m	G^K [MPa]	η^K [MPa·d]
$1.86 \cdot 10^6$	0.164	$1.51 \cdot 10^4$	$2.87 \cdot 10^4$

Table 13: Creep parameters for rock salt used in the second Haaksbergen model, (IfG, 2012b)

Evaluation criteria and subsidence prediction

Evaluation criteria

The integrity and stability of the generic cavern are evaluated based on two criteria. The integrity is evaluated by the fracture criterion. The stability of the caverns and pillars is evaluated by the utilization degree. At the contours $\eta \leq 40\%$ must be valid and in the supporting elements $\eta \leq 25\%$.

Subsidence prediction

The volume convergence that originates from the geomechanical model is used as an input in the Salt-subsid method. In the software also the angle of the cones β is varied and the factor a that determines the amount of convergence volume that is translated to surface.

Results, conclusions and recommendations

Both the first and second model guarantee stability of the cavern and impermeability of the rock salt surrounding the cavern.

7.4. Subsidence prediction

In the subsidence prediction that is included in the mining plan that needs to be approved by the minister of economic affairs, who is advised by SSM, subsidence caused by the first 12 caverns of the Haaksbergen brine field is included. As mentioned before the prediction was made using the Salt-subsid method. A number of scenarios were calculated to come up with the subsidence prediction by KBB (2012), see Figure 47. This scenario was chosen to be the most likely. The other scenarios are kept in case it turns out that, for example, the convergence rate is much higher than anticipated. After some caverns will have been developed it will be possible assess the reliability of the current prediction and it will be decided whether an update is necessary.

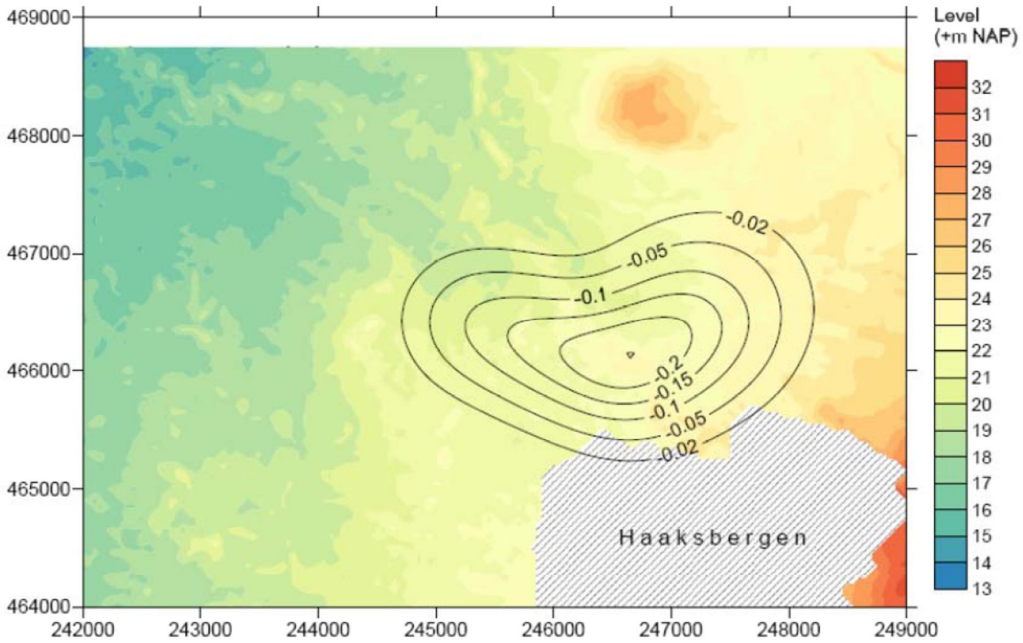

Figure 47: Subsidence prediction in m, used in the current mining plan for 12 Haaksbergen caverns, from KBB (2012)

8. Combined model of the Haaksbergen brine field

As has been described in the previous chapter, the development plan for the future Haaksbergen brine field has been updated every time new information became available. The geomechanical model and the subsidence prediction form two separate components that support the brine field development plan. In the geomechanical model the stability of a cavern of certain dimensions in a salt body that possesses certain properties has been tested. The cavern convergence rate was derived from this model and used as input for the analytical subsidence prediction that was carried out in Salt-Subsid.

The fact that AkzoNobel's very first development plan of the Haaksbergen brine field lead to an unacceptable high amount of subsidence, see 1.1, has raised the curiosity within AkzoNobel to get more insight in the factors that influence cavern convergence and subsidence. At the moment the effect on the subsidence prediction of any change in the geomechanical model (for example in cavern dimensions or material parameters) can not immediately be recognized. When the geomechanical model is updated, the subsidence prediction has to be updated subsequently. In other words two steps need to be taken to investigate the sensitivity of cavern convergence and subsidence to different parameters. Since AkzoNobel hires two parties (IfG as a consultant for geomechanical modelling and KBB for subsidence prediction), it would be a time-consuming and costly process to perform a sensitivity analysis that involves a large number of parameters.

To be able to identify the effect of parameter variation on cavern convergence and the formation of a subsidence bowl, it is required to make a geomechanical model from which these two results can be derived. In this study the finite element software package DIANA (**Di**splacement **Ana**lyzer) was used for this purpose. The choice for DIANA was based on availability of a license via TU Delft, the availability of the Fokker creep model that is used to model salt behaviour and, most importantly, the willingness of the company TNO DIANA to provide help and advice in the modelling process.

Two types of analyses were carried out in this study:

- An axisymmetric analysis on a single cavern
- A plane strain analysis on two caverns

In the following sections the modelling process of both analyses will be discussed. Following the same line as described in subsection 3.3.1 and used in the previous chapters that described the existing geomechanical models, it will be extensively explained how both models are built up. The last two components of the modelling process will be discussed in the chapters on results and conclusions that will follow.

For a concise description on the process of developing and running a model in DIANA, reference is made to Appendix B. The data files and command files of all models that were developed in this work are available on CD-ROM.

8.1. Single cavern analysis

8.1.1. Scope and objectives

The objective of the single cavern analysis was to identify the effect of different parameters on the cavern convergence and the development of a subsidence bowl. The parameters of interest are

- Cavern diameter
- Thickness of salt roof and salt floor
- Salt properties (elastic and creep)
- Overburden properties

It was chosen to investigate the effect of these parameters on a single cavern to limit the complexity of the model. This makes it easier to make adjustments for the different calculation variants and it limits calculation time.

8.1.2. Model type

Because only one cavern needs to be modelled, an axisymmetric model is built. The vertical line through the heart of the cavern acts as the axis around which the model will be rotated.

8.1.3. Calculation variants

The calculation variants all differ in one aspect from the base case. In this base case cavern dimensions and material properties are chosen in accordance with the design principles by IfG (cavern diameter, thickness of salt roof and floor), results of laboratory tests (properties of salt) and the proximity of the Hengelo brine field (overburden parameters). The base case parameters are listed in Table 14 below. It is followed by Table 15 where it is listed for every calculation variant which parameter is changed. All other parameters keep the value of the base case.

Parameter	Value [unit]
Cavern diameter	125 [m]
Thickness salt roof	72.5 [m]
Thickness salt floor	10 [m]
Creep parameter A	0.0012 [s^{-1}]
Creep parameter n	3 [-]
Elasticity modulus salt	30 [GPa]
Elasticity modulus overburden unit Z2-Z4	15.5 [GPa]
Elasticity modulus overburden unit Triassic	5.5 [GPa]
Elasticity modulus overburden unit Tertiary +Quarternary	34 [MPa]

Table 14: Base case parameters and values

Calculation variant name	Varied parameter	Value varied parameter [unit]
002_D075	Cavern diameter	75 [m]
001_BASE	Cavern diameter	125 [m]
004_D150	Cavern diameter	150 [m]
005_D175	Cavern diameter	175 [m]
005_SR030	Thickness salt roof	30 [m]
006_SR050	Thickness salt roof	50 [m]
001_BASE	Thickness salt roof	72.5 [m]
007_SR090	Thickness salt roof	90 [m]
008_SR110	Thickness salt roof	110 [m]
040_SF00	Thickness salt floor	0 [m]
041_SF05	Thickness salt floor	5 [m]
001_BASE	Thickness salt floor	10 [m]
042_SF20	Thickness salt floor	20 [m]
043_SF40	Thickness salt floor	40 [m]
012_A12E-5	Creep parameter A	0.00012 [s^{-1}]
013_A06E-4	Creep parameter A	0.0006 [s^{-1}]
001_BASE	Creep parameter A	0.0012 [s^{-1}]
0141_A03E-3	Creep parameter A	0.003 [s^{-1}]
016_N1	Creep parameter n	1 [-]
017_N2	Creep parameter n	2 [-]
001_BASE	Creep parameter n	3 [-]
0181_N3_5	Creep parameter n	3.5 [-]
020_ES10	Elasticity modulus salt	10 [GPa]
021_ES20	Elasticity modulus salt	20 [GPa]
001_BASE	Elasticity modulus salt	30 [GPa]
023_ES60	Elasticity modulus salt	60 [GPa]
024_EZ2Z405	Elasticity modulus Z2-Z4	5 [GPa]
025_EZ2Z410	Elasticity modulus Z2-Z4	10 [GPa]
001_BASE	Elasticity modulus Z2-Z4	15.5 [GPa]
026_EZ2Z420	Elasticity modulus Z2-Z4	20 [GPa]
027_EZ2Z430	Elasticity modulus Z2-Z4	30 [GPa]
028_ETRIA02	Elasticity modulus Triassic	2 [GPa]
029_ETRIA035	Elasticity modulus Triassic	3.5 [GPa]
001_BASE	Elasticity modulus Triassic	5.5 [GPa]
030_ETRIA075	Elasticity modulus Triassic	7.5 [GPa]
031_ETRIA11	Elasticity modulus Triassic	11 [GPa]
032_ETERT15	Elasticity modulus Tertiary + Quarternary	15 [MPa]
033_ETERT25	Elasticity modulus Tertiary + Quarternary	25 [MPa]
001_BASE	Elasticity modulus Tertiary + Quarternary	34 [MPa]
034_ETERT50	Elasticity modulus Tertiary + Quarternary	50 [MPa]
035_ETERT75	Elasticity modulus Tertiary + Quarternary	75 [MPa]

Table 15: Calculation variants in single cavern analysis

A number of remarks have to be made about this table of final calculation variants.

1. In the series of different cavern diameters the variant (number 003) where the diameter is 100 m is missing, because for this calculation variant the calculations did not converge. The cause of this will be discussed in 9.2.1.
2. In all cases where dimensions are changed (002-008 and 040-043) the cavern volume automatically changes as a consequence. The effect of this will be discussed in 9.2.1.
3. For the spread of the creep parameter values, the initial objective was to have the extremes of parameter *A* ten times smaller and ten times larger than in the base case. Smaller values than in the base case did not give a problem. However for the value that was 5 times higher (0.006 s^{-1}) than the base case, the calculations did not converge. Apparently the deformations caused by this higher creep rate were too large for the model. In order to still have a variant with an *A*-value that is higher than in the base case, the variant 0141 was assigned the value $A = 0.003\ s^{-1}$. The same problem occurs with the creep parameter *n*, which is the stress exponent in the creep law and has the value 3 in the base case. For $n = 4$ the calculations did not converge, therefore the variant 0181 with $n = 3.5$ was run to have results for a higher *n*-value than the base case.
4. In the variation of the elasticity modulus of salt it was initially planned to have a variant (no. 022) with a value $E_{Salt} = 45$ GPa. Since the results of the base case ($E_{Salt} = 30$ GPa) and the variant 023 with $E_{Salt} = 60$ GPa did not show a big difference, it was considered unnecessary to run the model with the value in between.
5. For the variation of the E-modulus of the three overburden units (024-035) the aim was to have half the base case value as the lower extreme and twice the base case value as the upper extreme. Since no tests have been carried out on the overburden material, assumptions had to be made regarding its density and elastic properties. The values of the E-moduli that were chosen in the base case were taken from geomechanical models of the Hengelo brine field where the properties of the overburden have been measured in laboratory tests. Because of the lack of information about the overburden, halving and doubling the E-moduli to get a range, incorporates the uncertainty about this parameter more realistically than looking at the variation of test results of the overburden of the Hengelo brine field.

8.1.4. Simplifications and assumptions

In Figure 48 the axisymmetric single cavern model with the base case cavern dimensions is presented.

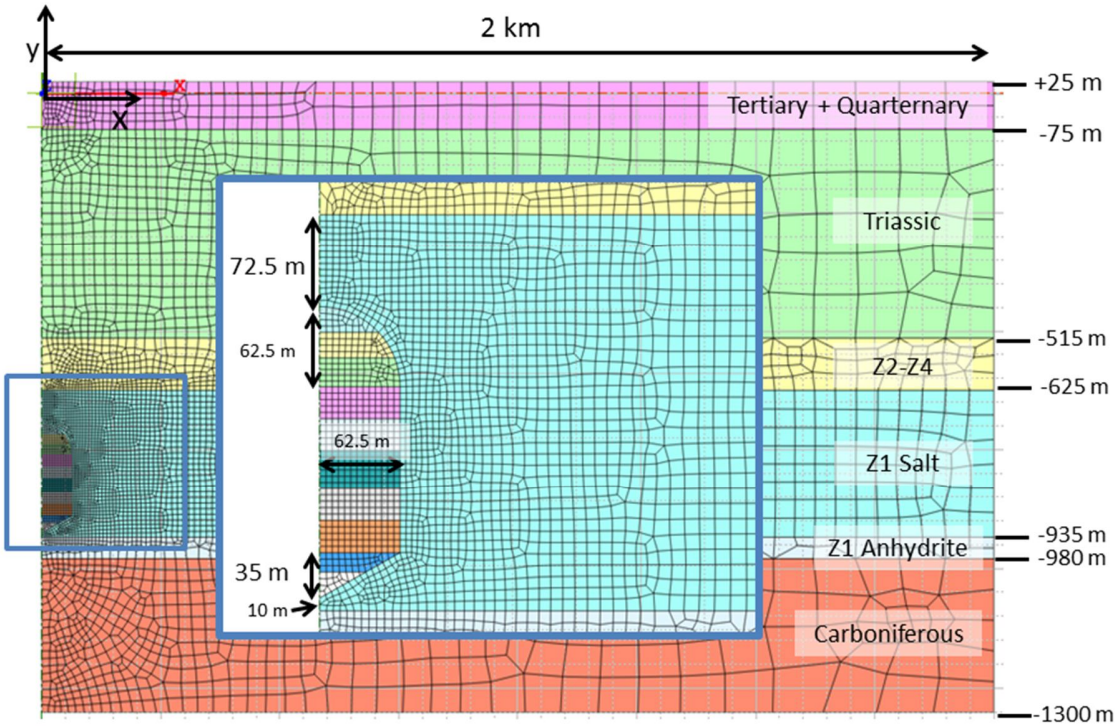

Figure 48: Axisymmetric model of the base case

Dimensions and mesh

Figure 48 shows the dimensions that were used for this geomechanical model. The horizontal extent depends largely on the depth of the cavern bottom. A general first approximation of the horizontal extent of the subsidence bowl is equal to the depth of the bottom of the cavern. In this case the cavern bottom lies at a depth of (925 + 25) 950 m below surface. Therefore it is expected that the subsidence bowl will extend around 950 m horizontally at surface. To make sure that the boundary of the model is at a sufficiently large distance to have negligible influence on the displacements in the model, this distance is doubled and rounded to 2 km.

It is important in the choice of the depth of the bottom of the model that there is sufficient distance between the bottom of the model and the bottom of the cavern. The effect of stress redistribution around the cavern should be negligible at the bottom boundary of the model. In this case the bottom boundary is at -1300 m, which is 375 m below the bottom of the cavern. In the current geomechanical model for the Haaksbergen area the bottom boundary of the model is at -1300 m as well (IfG, 2012a).

The elements of the smallest size are situated in the cavern and in its vicinity and are 5 x 5 m. Towards the edges the mesh is allowed to become coarser to a maximum size of about 100 x 100 m. In order to obtain this, the lines that form the boundaries between groups of elements were assigned mesh seeds. After applying the mesh seeds manually, a mesh that matches these seeds on the edges was generated. It determines the most suitable mesh for the inner area by itself.

In Figure 48 it can be seen that the thickness of the salt roof is 72.5 m. This differs from the 70 m of the generic cavern design. It was initially decided to use this roof thickness, because of the chosen 5x5 m mesh size. The radius of the spherical roof is 62.5 m. Having a 72.5 m thick salt roof makes the whole mesh fit better. Later it became clear that this was unnecessary, because the mesh would have adapted to it.

Boundary constraints

Figure 49 shows the boundary constraints that are applied to the axisymmetric single cavern model. It can be seen that the nodes on the left and right hand vertical boundary are fixed horizontally. On the bottom boundary the nodes are fixed vertically.

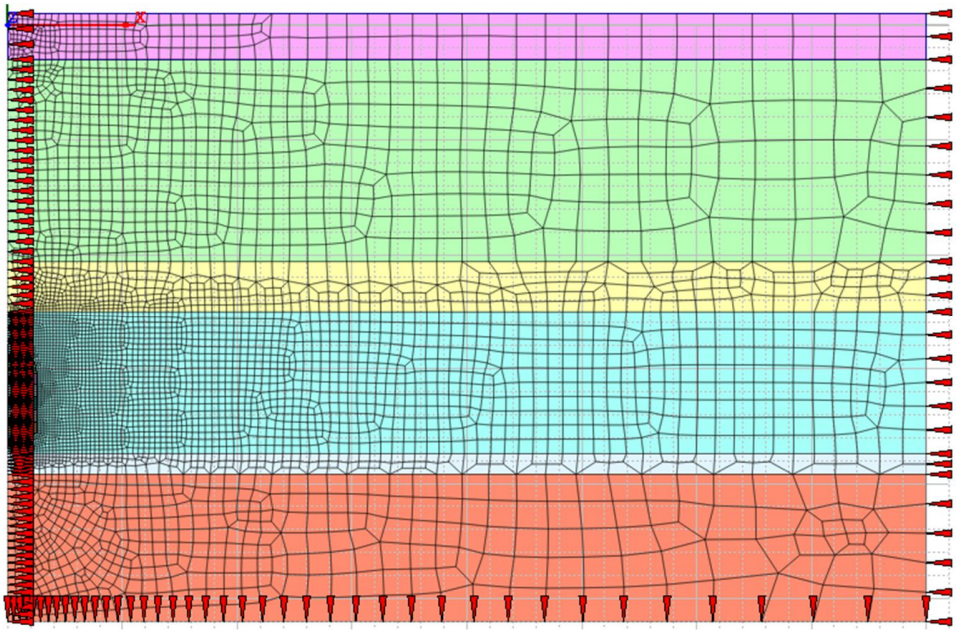

Figure 49: Boundary constraints applied to the single cavern model

Geology

As can be seen in the geological cross section of Figure 45, the geology is not continuous across the future brine field. Because it is a pillow salt deposit, its thickness varies over the area, as well as the thickness of the different overburden units. The depth and thickness for the geological units in this geomechanical model were derived from an interpolation of the contour lines of the different layer interfaces provided by MWH (2011b). The location of the exploration well ISH-01 was chosen, because the salt properties were determined from tests on cores that were retrieved from this well.

In the axisymmetric model the layers are perfectly horizontal and parallel, which is not the case in practice. If the layers would be inclined in the model, rotation around the *y*-axis would result in a mirrored inclination at 180° of rotation, as illustrated in Figure 50. This would model a cavern that is situated exactly in the centre of a perfectly axisymmetric pillow salt deposit. For two reasons this does not apply to the Haaksbergen situation. First of all the salt pillow is not axisymmetric, it has a ridge that stretches roughly in East-West direction. Also, the location of the exploration well (where the depth intervals in the axisymmetric model originate from) is not in a central location in the salt pillow. As can

be seen in the cross section of Figure 45 the salt gets thicker in WNW direction and thinner in the opposite ESE direction.

Due to the lack of symmetry in the salt deposit it is hard to decide how inclined layers should be incorporated into the model in order to be representative for the Haaksbergen situation. For this reason it was decided to model only perfectly horizontal and parallel layers.

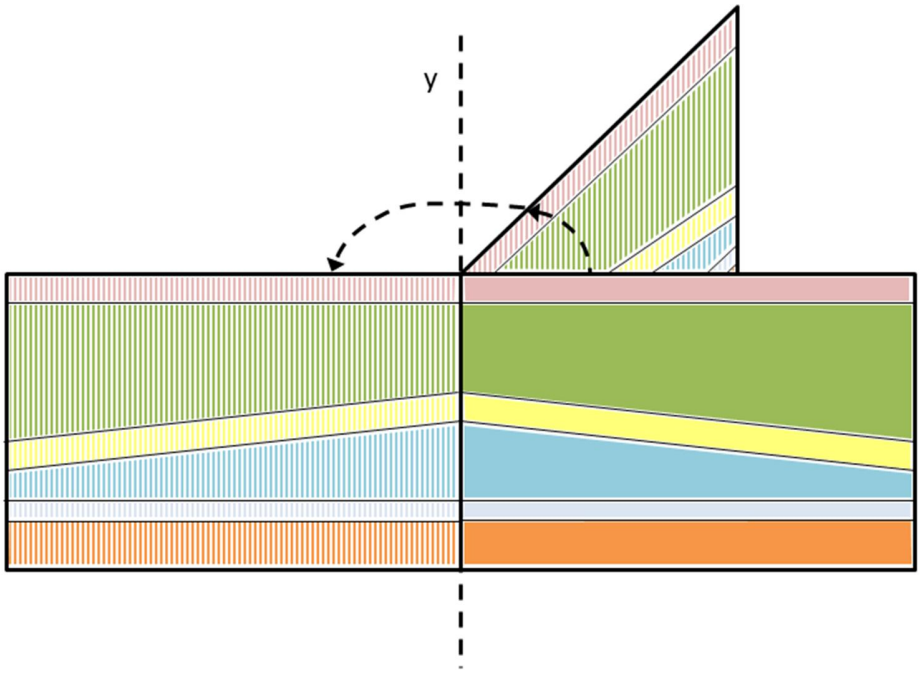

Figure 50: Rotation of inclined layers in an axisymmetric model

From the log of the exploration well, it is known that the overburden unit that is called Triassic (green in Figure 48) consists of different lithologies, like claystone, siltstone and limestone (MWH, 2011a). The same applies to the other overburden units. Since the geological model only provides the layer interfaces Top Triassic, Top Zechstein, Top Z1 salt, Bottom Z1 salt and bottom Zechstein (MWH, 2011b), no differentiation is made inside the units that are separated by these interfaces. Each unit gets their own set of material properties.

An important simplification of the geological situation is that faults are left out of consideration. This means that in the model the only discontinuities are the layer interfaces, but these are not modelled as slide planes. Therefore sliding of a layer with respect to an adjacent layer does not occur.

Cavern Development

The cavern develops in ten phases in the course of the model. In every phase a group of elements becomes inactive to represent a part of the cavern. A pressure that is equal to the pressure of a static brine column at the local depth is applied to the wall and roof of the cavern in each stage. Figure 51 shows the cavern at different stages of its development.

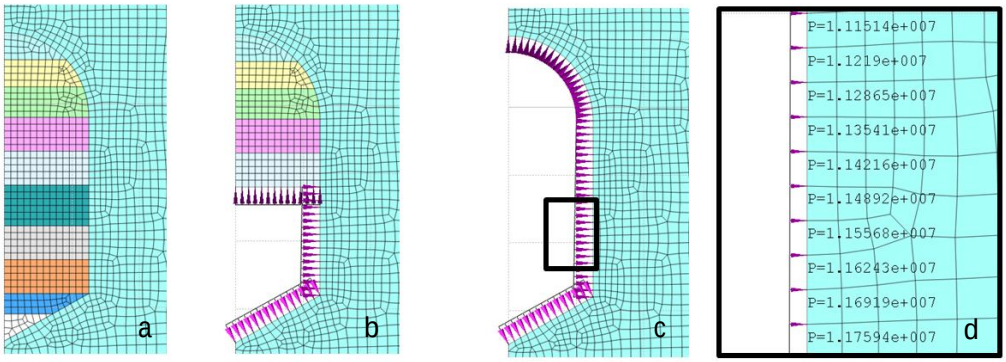

Figure 51: Implementation of cavern development, (a) phase 0, (b) phase 5, (c) phase 10 and (d) zoom in on cavern wall of phase 10 with increasing pressure values with increasing depth

As can be seen in image d in Figure 51, which zooms in on the cavern wall of image c, the pressure increases with depth. The model is able to calculate the pressure that is representative for a brine column at each depth with a function called 'brinepressure' that was implemented in the model. This function uses the depth *y* as independent variable. In Figure 52 it can be seen how this function is specified. Behind this is the pressure gradient for brine which is 0.012 MPa/m. With every meter depth, the pressure increases 0.012 MPa. At surface (+25 m) the pressure is 0 and a brine column that would reach the bottom boundary of the model (-1300) would be (1325 x 0.012) at 15.9 MPa.

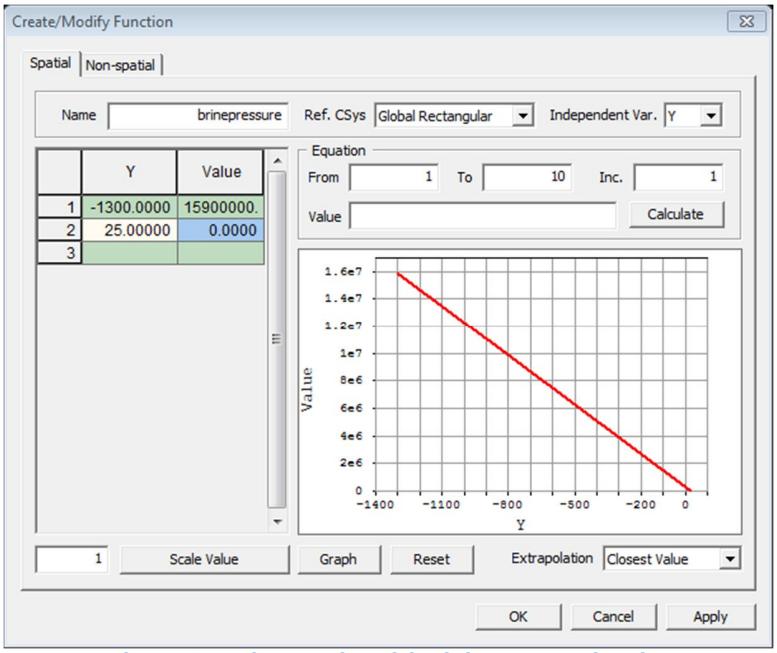

Figure 52: Implementation of the 'brinepressure' function

The development of the cavern in time is presented in Figure 53. Cavern development starts in the year 2015 and every year a new phase starts. In every of these 10 phases, 12 time steps of one month each are taken to give the model the opportunity to show the creep behaviour. After the cavern has reached its full dimensions in ten years, the model keeps on running for 25 years to the year 2050 to be able to investigate the long term behaviour. In this last stage, time steps of one year are taken.

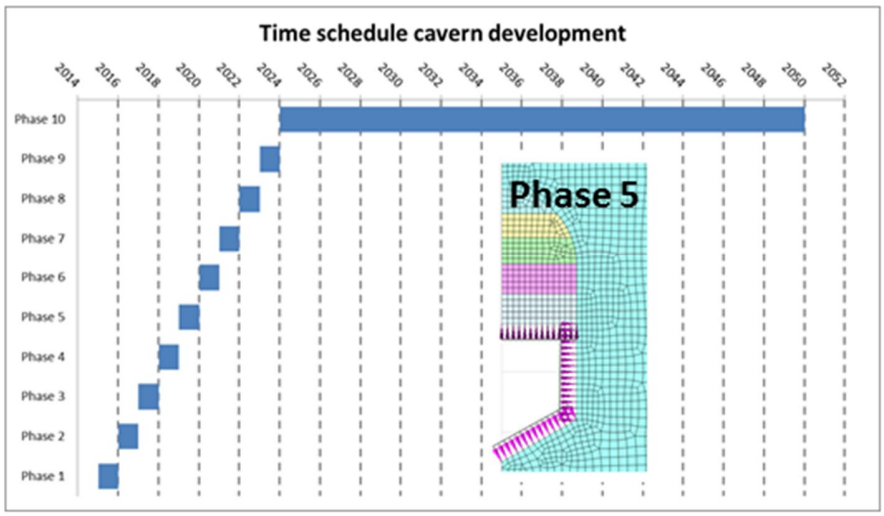

Figure 53: Time schedule of cavern development from 2015 to 2050, including image of cavern during phase 5

Temperature

According to Fokker's creep law, creep rate depends on temperature. In the subsurface temperature increases with depth. The model is able to calculate the temperature at each depth with the implemented function 'temperature' that has the independent variable *y*. The implementation is similar to that of the 'brinepressure' function, as can be seen in Figure 54.

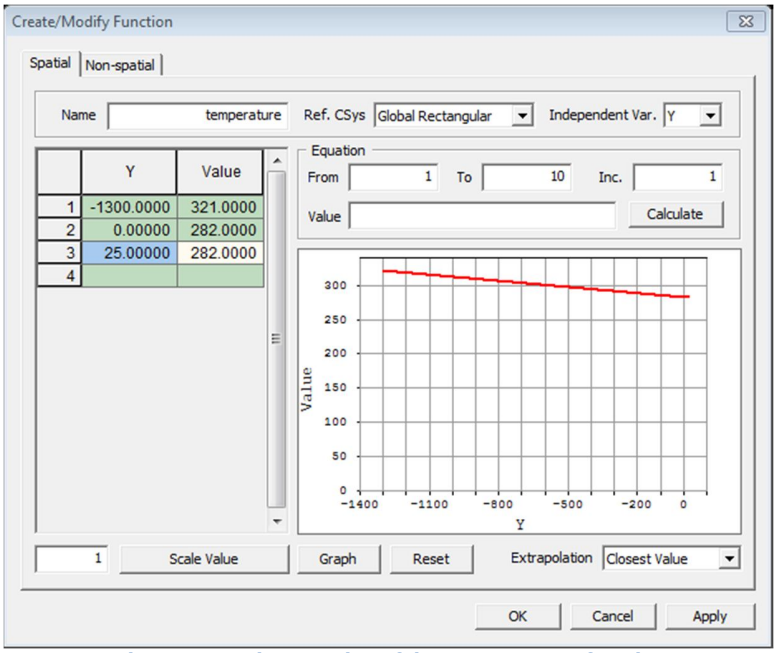

Figure 54: Implementation of the 'temperature' function

The temperature function is implemented to have the top 25 m at a constant temperature of 9°, or 282 K. Below this level, temperature increases with 3° every 100 m to reach 321 K at the bottom of the model. The effect of the injection of relatively cold water into the cavern is not considered in the model.

8.1.5. Material behaviour and parameters

Material models

Due to the lack of information about the rock mechanical properties of the different overburden units, it is hard to determine which material model fits these materials best. A choice for any material model that takes plastic deformation into account could not be supported by data that show the plastic behaviour of the material. For this reason it was decided to model the behaviour of all non-salt materials linear elastically. This way the least material parameters are required and it avoids having a large number of input parameters of which the magnitude is unknown.

The creep behaviour is modelled by Fokker's creep law for secondary creep. The reason to use this model is its availability in DIANA. A disadvantage of using this material model is that the required material parameters are not immediately available. From the lab tests on the salt from the exploration well the parameters of the Minkley model have been derived. There is no direct relation between the Minkley model and Fokkers creep model. Therefore a way had to be found to derive the parameters of Fokker's creep law from the test results of the Haaksbergen salt. Section 8.3 in this chapter is dedicated to the description of how this calibration was carried out.

Material Parameters

The elastic material parameters that were used are listed in the Table 16 below. They are chosen equal to the values that are known for the geological layers in the Hengelo brine field. Because their actual value is unknown, it is varied in calculation variants 020 to 035 to investigate their influence on cavern convergence and the development of the subsidence bowl.

	E [MPa]	ν [-]	ρ [kg/m^3]
Tertiary	34	0.33	2000
Triassic	5500	0.33	2400
Z2-Z4	15500	0.33	2400
Z1Salt	30000	0.30	2200
Z1Anhydrite	15500	0.33	2400
Carboniferous	20000	0.33	2400

Table 16: Assumed elastic material parameters for the geological units of the Haaksbergen field

The Fokker creep parameter values that resulted from the calibration of the creep tests on the Haaksbergen salt are listed in Table 17.

	A [s^{-1}]	N [-]	Q/R [K]
Z1 Salt	0.0012	3	6500

Table 17: Fokker creep parameters for the Haaksbergen salt

8.1.6. Evaluation criteria and subsidence prediction

The results of all calculation variants are evaluated on the convergence behaviour of the cavern and the development of the subsidence bowl. Therefore four result items are determined for each variant:

1. Rate of cross-sectional convergence during the lifetime of the cavern
2. Converged cross-sectional area that accumulates during the lifetime of the cavern
3. Cross-sectional subsidence bowl area development
4. Vertical subsidence in the deepest point of the subsidence bowl

Figure 55 and Figure 56 illustrate what is meant by 'converged cross-sectional area' and 'cross-sectional subsidence bowl area' respectively. In Figure 55 the sold blue line represents the simplified cavern contour at a certain point in time, say year x. This contour determines the cross-sectional area of the (half-)cavern in the model at that time. The dashed line represents the contour of the same cavern later in its lifetime, say year x+1. The light blue area is the area that the cavern has lost due to convergence, the converged cross-sectional area. The rate of cross-sectional convergence k is the annual loss of area divided by the initial cross-sectional area of the cavern. In formula form this is:

$$k = \frac{A(x) - A(x+1)}{A(x)} \tag{10.1}$$

In the first 10 years of the model, the cavern contour already changes yearly due to continuing development of the cavern. Therefore the above described method is not applicable during the period of cavern development when a time difference of one year is used. However when a time difference of 1 month is considered and multiplied by 12, the annual rate of cross-sectional convergence can be approached.

For each variant the convergence rate is determined for year 2, 5, 8 and 10 of the cavern lifetime by looking at a month of time-difference and for year 15, 25 and 35 by looking at a year of time difference.

The cross-sectional convergence area is determined by the sum of the yearly loss of area. Since this is not determined for every year, the years in between are assumed to have a converged cross-sectional area that is equal to that of the nearest year for which the value of converged cross-sectional area has been determined.

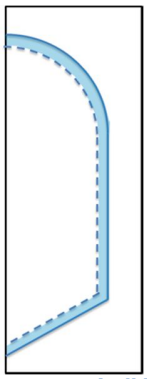

Figure 55: Converged cross-sectional area (blue) between year x (solid cavern contour) and year x+1 (dashed cavern contour)

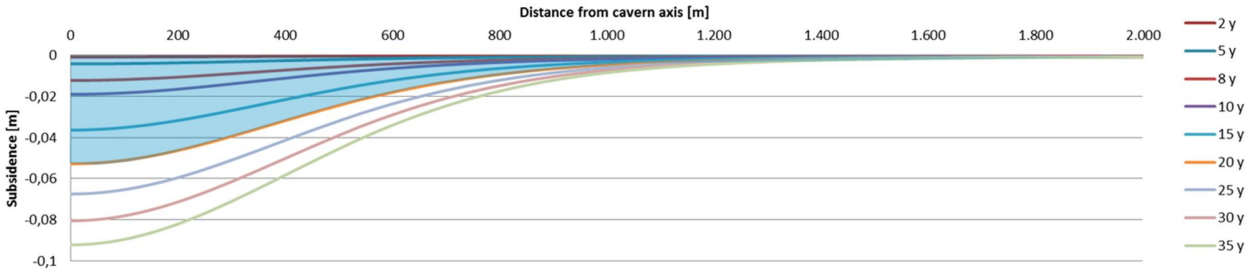

Figure 56: Subsidence bowl profiles with cross-sectional area of subsidence bowl in year 20 in blue

The cross-sectional area of the subsidence bowl is determined by looking at the displacement of the nodes at the top boundary of the model. In Figure 56 the development of the subsidence bowl for one of the variants is displayed. The subsidence bowl for the 20th year is represented by the orange curve. The blue area is the cross-sectional subsidence bowl area in year 20. For every calculation variant the cross-sectional area of the subsidence bowl is calculated for year 2, 5, 8, 10, 15, 20, 25, 30 and 35.

The vertical displacement in the deepest point of the subsidence bowl is extracted directly from the model. For every time step the vertical displacement of the node that lies at surface and exactly on the axis of the model, is registered.

8.2. Two cavern analysis

The model that was built for the two cavern analysis largely resembles the single cavern. In this section, there is only a description in the subsections when it differs from the single cavern analysis.

8.2.1. Scope and objectives

The objective of the two cavern analysis is to investigate the effect of cavern spacing, or pillar width on the convergence behaviour and subsidence above the caverns. To be able to compare the results with the single cavern analysis, it is desired that the model resembles the single cavern model as good as possible.

8.2.2. Model type

It is not possible to model two caverns in an axisymmetric model, because one of the caverns would become a ring-like tunnel when the model is rotated around the axis. Therefore it is chosen to do a plane strain analysis

8.2.3. Calculation variants

First a plane strain model with only one cavern is developed and run the same way as in the axisymmetric model. This way it becomes clear what the difference between convergence behaviour and subsidence is, when modelled with a plane strain and an axisymmetric model.

Because the goal is to investigate the effect of cavern spacing or pillar width, models with two caverns with different pillar widths are developed. In the current plan for the Haaksbergen brine field, the pillars will have a width of 175 m. In the analysis there will be two variants with a lower pillar width W_p and two variants with wider pillars as listed in Table 18. Images of the calculation variants are presented in Figure 57.

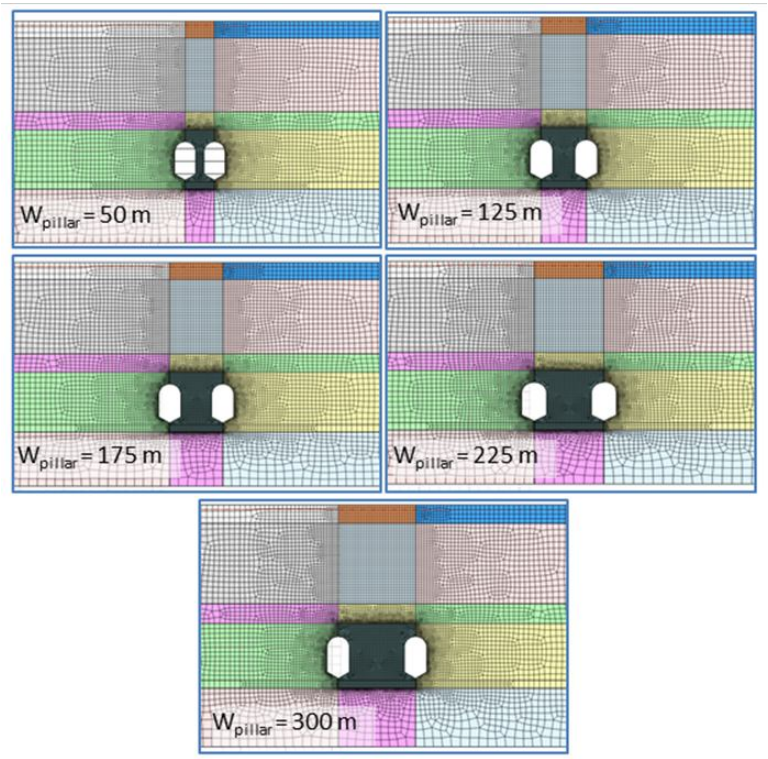

Figure 57: Images of the different two cavern models with different pillar widths

Calculation variant name	Pillar width [m]
053_S050	50
054_S125	125
055_S175	175
056_S225	225
057_S300	300

Table 18: Calculation variants of the two cavern models

8.2.4. Simplifications and assumptions

Dimensions and mesh

The dimensions of the plane strain model differ from the axisymmetric model. Two caverns are modelled here and both the left and right hand borders need to be at sufficient distance from the cavern. Because variants with different cavern spacing have to be made, the model was laid out for the variant with the largest cavern spacing as can be seen below. The width of the pillar and two adjacent caverns is 550 m in this variant (057). The entire model is 4500 m wide to have almost 2 km of space between the caverns and the boundaries of the model, see Figure 58.

In the vicinity of the cavern the meshed elements have a size of 5 x 5 m. Towards the edges the elements reach maximum dimensions of about 50 x 50 m, see Figure 58.

On second thought the model could also have been halved so that the axis would run exactly through the centre of the pillar. This would have limited calculation time and the amount of result data.

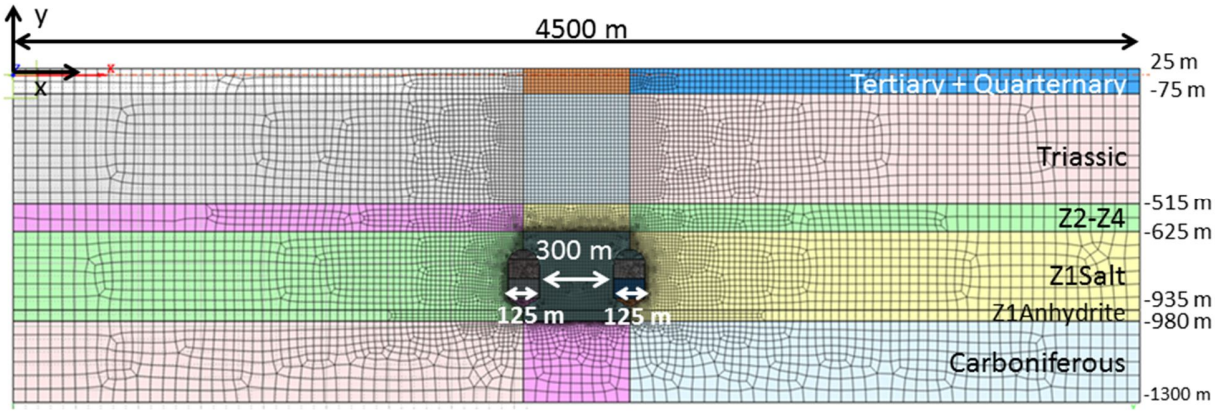

Figure 58: Dimensions and mesh of calculation variant 057 with two caverns

Boundary constraints

The boundary constraints of this model are similar to those of the single cavern model. The nodes on the left and right hand boundary are fixed in the horizontal direction. Nodes at the bottom boundary of the model can not move vertically, see Figure 59. If on basis of symmetry only half the pillar and one cavern would have been modelled, the nodes on the axis of symmetry would have been fixed horizontally.

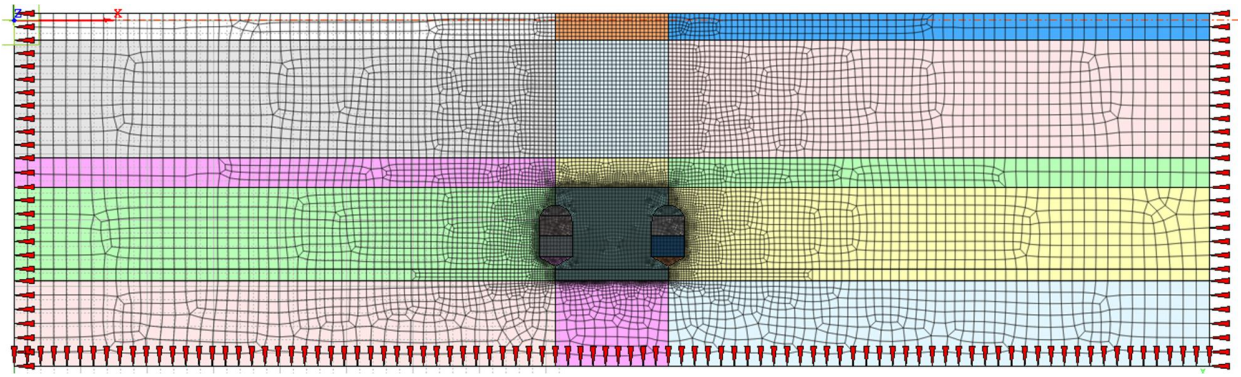

Figure 59: Boundary constraints applied to a two cavern plane strain model

Geology

All aspects of geology in this model are equivalent to the axisymmetric single cavern model. A description can be found in subsection 8.1.4.

Cavern Development

In the plane strain model with only one cavern, the cavern is developed in 10 phases in order to carry out the calculations exactly the same way as done in the axisymmetric analysis. To simplify the process of building the model, generating the mesh and controlling the model (telling it which elements are active in which phase, how many time steps to take, etc.) it was decided to divide each cavern into 4 units. Cavern development still takes ten years. During these ten years, time steps of 1 month are taken. After completion of the cavern development the model continues to take time steps of 1 year, until the year 2050 is reached. As described in subsection 8.1.4 the groups of elements that become inactive are 'replaced' by a brine pressure that depends on the depth. In Figure 60 the time schedule of the

development of the caverns is presented, including an image of the caverns at their full dimensions with brine pressure acting on the walls (phase 5).

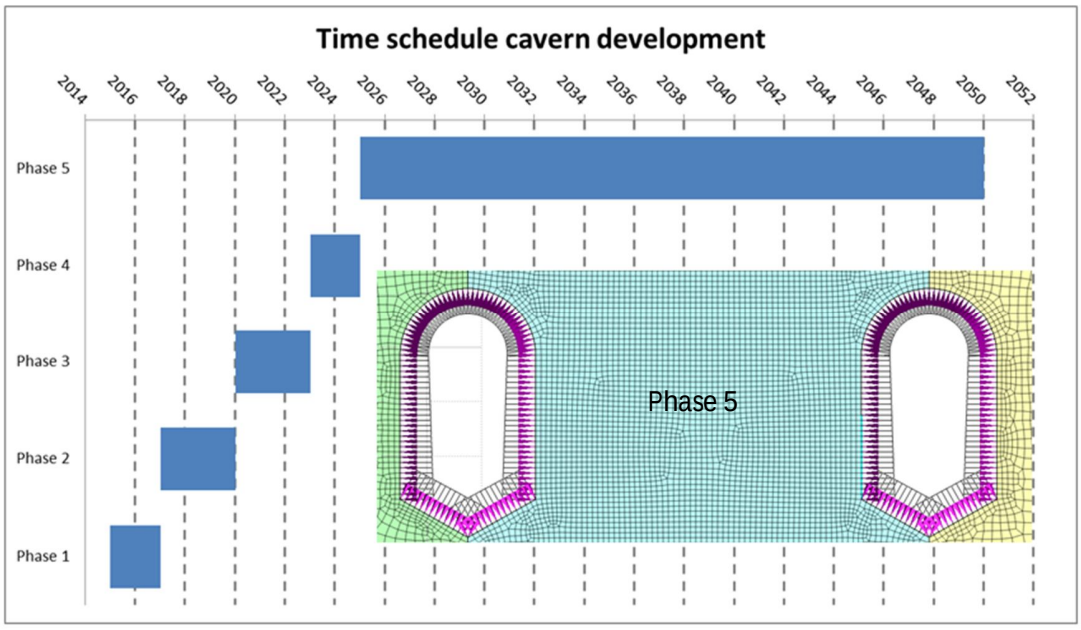

Figure 60: Time schedule of cavern development in a two cavern plane strain model including an image of the brine pressure acting on the cavern walls in phase 5

Temperature

Temperature implementation is done exactly the same way as described in subsection 8.1.4.

8.2.5. Material behaviour and parameters

All material models and material parameters are the same as described in subsection 8.1.5.

8.2.6. Evaluation criteria and subsidence prediction

The cavern convergence and subsidence bowl area are determined similarly to the approach described in subsection 8.1.6. The only difference is that here the cross-sectional area of complete caverns and subsidence bowls is determined, where this was only half in the axisymmetric model.

8.3. Calibration of creep properties

IfG (2012b) determined the parameter values for the Minkley model based on laboratory tests. The Fokker creep model that is implemented in DIANA requires other parameters. Therefore the results of the creep test must be used to determine the Fokker creep parameters of the Haaksbergen salt. In this section it is described how this was done.

10.3.1. Creep rates Haaksbergen salt

The creep rates that were measured during creep tests are listed in Table 19.

specimen	load step	load (MPa)			rate (1/d)
		σ_1	σ_3	$\Delta\sigma$	
461/8/52/K2	1	38	20	18	2,32E-04
	2	40	20	20	2,71E-04
461/8/52/K4	1	38	20	18	1,67E-04
	2	40	20	20	1,98E-04
461/10/66/K6	1	36	20	16	1,18E-04
	2	38	20	18	1,96E-04
461/11/70/K8	1	36	20	16	1,68E-04
	2	38	20	18	2,16E-04
461/16/109/K10	1	34	20	14	9,63E-05
	2	36	20	16	1,32E-04
461/16/109/K12	1	34	20	14	8,62E-05
	2	36	20	16	1,10E-04
461/18/118/K14	1	32	20	12	5,20E-05
	2	34	20	14	8,26E-05
461/21/144/K18	1	32	20	12	4,16E-05
	2	34	20	14	6,42E-05
461/23/158/K20	1	30	20	10	3,44E-05
	2	32	20	12	4,43E-05
461/26/178/K22	1	30	20	10	3,18E-05
	2	32	20	12	3,13E-05
461/29/197/K26	1	28	20	8	1,65E-05
	2	30	20	10	1,98E-05
461/29/197/K28	1	28	20	8	1,99E-05
	2	30	20	10	2,41E-05
461/32/217/K30	1	28	20	8	1,99E-05
	2	30	20	10	2,69E-05
461/38/262/K34	1	28	20	8	2,13E-05
	2	30	20	10	2,15E-05
461/41/280/K37	1	26	20	6	1,08E-05
	2	28	20	8	7,62E-06
461/43/296/K40	1	26	20	6	1,38E-05
	2	28	20	8	8,50E-06

Table 19: Measured creep rates of the Haaksbergen salt, (IfG, 2012b)

For every test the radial stress on the sample was 20 MPa and the axial stress at which each test was carried out was determined in advance. A relationship needs to be established between the difference in axial and radial stress ($\Delta\sigma$ or in creep laws sometimes called σ_{eff}) and the creep rate. The Fokker creep law for secondary creep states that this relation is a power law. The process to extract Fokker creep parameters from the Haaksbergen salt test results can be explained using Figure 11 on page 16. This figure is used in Chapter 3 to illustrate secondary creep in the BGRa creep law. Since Fokker's law for secondary creep is the same, it can also be used in this context.

The red squares in the diagram represent creep rates that result from creep tests at predetermined values of $\Delta\sigma$ or σ_{eff}. The blue curve is the best fit with these results. When the equation of this fitting curve is written in the form of a power law, the parameters of the creep law can be derived from this.

Following this procedure the first step would be to plot the creep rates against the differential stress. However, advice from TNO DIANA was to have the unit for time in seconds. The unit of the provided

creep rates is [day^{-1}], therefore they need to be divided by the amount of seconds in a day (86400). The next step is to draw a power law trend line and display the associated equation. This can be seen in Figure 61 below.

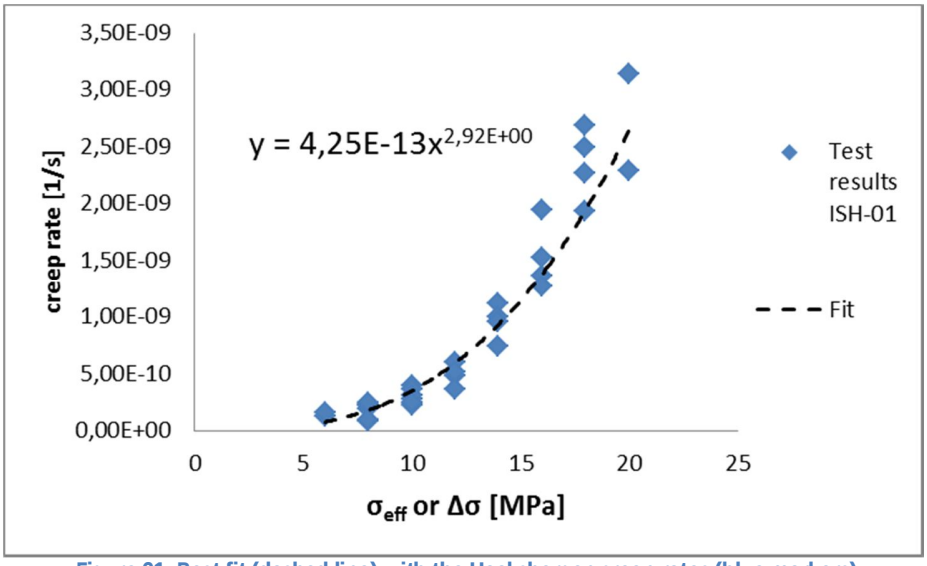

Figure 61: Best fit (dashed line) with the Haaksbergen creep rates (blue markers)

The following equation (Eq. 8.2) is solved to obtain creep parameters

$$\dot{\varepsilon}_{cr} = A \cdot e^{-\frac{Q}{RT}} \cdot \left(\frac{\sigma_{eff}}{\sigma^*}\right)^n = 4.25 \cdot 10^{-13} x^{2.92} \qquad \text{(Eq. 8.2)}$$

For the temperature *T* the value 298 K (25 °C) is filled in, because the creep tests were carried out at this temperature. In DIANA *Q* and *R* are not inserted separately. *R* is the universal gas constant (8.31·10^{-3} [kJ/K·mol]), and *Q* is a material constant for salt (54 [kJ/mol]) (Jeremic, 1994). The value of *Q*/*R* needs to be provided in DIANA and this is about 6500 [K^{-1}].

In (Eq. 8.2) and Figure 61 it can be recognized that the value of the exponent *n* should be 2.92. In the application of creep laws usually integers are used for stress exponents. Therefore in the standard set of creep parameters *n* is set at 3.

The factor 4.25·10^{-13} needs to match $A \cdot e^{-\frac{Q}{RT}}$. As described above, the values for *Q*, *R* and *T* are already known, this gives $e^{-\frac{Q}{RT}} = 3.37 \cdot 10^{-10}$. This leaves for *A* a value of 0.0012 [s^{-1}].

In summary, it can be stated that the set *A* = 0.0012 [s^{-1}], *Q*/*R* = 6500 [K^{-1}] and *n* = 3 [-] is the standard set of Fokker creep parameters for the Haaksbergen salt.

10.3.2. Single element analysis in DIANA

To be able to check whether implementation of these values in DIANA gives the expected results, a creep tests was simulated in DIANA with an axisymmetric single element analysis. This element has half the width of the core samples that were used in the actual tests and the height is equal to that of the real samples. The material properties of the salt are assigned to the element, axial and radial loads are

applied and boundary constraints are set. An illustration can be found in Figure 62. After the load is applied, forty time steps of one day are taken.

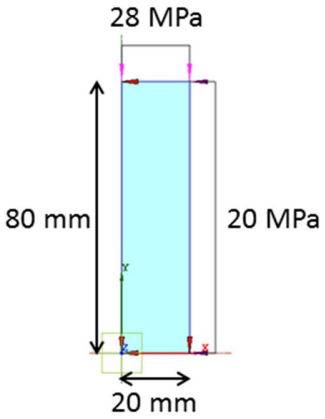

Figure 62: Single element creep test simulation in DIANA

Before the simulation is done, the creep rate that has to be expected from the model can be calculated. Filling in the standard set of parameter values and (28 – 20) 8 MPa for the differential stress, a creep rate of $2.07 \cdot 10^{-10}$ [s^{-1}] can be expected.

In Figure 63 the creep deformation, which is in this case given by the vertical strain ε_{yy}, is plotted for the forty days of the test period. From the equation of the trend line that is included in the diagram, it can be seen that the gradient of this line (in other words, the creep rate) is $2.09 \cdot 10^{-10}$ [s^{-1}] Which is very close to the predicted $2.07 \cdot 10^{-10}$ [s^{-1}].

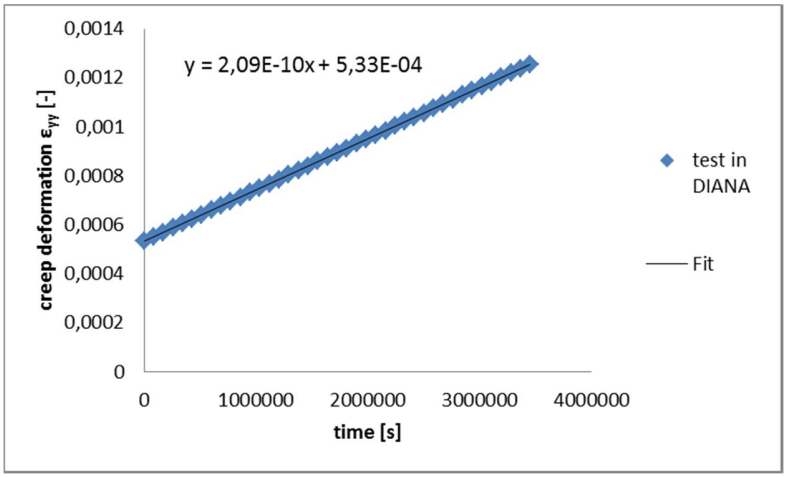

Figure 63: Creep deformation resulting from the single element creep test simulation in DIANA

9. Results and discussion

In this chapter the results of the different models are presented and discussed. Section 9.1 deals with some initial variations on the base case model to test the response. For example a model with a finer mesh was developed to check whether this would give a significant difference in the results. Also models were run to investigate the results on the very long term, different numbers of phases in cavern development, with and without depth-dependent temperature etc. This is all in order to gain confidence in the response of the model.

In section 9.2 the results of the sensitivity analysis with the axisymmetric single cavern model are presented. The results of the plane strain analysis can be found in the subsequent section 9.3.

9.1. Tests on base case

To investigate the response of the model before starting the sensitivity analysis, some tests were done gain confidence in the response of the model. This section is dedicated to these tests.

9.1.1. Base case

First of all the base case was run and its results were analyzed. As explained in subsection 8.2.6, the four evaluation criteria are rate of cross-sectional convergence, development of converged cross-sectional area, development of cross-sectional subsidence bowl area and vertical displacement of the surface exactly above the centre of the cavern. The results are presented in the graphs a to d in Figure 64.

In diagram a, where the rate of cross-sectional convergence is plotted, it can be seen that this rate is much higher in the beginning of cavern development, than later on. During the cavern development (first ten years) the rate decreases gradually. From year ten to thirty-five when the cavern is at its full dimensions, this keeps on decreasing. Since it does not reach the value of zero, cavern convergence continues. This is confirmed by the development of the converged cross-sectional area. As can be seen in diagram b, this area keeps on increasing and does not tend to a constant. In graph c it can be seen that this also applies to the cross-sectional area of the subsidence bowl as well as the vertical displacement at surface (d). The development of the cross section profile of the subsidence bowl over the years is presented in the bottom image (e) of Figure 64.

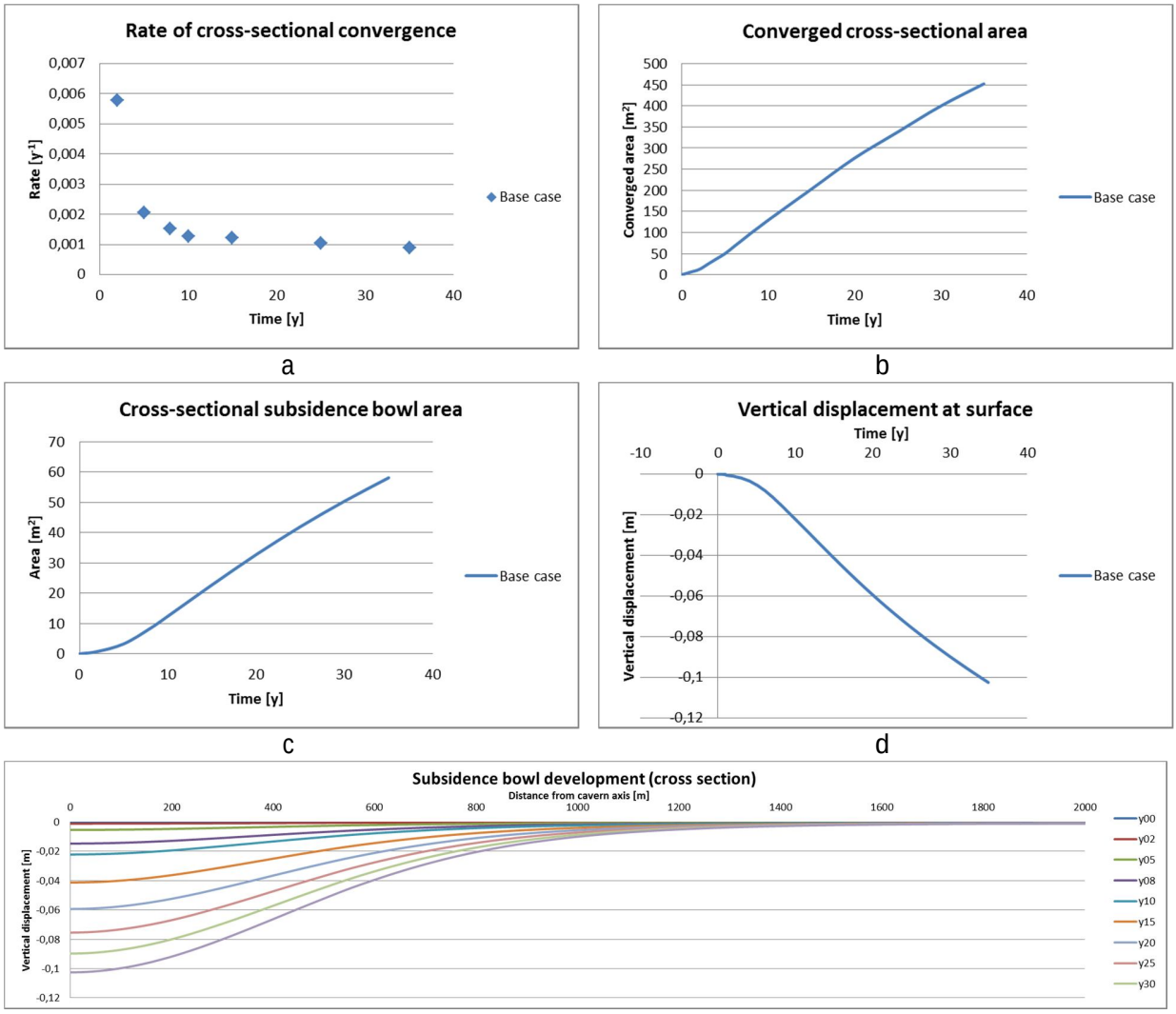

Figure 64: Results of the base case variant

The fact that the rate of cross-sectional convergence starts with a relatively high value, is related to the geometry of the cavern in the early stages of development. Cavern convergence occurs at the contour of the cavern. In the early stages, the contour, or perimeter is relatively large with respect to the cavern area. This is supported by the graph in Figure 65 where in red squares the ratio of cavern perimeter over cavern cross-sectional area is plotted. The trend is similar to the trend in the rate of convergence. So where the ratio of cavern perimeter over cavern cross-sectional area is high, the rate of cross-sectional convergence is high as well.

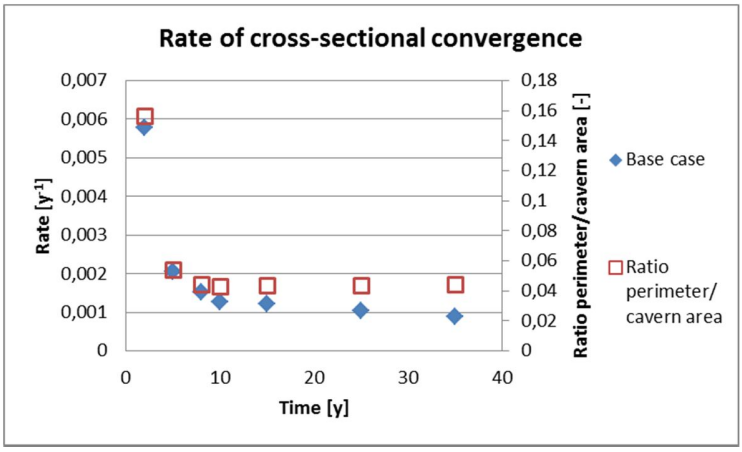

Figure 65: Rate of cross-sectional convergence and ratio of cavern perimeter over cross-sectional area in the course of the model

Comparing the magnitude of the converged cross-sectional area and the cross-sectional area of the subsidence bowl, it can be seen that these are not equal. This suggests that not all converged area is translated to surface. However, here the fact that the model is rotated around the axis comes in. When the model is rotated around its axis, volumes can be calculated instead of areas. In axisymmetric models, the distance from the axis is a major factor in volume calculation. This is illustrated with the following calculation example (see Figure 66).

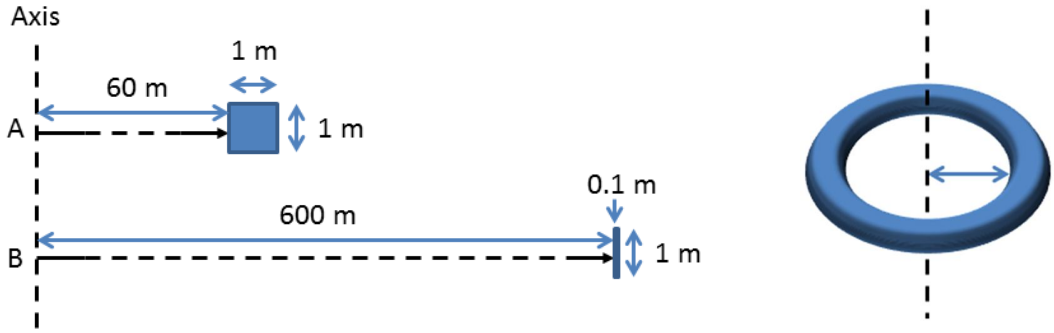

Figure 66: Calculation example of volume calculation by rotation around an axis

Considering first the upper part (A) of the left side of Figure 66, the blue square can be seen as a an area of 1 x 1 m at a distance of 60 m from the axis. When this square is rotated around the axis, a ring-like volume (like sketched in the right hand side of Figure 66) will be formed that is 1 m high and 1 m wide. The inner radius of this ring r_i is 60 m and the outer radius r_o is 61 m. To calculate the volume of the ring, it can be seen as the volume difference between two concentric cylinders. The formula to calculate the volume of a cylinder V_{cyl} with height h and radius r is (Eq. 9.1)

$$V_{cyl} = h\pi r^2 \qquad \text{(Eq. 9.1)}$$

The volume of the ring is the volume of the outer cylinder with radius r_o minus the volume of the inner cylinder with radius r_i, see (Eq. 9.2)

$$V_{ring,A} = V_{cyl,o} - V_{cyl,i} = h\pi r_o^2 - h\pi r_i^2 = h\pi\left(r_o^2 - r_i^2\right) = 1 \cdot \pi(61^2 - 60^2) = 121\pi \text{ m}^3 \qquad \text{(Eq. 9.2)}$$

In the lower part of the left side of Figure 66 (B), Also an area is drawn. The height remained 1 m, but this time, the width was 0.1 m and it is situated at a distance of 600 m from the axis. The volume of a now very thin ring is calculated with (Eq. 9.3)

$$V_{ring,B} = V_{cyl,o} - V_{cyl,i} = h\pi r_o^2 - h\pi r_i^2 = h\pi\left(r_o^2 - r_i^2\right) = 1 \cdot \pi(600.1^2 - 600^2) \cong 120\pi \text{ m}^3 \qquad \text{(Eq. 9.3)}$$

From this example it can be learned that two areas that differ largely (A_A = 1 m^2 and A_B = 0.1 m^2) on a 2D plane of an axisymmetric model can have (nearly) the same volume when rotated around an axis, depending on the distance to that axis. This has to be kept in mind when the converged cross-sectional area is compared to the cross-sectional area of the subsidence bowl. The converged volume is located at a limited distance to the axis, whereas the subsidence bowl stretches hundreds of meters along the top boundary of the model.

In the calculation example a simple geometry was used. In the axisymmetric model, the cavern contour as well as the subsidence bowl are irregularly shaped. Therefore it is only possible to obtain the exact volumes using 3D software that can rotate the cavern contour and subsidence bowl profile around an axis, convert this into a 3D body and calculate the enclosed volume. Unfortunately, regarding the amount of modelling results and the time aspect, this could not be done for all calculation variants in this work. To give an indication, the volumes that are enclosed by the cavern contours and subsidence profiles at the end of the years 10 and 35 are studied, see Table 20. These times were chosen because the cavern is complete at both times and in the period in between, the convergence and subsidence bowl development are only caused by the creep-induced convergence of the cavern, not by the initiation of a new phase.

	Cavern volume [m³]	**Subsidence bowl volume [m³]**
Year 10	2206266	34208
Year 35	2099204	140708
Difference [m³]	107062	106500

Table 20: Volumes of cavern and subsidence bowl in year 10 and 35

When both volume differences are compared, it can be seen that almost all (99.47%) of the volume loss of the cavern from year 10 to year 35 (107062 m^3), contributes to the increase of the subsidence bowl volume in this period (106500 m^3). Below, in Figure 67 the cross-sectional areas of the cavern are presented. In blue for year 10 and in red for year 35. As can be seen, the cavern has lost most of its cross-sectional area at the wall of the cylindrical part of the cavern. Since this part is situated at the largest distance from the axis of the model, this makes up the biggest part of the convergence volume. The 3D volume calculations were conducted in Surpac 6.3, which is a software package used for mine design.

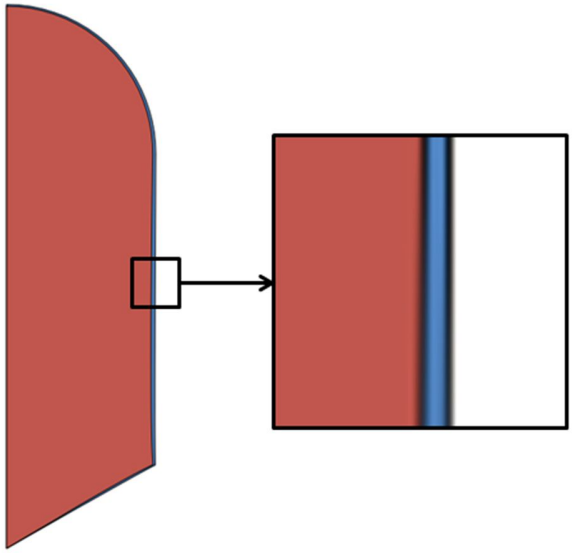

Figure 67: Cross-sectional cavern area in year 10 (blue) overlapped by year 35 (red)

9.1.2. Mesh size

In order to investigate the influence of the mesh size on the results (or in other words: to check whether the chosen mesh is sufficiently fine) a model was developed with a maximum element size of 1 x 1 m near the cavern instead of 5 x 5 m. This resulted in a model that contained a much higher number of elements (5217 elements in the standard model and 18435 elements with a finer mesh), that took significantly more time to run the calculations. Besides the mesh size, nothing was changed in the model.

To be able to compare the results of this model with the original one, the cross-sectional cavern areas of both models were compared at different points in time. The results can be found in Table 21.

	Cross-sectional area cavern standard mesh size[m²]	Cross-sectional area cavern finer mesh size [m²]	Difference [%]
Year 10	12164.2787	12213.0351	+0.4
Year 25	11955.0314	12084.1869	+1.08
Year 35	11842.0534	12015.2008	+1.46

Table 21: Cross-section cavern areas for year 10, 25 and 35 for standard mesh size and a finer mesh

At every point in time, the model with the finer mesh size results in a cavern that has converged less. From this it can be concluded that with the standard mesh size the deformations are overestimated. The difference in percentages with respect to the entire cavern area are very small. It has to be noted here that during the 'lifetime' of the model, there is an increase in difference, but it remains small. The small differences indicate that a 5x5 m mesh is acceptable.

9.1.3. Phased cavern development

In the standard model the cavern is developed in 10 phases of 1 year each. In for example the geomechanical models of the SCC caverns in the Hengelo brine field the complete cavern appears in the model instantaneously at time $t = 0$. To investigate whether dividing the caverns into a number of phases has a large influence on the results, the model was also run with 3 phases. In the first phase of two years,

the sump was removed. In the second phase of five years the complete cylindrical part was removed and in the third phase the spherical roof in 3 years. Afterwards the model keeps on running for 25 years, like in the base case.

The vertical displacement along the axis of the model is the output that is easiest to retrieve. For this reason the vertical displacement of the nodes at surface, in the roof of the spherical part, in the roof of the cylindrical part and in the roof of the sump part is compared for the standard model with 10 phases and the alternative with 3 phases. In Figure 68, the dots indicate the locations of the selected nodes. The colours match the colours of the curves in the diagram of Figure 69.

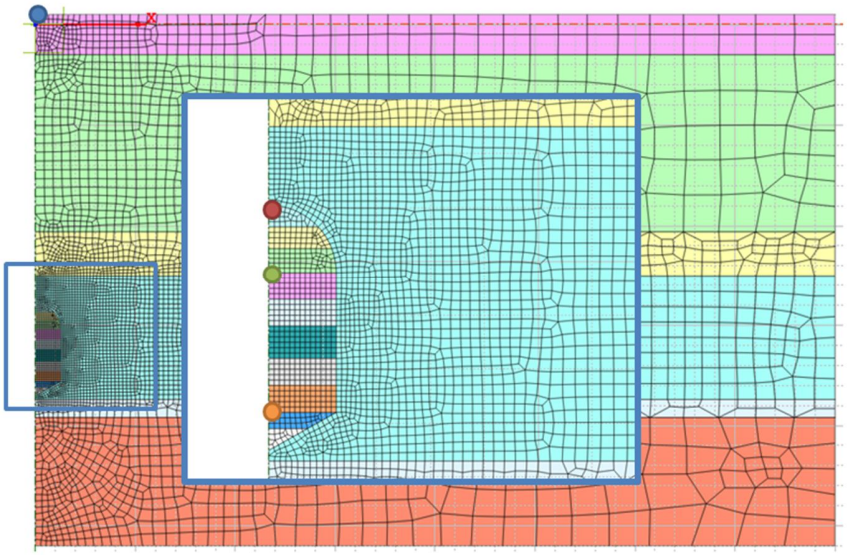

Figure 68: Location of nodes where vertical displacement was recorded

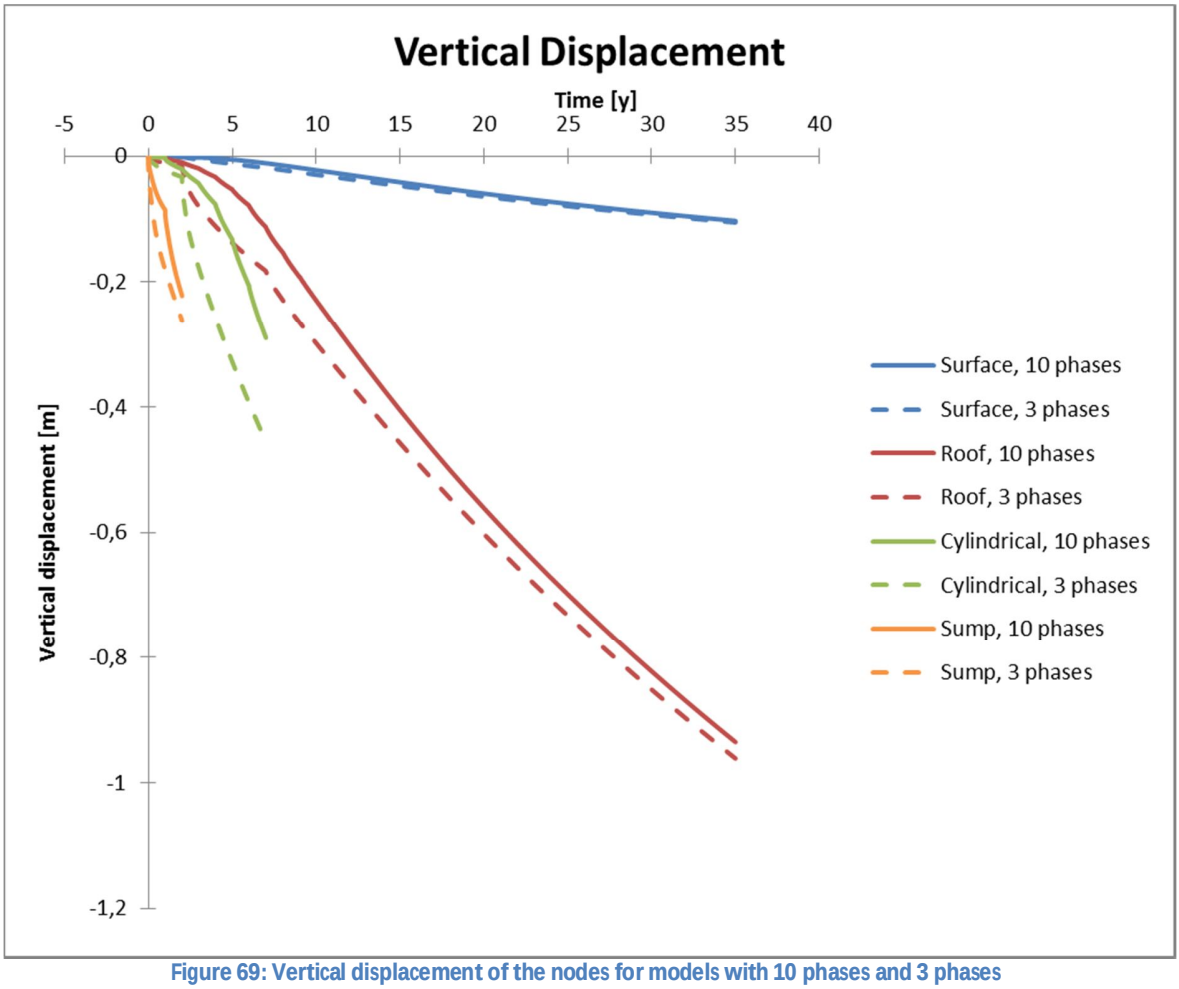

Figure 69: Vertical displacement of the nodes for models with 10 phases and 3 phases

The orange and green curves that represent the nodes in the roof of the sump phase and the cylindrical part end after 2 and 7 years respectively, because the nodes are no longer active after these years. Studying the differences between the solid and dashed lines, it can be seen that after a new phase is initiated, the vertical displacement is much higher for the 3-phase model than for the 10-phase model. This means that having less phases in the model results in a higher (overestimated) vertical displacement and therefore the results can be considered to be more conservative. The red curves for the node in the roof of the cavern deviate significantly in the early stage of the model, but on the long term they become much closer. For the node at surface there is only a very small difference between the 3 and 10-phased model, because the displacements are much smaller here.

After investigation of the effect of the number of phases in cavern development, it was decided to keep the concept of cavern development in 10 phases for the axisymmetric single cavern analysis. The main reason for this is that there is a significant difference in the results during cavern development. Besides this, the model was initially designed to develop the cavern in 10 phases. All this work had already been done and it would be a shame not to use it, when it gives more realistic results.

9.1.4. Long term response

In Figure 64 it could be seen that the rate of cross-sectional convergence does not decrease to zero. As a consequence the converged cross-sectional area continues to increase and so does the cross-sectional area of the subsidence bowl. This raises the question what would happen on the very long term. Therefore the model was run on a very long term, namely 1000 years. This means that after the 10 years of cavern development the model keeps running for 990 years. The results are shown in Figure 70.

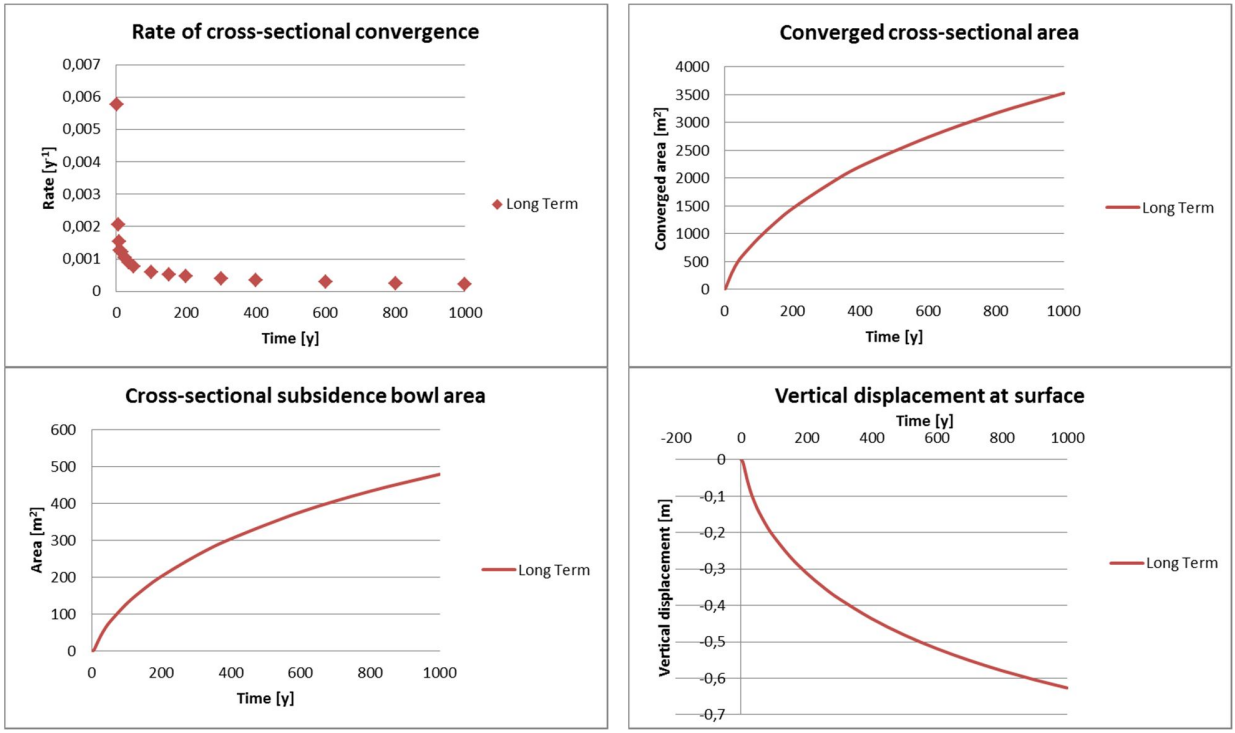

Figure 70: Results of base case when run for 1000 years

As shown in the upper left graph, the rate of cross-sectional convergence keeps on decreasing, but it does not reach zero. Therefore the converged cross-sectional area and the cross-sectional area of the subsidence bowl keep on increasing. This is also valid for the vertical displacement at surface. However, the trends look different on this timescale when comparing Figure 64 and Figure 70.

The cavern keeps on converging because the pressure of the brine on the cavern wall is constant in time. Because this pressure is less than the stress in the rock salt that surrounds the cavern, there is always a net stress cavern inwards from the rock salt. In the current plan for the Haaksbergen field it is described that the caverns will be sealed after operation. When the cavern keeps on converging, pressure in the brine inside the cavern will increase. This gives a counter-pressure on the cavern walls to limit the convergence. The fact that this process is not taken into account in the model puts a significant limitation on the applicability of the modelling results. The next subsection is dedicated to a model variant that incorporates sealing of the cavern, to provide an insight on how it influences the results.

9.1.5. Cavern sealing after operation

In this subsection it is described how cavern sealing after operation can be implemented into the model and it is shown how it influences the results. It is assumed that the pressure of the brine inside a cavern increases to the lithostatic pressure after a cavern is sealed. Before or as lithostatic pressure is reached, brine will permeate into the surrounding rock salt.

In this model the cavern is still developed in 10 years. For 5 years after operation, the cavern remains open and the brine pressure that acts on the walls remains active. In year 15 this is replaced by a pressure that is equal to 70% of the lithostatic pressure at every depth value in the cavern. In year 20 this is increased to 80%. Afterwards the model runs 25 extra time steps of 1 year. The applied values for depth-dependent lithostatic pressure are retrieved from the results of the very first '0' phase of the model where the stress that every element in the model experiences from the weight of the overlying material is calculated. Values are determined at the interface Z2Z4 – Z1Salt (-625 m) and Z1Salt – Z1Anhydrite (-935 m). And a linear interpolation is applied in between because the material is uniform in this interval (Z1Salt). See Figure 71 for the implementation of the pressure function 'lithostatic'.

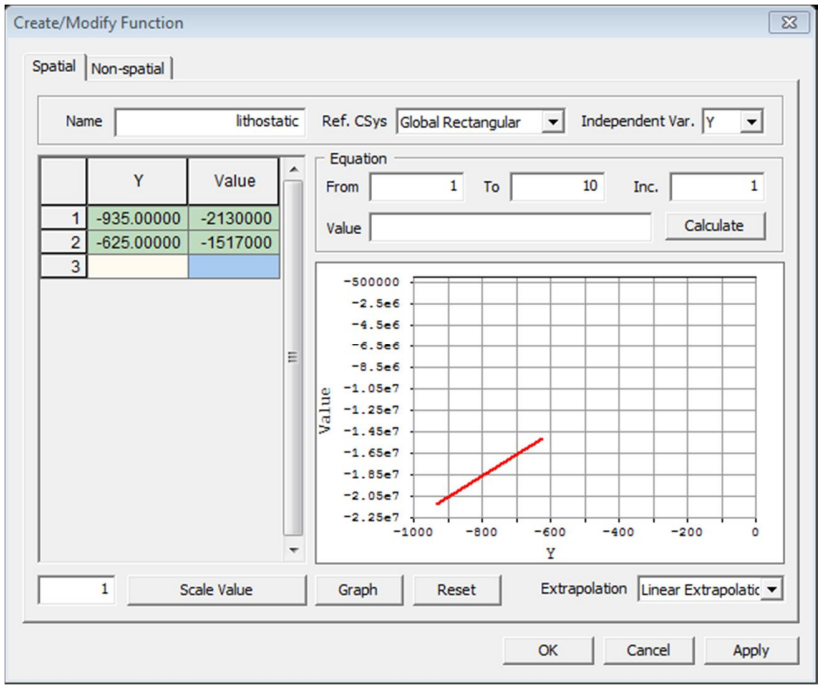

Figure 71: Implementation of the 'lithostatic' function

In Figure 72 the results are presented, to be able to make a comparison, the base case results are plotted as well. On the secondary vertical axis of the upper left graph, the development of internal pressure at a depth of 800 m in the course of the model is plotted to be able to see how the internal pressure is imposed in time.

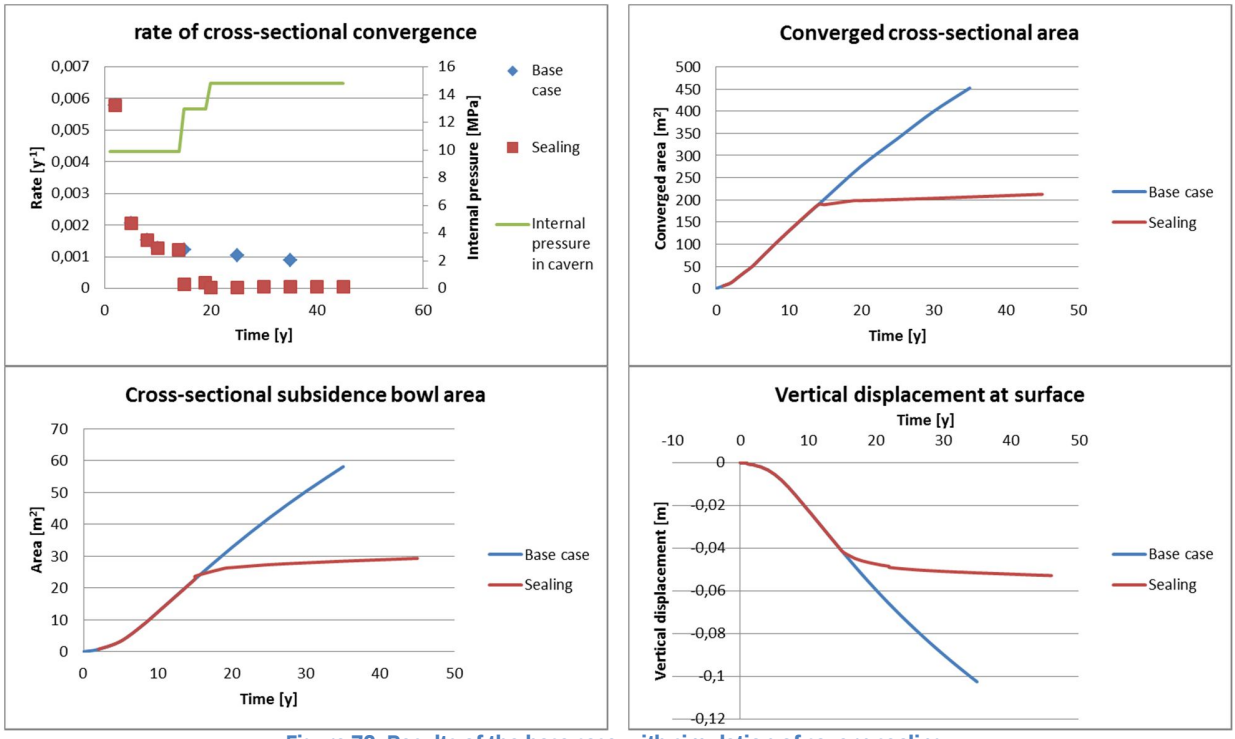

Figure 72: Results of the base case with simulation of cavern sealing

Clearly, the application of cavern sealing limits the convergence and the development of the subsidence bowl and vertical subsidence to a significant extent. This strongly supports that it is useful, maybe even necessary, to seal caverns after operation. Although the convergence rate is limited when (part of) the lithostatic pressure is applied, it is still not zero. Still the conclusion remains that sealing a cavern puts a significant limitation on cavern convergence and subsidence at surface.

9.1.6. Depth dependency

In order to establish that increasing depth (higher stress and temperature) results in increasing cavern convergence, two models as shown in Figure 73 were developed. The models both contain a small cavern that is developed in 3 phases because of its small cross-sectional area. In the left hand model the cavern is placed very high in the layer of salt. In the right hand model the cavern is situated very low in the layer of the salt. Since both stress and temperature increase with depth and both of these factors have a stimulating effect on creep, it is expected that the lower cavern experiences more convergence than the upper cavern.

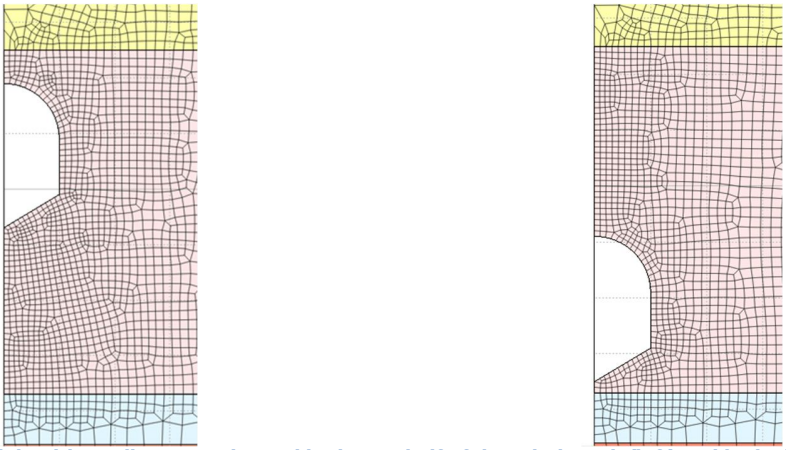

Figure 73: Two models with small caverns situated in the top half of the salt deposit (left) and in the bottom half (right)

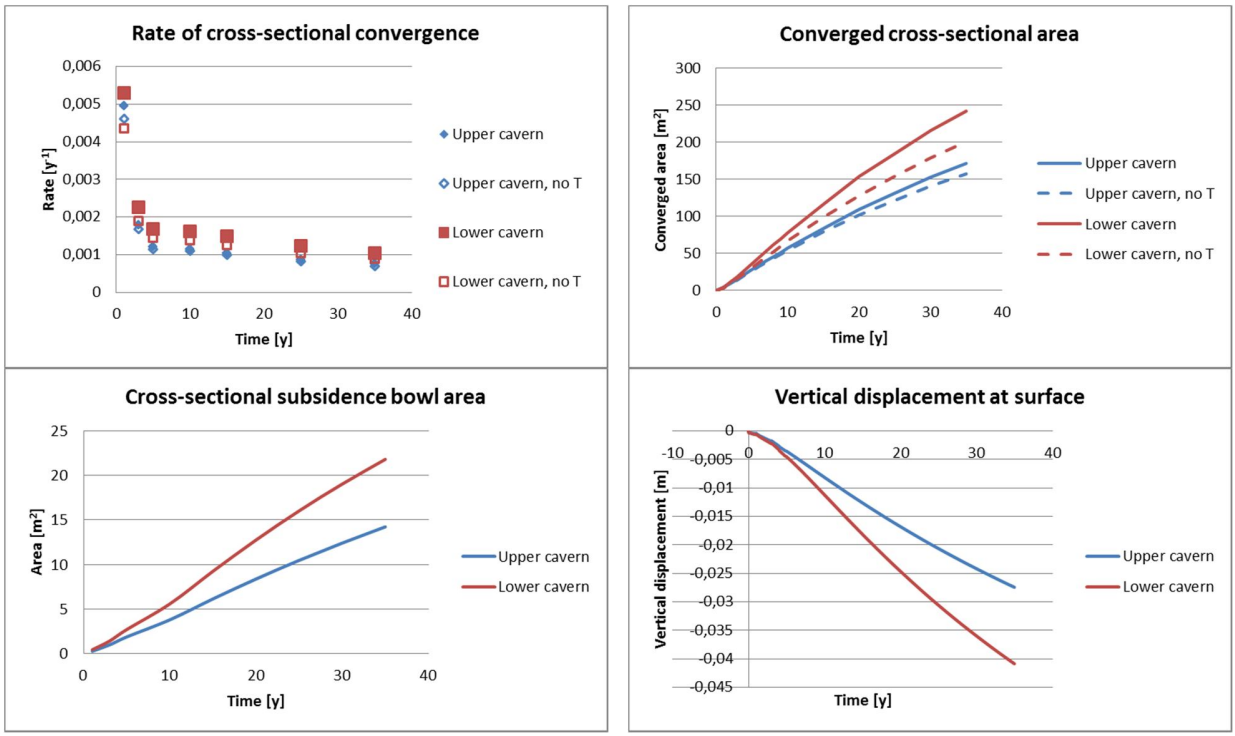

Figure 74: Results of the analysis with two small caverns

The expected higher convergence for the lower cavern is confirmed by the results, see the upper graphs of Figure 74. As a consequence of more convergence, the subsidence bowl and vertical subsidence for the lower cavern are also increased with respect to the higher cavern, see lower diagrams.

In the two upper graphs also open markers and dashed lines are added. These represent the results of the same models when depth-dependent temperature was disabled and a default temperature of 25 °C was used throughout the model. In the upper right figure it can be seen that the depth-dependent temperature does not influence the results severely for the upper cavern (blue lines). An indicative temperature at the depth interval of this cavern is 30 °C, where this is 35 °C for the depth interval of the lower cavern. The deviation from the default temperature is larger for the lower cavern, therefore the

difference in the results is bigger for the lower cavern (red lines). The difference between the dashed lines of the upper left graph shows the influence of the depth-dependent stress. The difference between the dashed line and the associated solid line shows the influence of depth-dependent temperature.

9.2. Single cavern analysis

Now that the response of the model on different aspects has been tested, confidence is gained in the quality of the model. In the single cavern analysis the variants as listed in Table 15 are run. The results are presented in three categories. The cavern diameter and thickness of salt roof and floor are grouped in the category 'Cavern dimensions' in subsection 9.2.1. The creep parameters and elasticity modulus of salt fall into the category 'Salt properties' and the results are presented in subsection 9.2.2. The last category is named 'Elasticity moduli'and subsection 9.2.3 contains the results of the different values of the elasticity modulus for salt and the overburden units.

9.2.1. Cavern dimensions

By changing the cavern diameter, thickness of the salt roof or thickness of the salt floor, always at least two aspects of the model are changed simultaneously. For example when the cavern diameter is changed, also the cavern cross-sectional area changes. If it is desired to keep the cavern cross-sectional area constant, enlarging the cavern diameter immediately leads to limiting the height of the cavern and vice versa. Similar things happen when the thickness of the salt roof or salt floor is changed. Therefore it was decided to let the cavern cross-sectional area 'grow' with the changing dimensions. When looking at the results that are presented under the following headings, it needs to be kept in mind that with increasing cavern diameter or decreasing thickness of salt roof or floor, the cross-sectional area of the cavern increases. After these results are presented they will be related to the cross-sectional area of the model from which the results originate.

Cavern diameter

Figure 75 shows the results of the variants with different cavern diameters. In the base case the diameter is 125 m.

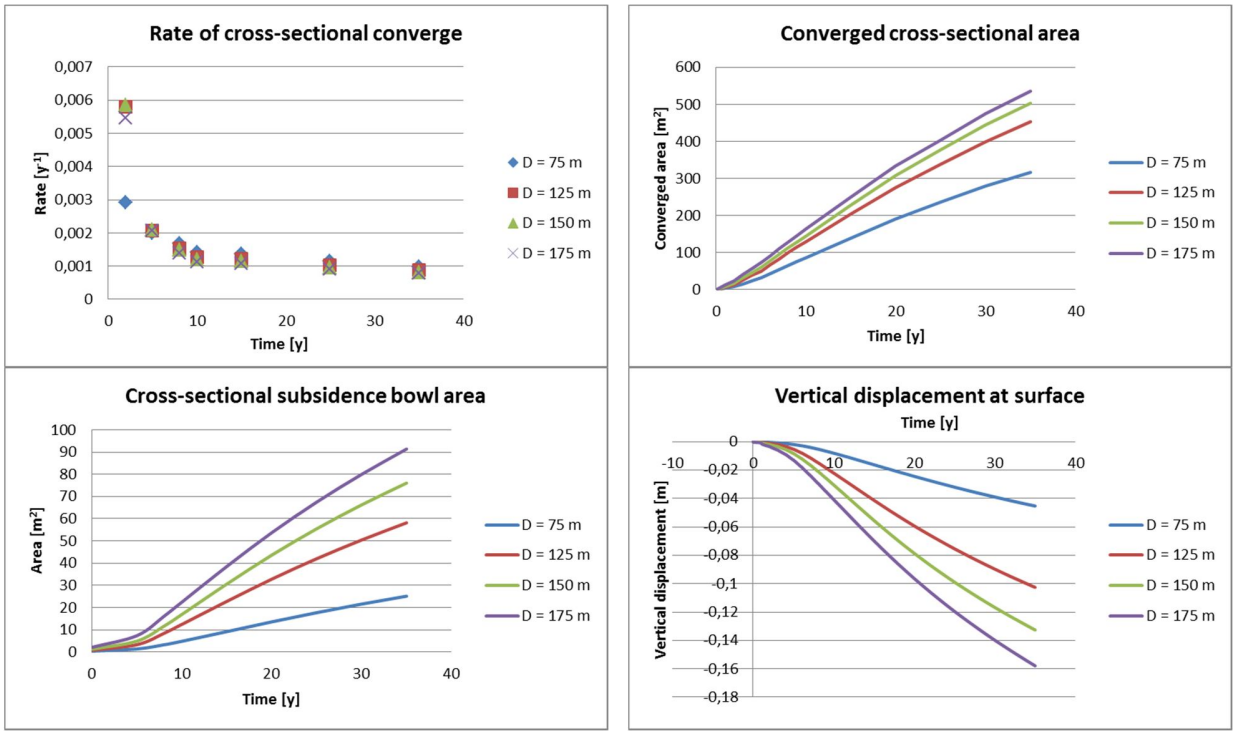

Figure 75: Results of the cavern diameter variants

In the upper left graph it can be seen that on the long term the rates of cross-sectional convergence are very similar. Nevertheless, on the long term the convergence rate for the smallest cavern (D = 75 m) is higher than for the biggest cavern (D = 175 m). This is unexpected because the biggest caverns lead to the largest convergence and subsidence, as can be seen in the other graphs. To find an explanation for this, the geometry of the caverns is considered. In Figure 76 an image of the smallest cavern (left) and the biggest cavern (right) can be seen.

Figure 76: Images of calculation variants with different cavern diameters, D = 75 m (left) and D = 175 m (right)

Where the smallest cavern has a thin and tall geometry, the cross-section of the biggest cavern approaches more a semicircle-like geometry. For the small cavern the perimeter is large with respect to the area it encloses compared to the big cavern. Since convergence can only happen at the cavern contour, this results in the high rate of cross-sectional convergence. This also explains why in an early stage of the model, the rate of cross-sectional convergence is low for the small cavern and high for the big cavern. In an early stage, the cavern with the large diameter is much wider than it is high, resulting in a less favourable (higher) ratio of perimeter over cross-sectional area than for the cavern with the small diameter.

Thickness salt roof

The results of the salt roof thickness variants are presented in Figure 77, a thinner salt roof leads to a cavern with a larger cross-sectional area. In the base case the thickness of the salt roof is 72.5 m.

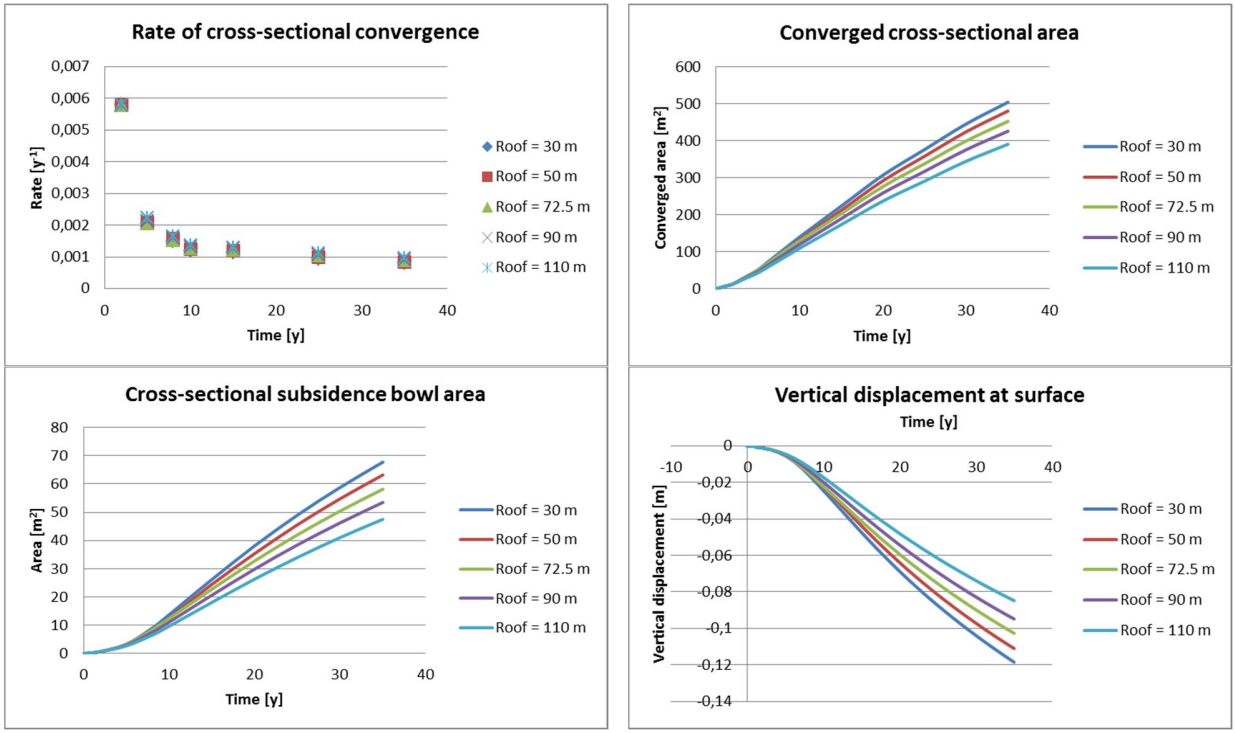

Figure 77: Results of the variants with different salt roof thickness

Thickness salt floor

In Figure 78 the results of the variants with different salt floor thickness are presented. Also here, a thin salt floor leads to a larger cross-sectional area of the cavern. The base case has a 10 m thick salt floor.

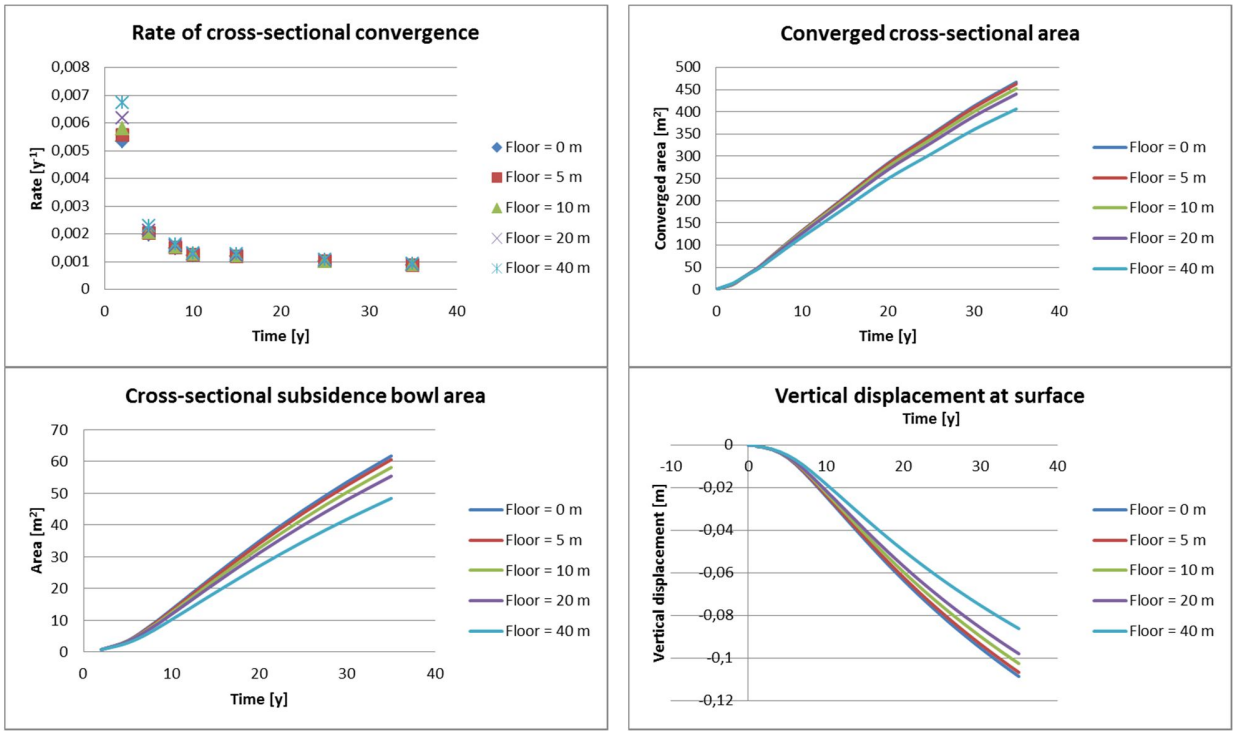

Figure 78: Results of the variant with different thickness of the salt floor

Combined results

In Figure 79 the total converged cross-sectional area in year 35 is plotted against the cross-sectional area of the cavern in that year. This is done for all calculation variants in the category of cavern dimensions, all represented by one marker in the graph. For example the lower left blue marker represents the 75 m diameter cavern that has a cross-sectional area of 7854 m^2 in year 35 and has lost 316 m^2 since the start.

All markers seem to follow a global trend with increasing converged area for increasing cavern cross-sectional area. So for convergence behavior, the cross-sectional area seems to be the determining factor. Figure 80 zooms in on the area where the markers are. Linear trendlines are drawn through the markers. From the equations of the trendlines it can be learned that the influence of the diameter is the largest of the three, because it has the trendline with the highest gradient (0.0268). But the difference with the trendline gradient of the salt roof variants is very small (0.0043). The thickness of the salt floor apparently has a slightly bigger influence than that of the salt roof. This is probably due to the fact that the salt floor is situated lower in the salt and is therefore experiencing higher stress and temperature resulting in a higher convergence.

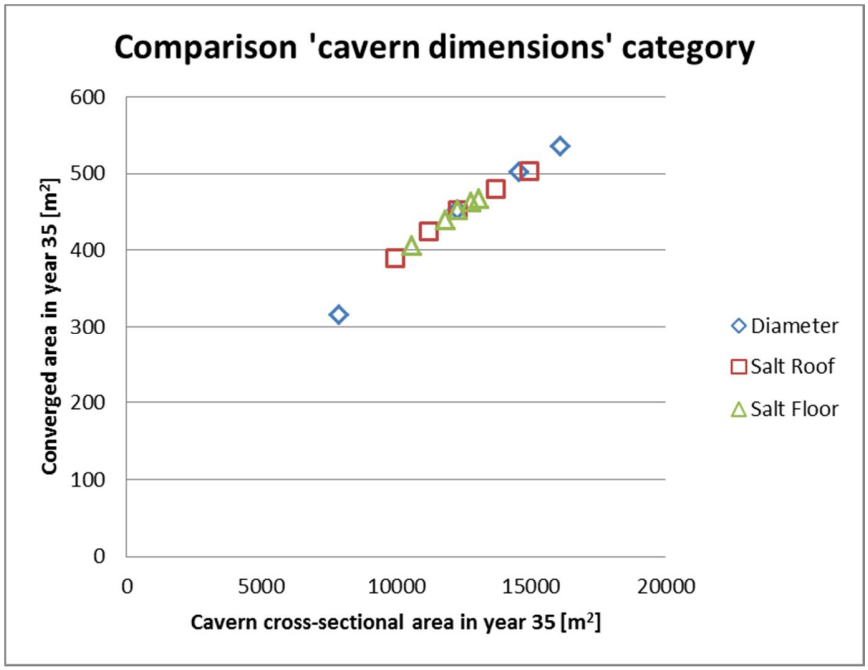

Figure 79: Results of cavern dimension variants with respect to the cross-sectional cavern areas in year 35

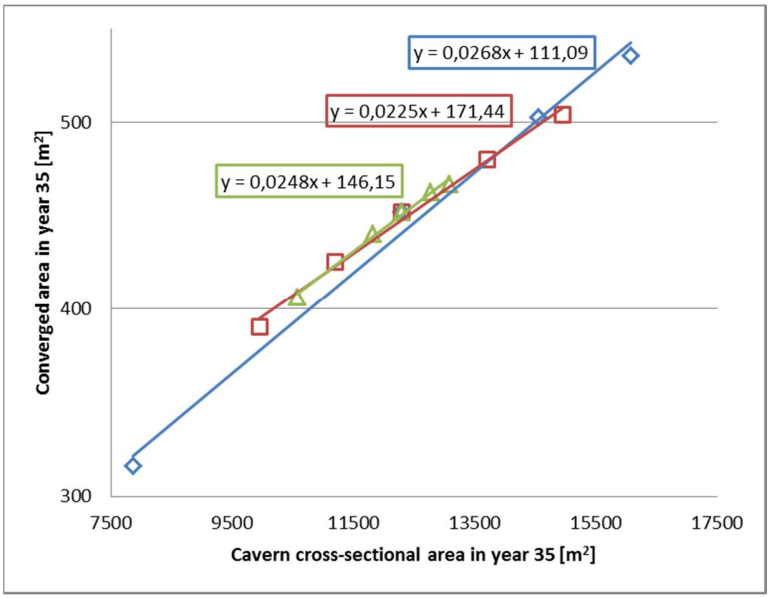

Figure 80: Zoom-in on the results presented in Figure 79

9.2.2. Salt properties

In this subsection the results of the variation of two creep parameters *A* and *n* are presented, as well as the variation of the elasticity modulus of salt. In the last part of this subsection the results of all salt parameter variants are compared.

Creep parameter A

The parameter *A* in Fokker's creep law is a scaling factor for the creep rate, see (Eq. 3.12). The results of the variants with different values for this parameter are presented in Figure 81. The *A*-value for the base case is 0.0012 [s^{-1}].

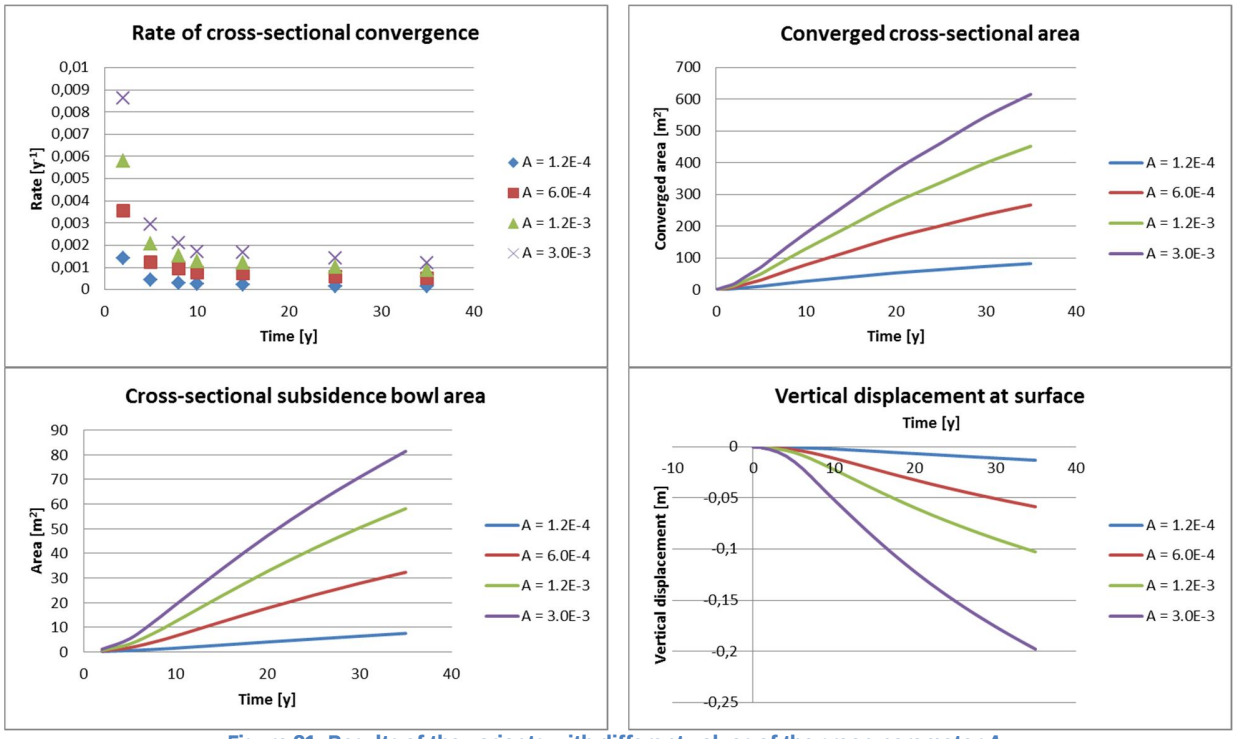

Figure 81: Results of the variants with different values of the creep parameter *A*

The rate of cross-sectional convergence (upper left diagram) clearly increases with larger values of *A*. Looking at the blue markers that represent the lowest value for *A* in this study, that is 10 times lower than in the base case (green markers) it can be seen, that although the creep rate of the salt is 10 times higher in the base case, this does not mean that the rate of cross-sectional convergence is 10 times higher, because this is related to the geometry.

Compared to the results shown in the previous subsection, the spread in rate of cross-sectional convergence is significantly bigger. Consequently the converged cross-sectional area (upper right diagram) shows a large spread as well. The same applies to the subsidence bowl and vertical subsidence (lower diagrams).

Creep parameter n

The creep parameter n is the stress exponent in Fokker's creep law. In the base case its value is 3. The results for the variants with different n values are presented in Figure 82.

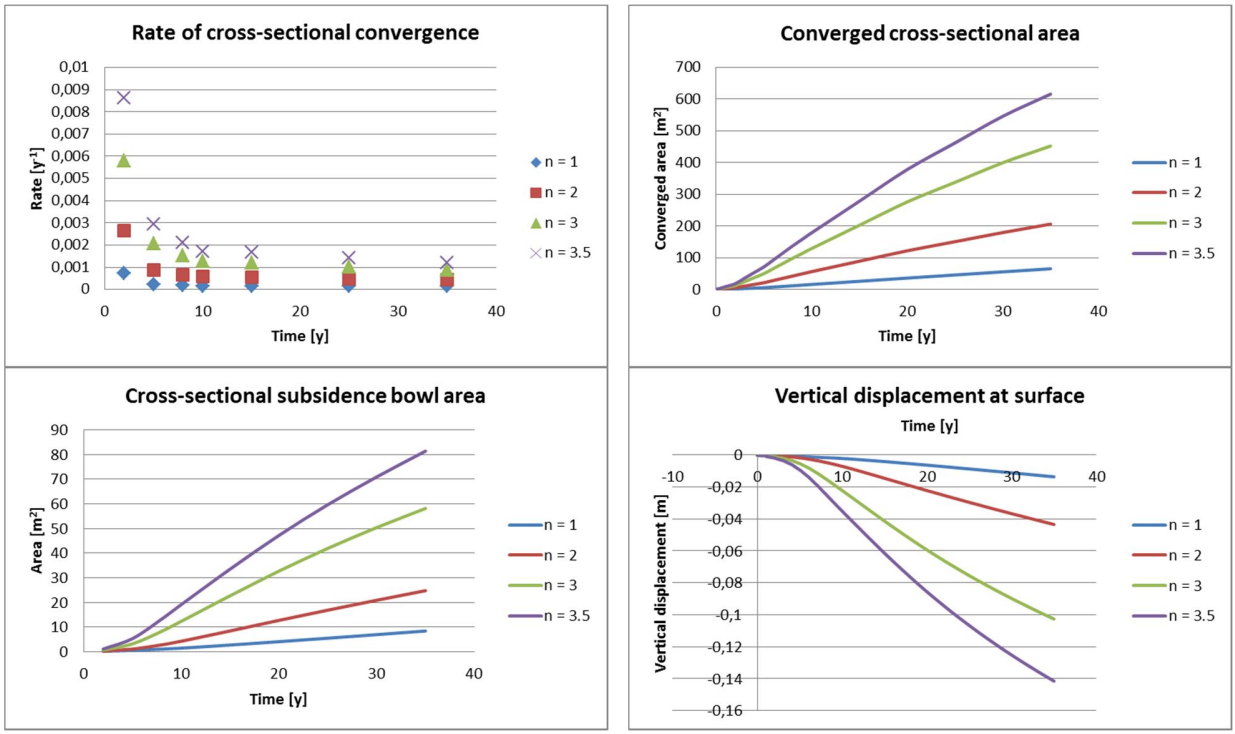

Figure 82: Results of the variants with different values for the stress exponent *n* of the creep law

These results show the same characteristics as described under the previous heading on the variation of the creep parameter *A*.

Elasticity modulus E

In Figure 83 the results of the calculation variants with different elasticity moduli for salt are presented. The value in the base case is 30 GPa.

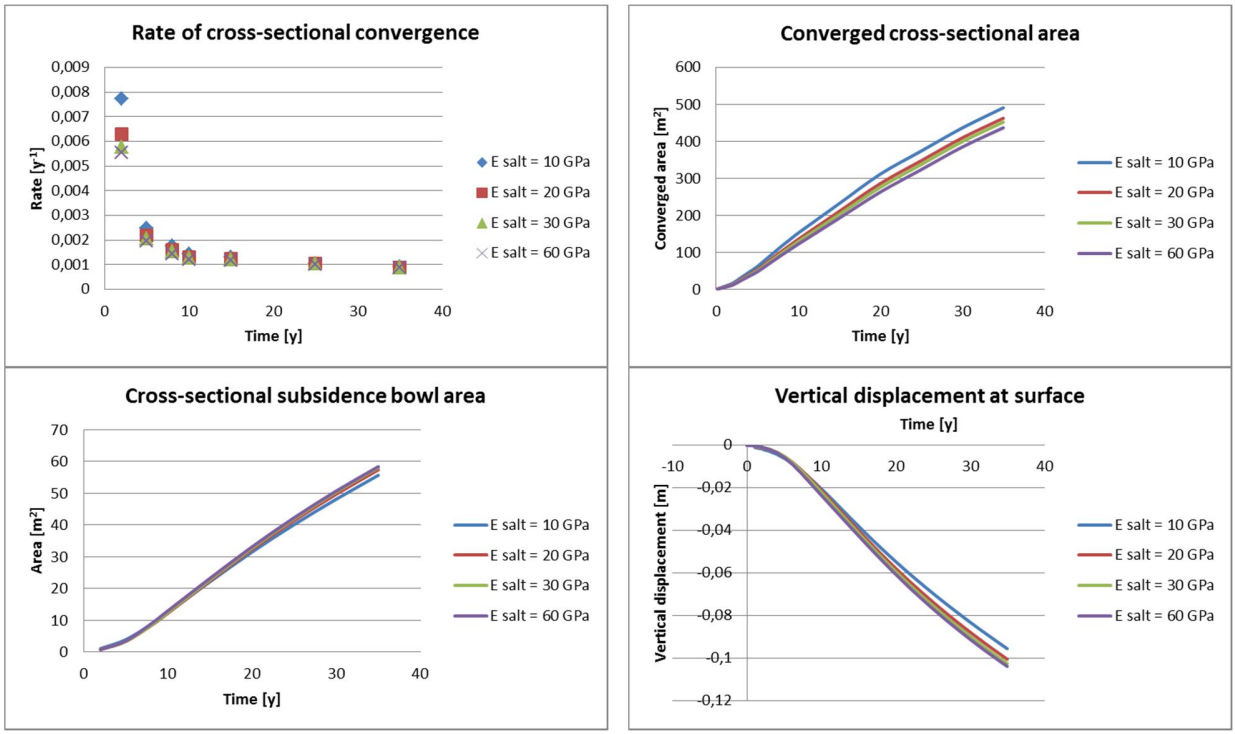

Figure 83: Results of calculation variants with different values for the elasticity modulus of salt

The first thing that can be noticed here is that the spread in the results for this elastic parameter is much smaller than for the creep parameters. The rate of cross-sectional convergence as well as the converged cross-sectional area is largest for the low value of the elasticity modulus of salt (10 GPa). Hooke's law (Eq. 3.3) tells that a low elasticity modulus results in large deformations and a high elasticity modulus implies low deformability. From this perspective the term 'stiffness' describes the physical meaning better then 'elasticity' modulus. Since a low elasticity modulus means a high deformability, it is plausible that the convergence is higher when the elasticity modulus is lower.

A second thing that can be noticed here is that although the convergence is bigger for the low elasticity modulus, the vertical subsidence (lower right diagram) as well as the cross-sectional subsidence bowl area is smaller for this value. This is in contrast with the results so far where a higher convergence automatically has led to more subsidence. To investigate whether this is due to the fact that areas are compared instead of volumes, the volumes of the caverns and subsidence bowls in the variants with the highest salt deformability (no. 020, E_{Salt} = 10 GPa) and lowest salt deformability (no. 023, E_{Salt} = 60 GPa) are calculated in 3D.

In Table 22 the volumes at times t = 10 years and t = 35 years are listed. For the E_{Salt} = 10 GPa variant the convergence volume between year 10 and year 35 is larger (112282 m^3) than the E_{Salt} = 60 GPa variant (105322 m^3). But the increase in subsidence bowl volume between year 10 and 35 is larger for the

E_{Salt} = 60 GPa variant, namely 104817 m^3. Where this is 103608 m^3 for the E_{Salt} = 10 GPa variant. This eliminates that this is due to the fact that areas are compared in Figure 83.

Since the only thing that is different in the two variants is the elasticity modulus of salt, the cause of this feature must be derived from this fact. The explanation is that the deformable salt in the variant E_{Salt} = 10 GPa takes up a larger portion of the deformations elastically. Where the less deformable salt with E_{Salt} = 60 GPa is not capable of doing this. Because it is not capable of taking up this deformation, it is translated to surface. Therefore in the bottom row of Table 22, it can be seen that for E_{Salt} = 10 GPa 92.27% of the converged volume is translated to surface, where this is almost 100% (namely 99.52%) for E_{Salt} = 60 GPa.

	E_{Salt} = 10 GPa	E_{Salt} = 60 GPa
Cavern volume in y 10 [m³]	2198756	2208370
Cavern volume in y 35 [m³]	2086474	2103048
Convergence volume y 10 to 35 [m³]	112282	105322
Subsidence bowl volume in y 10 [m³]	35266	35031
Subsidence bowl volume in y 35 [m³]	138874	139848
Increase subsidence bowl volume y 10 to 35 [m³]	103608	104817
Subsidence/convergence y 10 to 35 [%]	92.27	99.52

Table 22: Cavern and subsidence volumes in year 10 and 35 for E_{Salt} = 10 GPa and E_{Salt} = 60 GPa

Combined results

In Figure 84 the converged cross-sectional area in year 35 is plotted against the parameter variation of the salt properties as a sensitivity analysis to investigate which parameter influences the convergence the most. It shows that the stress exponent *n* has the largest influence, followed by the factor *A*. The influence of the elasticity modulus of salt has an inverse effect. A larger value for E_{Salt} means less convergence.

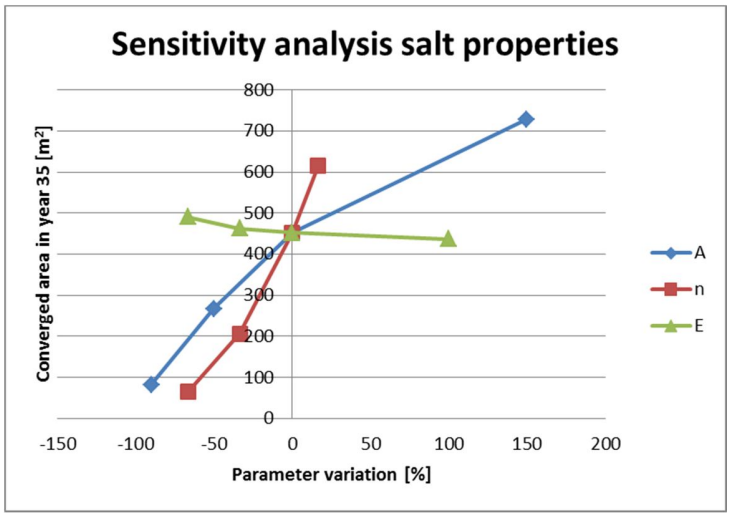

Figure 84: Sensitivity analysis of salt properties

It can be argued that the chosen variation in the parameters *A* and *n* is too large in the light of the results of the laboratory creep test. This is a fair point. In Figure 85 an upper (green) and a lower curve (red) enclose all creep test results. The equation of the upper line is (Eq. 9.4) and the lower line is (Eq. 9.5).

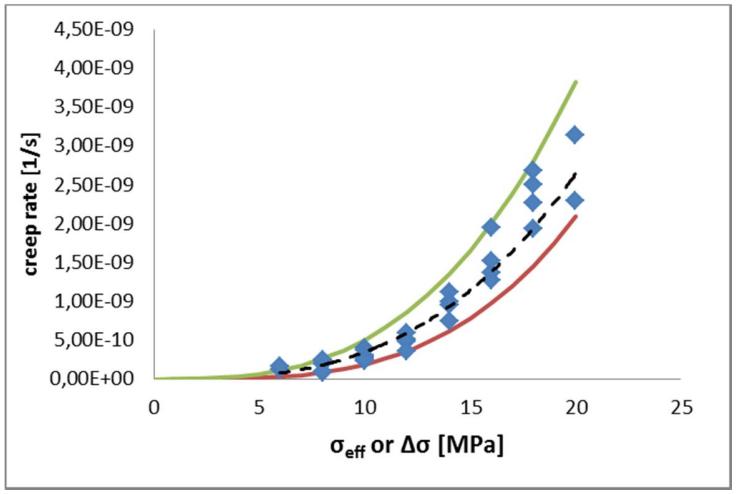

Figure 85: Creep test results of the Haaksbergen salt (blue markers), with a best fit (dashed black line), an upper (green line) and lower (red line) boundary

$$\dot{\varepsilon}_{cr} = 6.08 \cdot 10^{-13} x^{3.02} \qquad \text{(Eq. 9.4)}$$

$$\dot{\varepsilon}_{cr} = 6.61 \cdot 10^{-14} x^{3.46} \qquad \text{(Eq. 9.5)}$$

So from the creep test results it is likely that the parameter *n* will vary between 2.92 (best fit)and 3.46 (lower boundary) instead of the variation of *n* =1 to *n* = 3.5 in this study. However, these creep tests are carried out on samples from a single exploration well. So it is unknown how representative these samples are for the entire pillow salt deposit. For this reason it is interesting to see how a large variation of these parameters influences the results.

When the *A*-values of the upper and lower boundary curves are calculated from (Eq. 9.4) and (Eq. 9.5) by dividing the factors by $3.37 \cdot 10^{-10}$, the results *A* = 0.0018 and *A* = 0.0002 are found. These fit quite good in the range of the variation of *A* in this study (0.00012 to 0.003).

9.2.3. Elasticity moduli

First, in order to understand how the model reacts when the overburden is relatively deformable or relatively undeformable, two models were made where all the overburden units were assigned the same value for elasticity. In the first model the elasticity modulus of the overburden is very high (60 GPa) compared to that of salt (30 GPa). In the second model the elasticity modulus of the complete overburden is only 6 MPa which is around 1000 times smaller than the weighted average of the overburden in the base case that is around 6 GPa.

The deformation in the models between year 34 and 35 is studied by looking at the cross-sectional areas of different units in both models. For this purpose the model was divided in 5 units: cavern, salt, overburden, base and subsidence bowl, see Figure 86. The difference in cross-sectional area and the corresponding percentages are listed in Table 23.

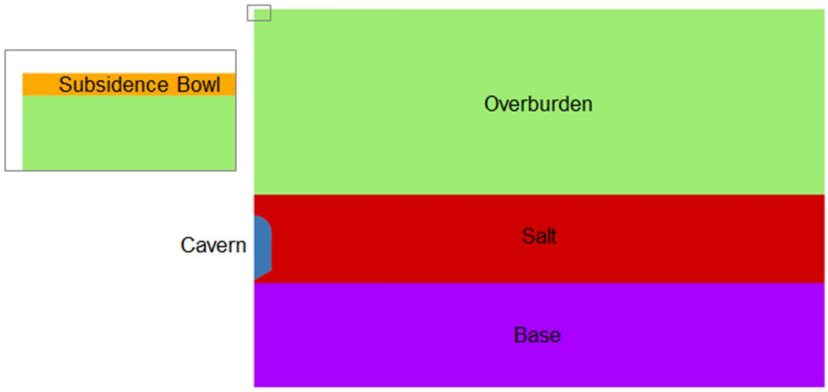

Figure 86: Division of the axisymmetric model into 5 units: cavern, salt, overburden, base, and subsidence bowl

	$E_{Overbuden}$ = 60 GPa (low deformability)		$E_{Overburden}$ = 6 MPa (High deformability)	
Unit	**ΔA [m²]**	**%**	**ΔA [m²]**	**%**
Cavern	-7.690934	-100	-27.752836	-100
Salt	6.726704	87.4627711	14.919347	53.75791865
Subsidence bowl	0.770549	10.01892618	4.317571	15.55722449
Overburden	0.049927	0.649166928	8.520027	30.69966255
Base	0.143661	1.867926574	-0.00411	-0.014809297
	Total	-0.001209217	Total	-3.60334E-06

Table 23: Deformations in the model with different deformability of the overburden from year 34 to 35

Two things need to be discussed here. Firstly, the decrease of cavern cross-sectional area from year 34 to 35 is much larger for a highly deformable overburden. Intuitively it can be expected that the amount of convergence remains constant because the salt properties and loads in the model are not changed. However these results indicate that cavern convergence is stimulated by a very deformable overburden.

Secondly, looking at the percentages, it can be seen that the highly deformable overburden takes up a large portion of the deformation (30.7 %), where this is only 0.6 % when the overburden has a very low deformability.

Instead of showing the four diagrams with the rate of cross-sectional convergence, the converged cross-sectional area, the cross-sectional area of the subsidence bowl and the vertical subsidence along the axis, the results are combined in a sensitivity analysis. In the base case the standard values are: E_{Salt} = 30 GPa, E_{Z2Z4} = 15.5 GPa, $E_{Triassic}$ = 5.5 GPa and $E_{Tertiary+Quarternary}$ =34 MPa.

First, the converged cross-sectional area in year 35 is plotted against the parameter variation in Figure 87. The trend of the lines (lower converged cross-sectional area at higher values of the elasticity modulus) matches the results from the study described above. The very limited influence of the elasticity modulus of the Tertiary + Quarternary is due to the small thickness of this layer. Moreover, its position at the top of the model, makes it situated at the largest distance from the area where the actual convergence is happening (in the vicinity of the cavern).

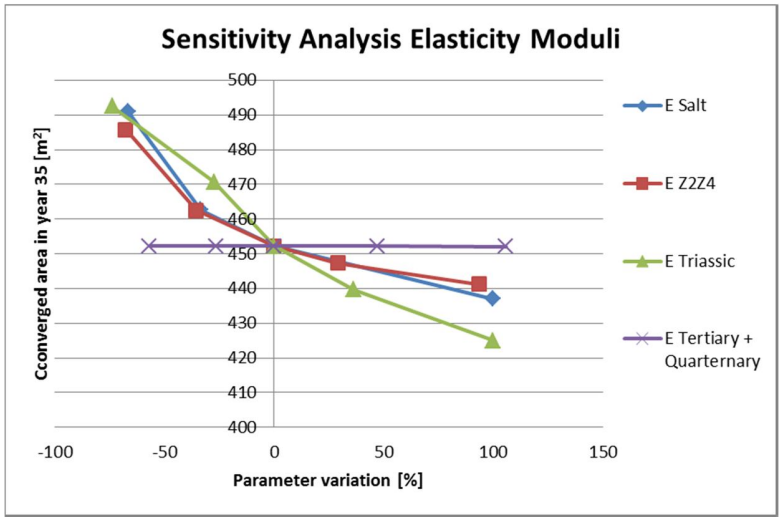

Figure 87: Sensitivity analysis of the variation of the elasticity moduli of different geological units

To investigate how the portion of the convergenced volume that contributes to the subsidence bowl is influenced by different values of the elasticity modulus, 3D volume calculations were done for the variants with the largest and smallest elasticity modulus per unit, the results are listed in Table 24. The unit Tertiary + Quarternary is left out, because the variation in results is very minimal. As has been indicated in Figure 87.

Variant	Convergence volume increase between year 10 and 35 [m³]	Subsidence bowl volume increase between year 10 and 35 [m³]	Subsidence / convergence volume [%]
E_{Salt} = 10 GPa	112282	103608	92.27
E_{Salt} = 30 GPa	107062	106500	99.47
E_{Salt} = 60 GPa	105322	104816	99.52
E_{Z2Z4} = 5 GPa	114980	114543	99.62
E_{Z2Z4} = 15.5 GPa	107062	106500	99.47
E_{Z2Z4} = 30 GPa	105513	104882	99.40
$E_{Triassic}$ = 2 GPa	118413	118000	99.65
$E_{Triassic}$ = 5.5 GPa	107062	106500	99.47
$E_{Triassic}$ = 11 GPa	100550	99613	99.07

Table 24: 3D volume calculations for the elasticity moduli variants

First of all, since for all variants the percentage of convergence volume that is translated to surface is very close to 100%, except for E_{Salt} = 10 GPa (see first row of Table 24). It can already be concluded that the influence of overburden elasticity on the amount of subsidence is very minimal. It can also be seen that the convergence volume increase between year 10 and 35 is for each unit the biggest when the elasticity modulus is the lowest.

Looking at the right most column, it can be seen that the percentage of the convergence volume that contributes to the subsidence bowl increases when the stiffness of salt increases, as has been discussed in 9.2.2. For the other two units this is the other way around. The stiffer the overburden, the smaller is the portion of convergence volume that is translated to surface in the form of a subsidence bowl.

9.3. Double cavern analysis

To investigate the influence of the presence of a second cavern on the convergence behaviour of a cavern, a plane strain model was developed. In fact, five models were made with a different cavern spacing. The results of this study are presented in subsection 9.3.2. In the now following subsection the results of a plane strain model with only one cavern are presented. A comparison between an axisymmetric and plane strain analysis can be made this way.

9.3.1. Comparison with axisymmetric analysis

The plane strain model with only one cavern was designed to resemble the axisymmetric model in as many aspects as possible. For example the material properties, layer thickness, cavern dimensions, brine pressures and the division of the cavern in 10 phases are kept.

In Figure 88 the results of the plane strain single cavern model are shown. The rate of cross-sectional convergence is consequently higher than in the axisymmetric model. This is a consequence of the fundamental difference between axisymmetric and plane strain models. A plane strain model is infinitely long in the direction normal to the plane. This means that the cavern is modelled as an endless tunnel. So the salt that is present beyond the cavern in the *z*-direction is not modelled and therefore the whole cavern does not get support from this salt. For this reason the rate of cross-sectional convergence is higher for a plane strain analysis. This causes the difference in the converged cross-sectional area (upper right diagram). Since in the axisymmetric model only half the cavern cross-section is modelled, the values are doubled to be able to make a fair comparison with the plane strain analysis that models the complete cross-section of a cavern.

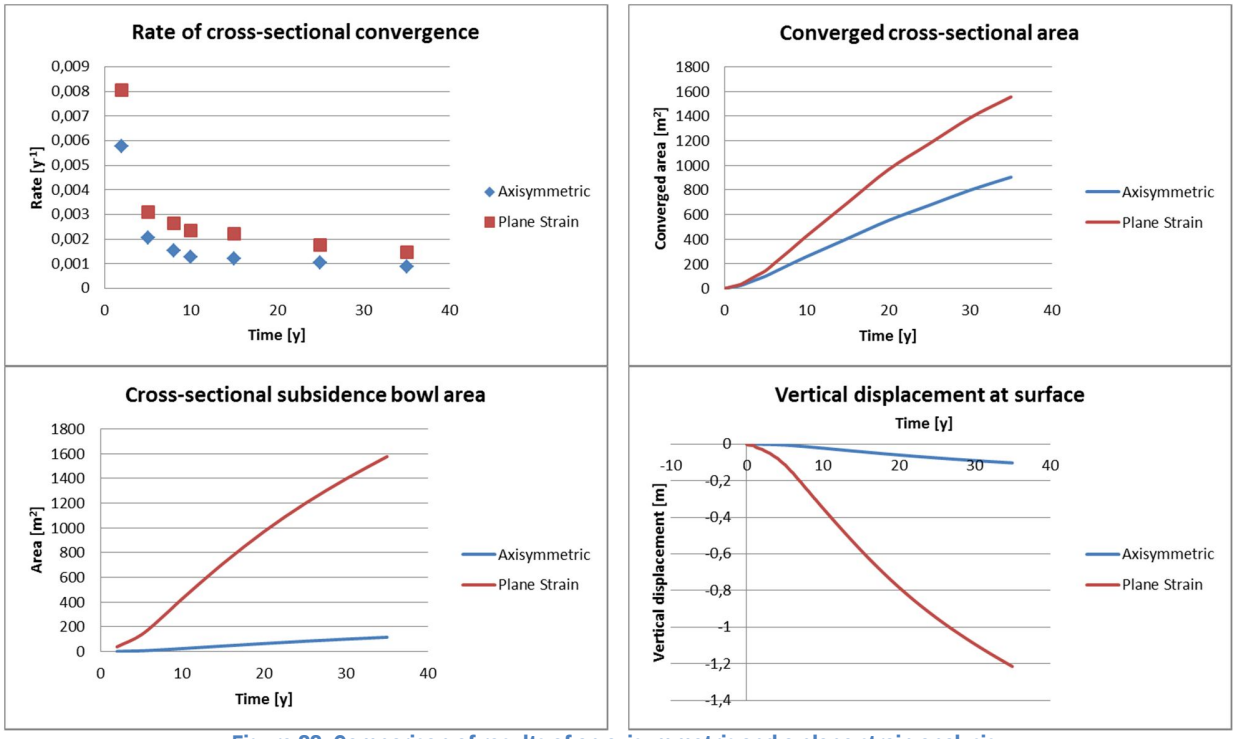

Figure 88: Comparison of results of an axisymmetric and a plane strain analysis

The difference in the cross-sectional area of the subsidence bowl is quite noticeable, even though the cross-sectional area of the axisymmetric subsidence bowl is already doubled for the same reason as described above for the converged cross-sectional area. This large difference can also be seen in the vertical displacement at surface.

When the converged cross-sectional area and the cross-sectional subsidence bowl area of the plane strain analysis are compared, that are about 1557 and 1577 m^2 respectively, it can be seen that these are almost equal. Here the problem of the conversion from area to volume does not play a role, because there is no rotation around an axis.

The fact that the cross-sectional area of the subsidence bowl is 20 m^2 bigger than the converged cross-sectional area might be due to the fact that the cross-sectional area of the subsidence bowl is calculated less accurately towards the edges. As an example the converged cross-sectional area from year 34 to 35 and the cross-sectional area of the subsidence bowl from these years are compared in Table 25.

	t = 34 year	t = 35 year	ΔA [m²]
Cavern cross-sectional area [m²]	23354.245889	23320.254374	-33.9152
Subsidence bowl cross-sectional area [m²]	1542.053307	1576.669327	34.61602

Table 25: Cross-sectional cavern and subsidence bowl areas in year 34 and 35

The loss of cross-sectional area of the cavern almost matches the increase in subsidence bowl cross-sectional area. The fact that $|\Delta A|$ for the subsidence bowl is about 0.70 [m^2] bigger than the absolute converged area, might be due to the fact that the converged area is calculated more accurately. The distance between the nodes that define the cavern contour is always between 5 and 10 m. Where the

nodes that define the subsidence bowl at the top boundary of the model can be around 50 m apart towards the left and right hand edges of the model. Since the area is defined by drawing straight lines between the nodes, the error that is made, is bigger when the nodes lie further apart.

9.3.2. Pillar width

When the models with the different pillar widths were run, the calculations of the two variants with the lowest pillar width (50 and 125 m) did not converge. An explanation for this came when the outcome of the other variants was studied. These results are presented in Figure 89.

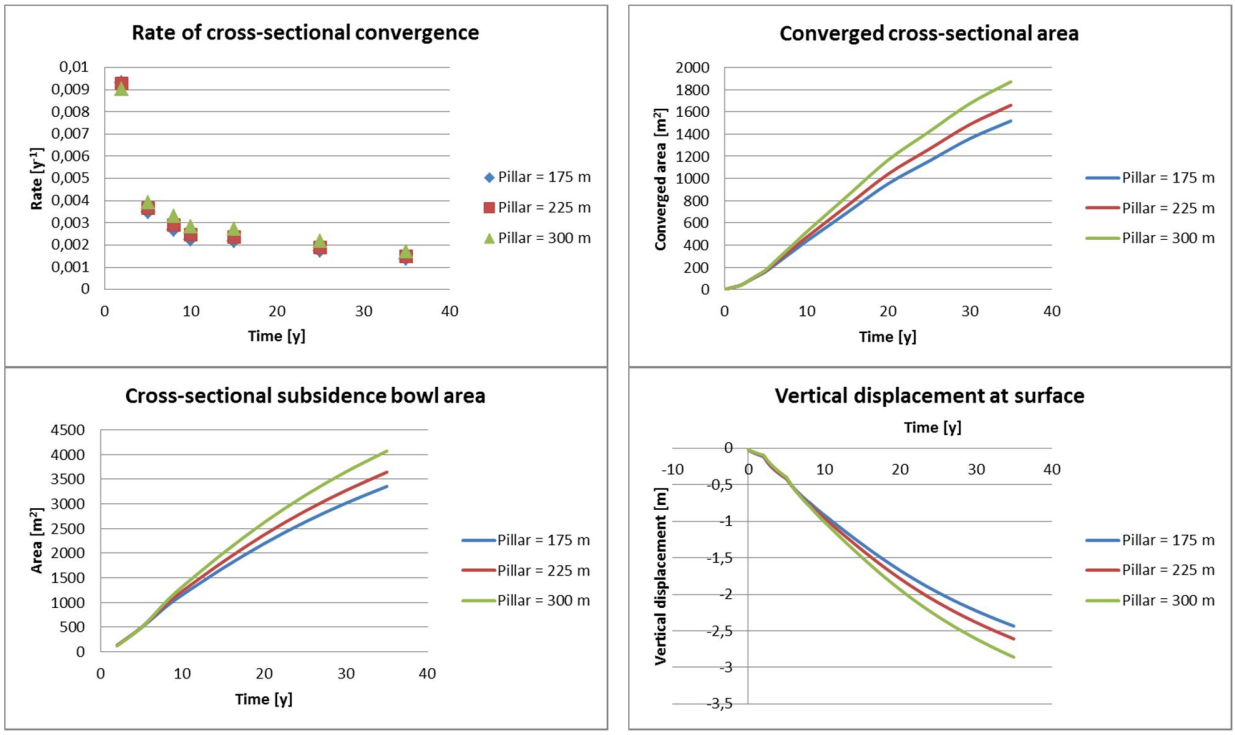

Figure 89: Results of the variants with different pillar widths

The most noticeable feature of these results is that the convergence behaviour is stronger for the variant with the largest pillar width. This is unexpected because intuitively, when caverns are further apart, they have less influence on each other.

In Figure 90 the left hand caverns of the variants with a 225 (red) and 300 m (green) wide pillar in year 35 are overlain. In the figure it has to be kept in mind that left from the caverns the model extends for about 2000 m. Right from the caverns there is a pillar and another cavern. When both cavern contours are overlain, it can be seen that the left hand sides of the caverns are almost equal. The right hand part of the W_{Pillar} = 300 m variant has converged more in year 35 than the variant with the thinner pillar W_{Pillar} = 225 m. This has happened on the side that is facing the pillar. Therefore this indicates that the load on the pillar is increased.

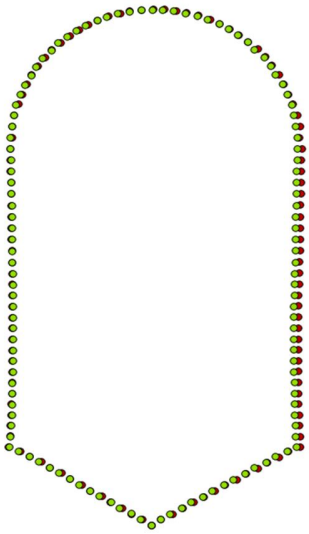

Figure 90: Contours of left hand cavern of models with a pillar width of 225 m (red) and 300 m (green)

Combining this feature of the results with the fact that the two variants with the lowest pillar width did not converge, leads to the following explanation. In the two variants with the lowest pillar width, the stress around the caverns is redistributed in such a way that the pillar is hardly loaded, see sketch of stress redistribution in Figure 91 (left). Since the pillar is not carrying a significant load the two caverns are basically combined in the model and 'seen' as one big underground opening. Because the dimensions of this opening are too big the deformations are too large for the calculations to converge.

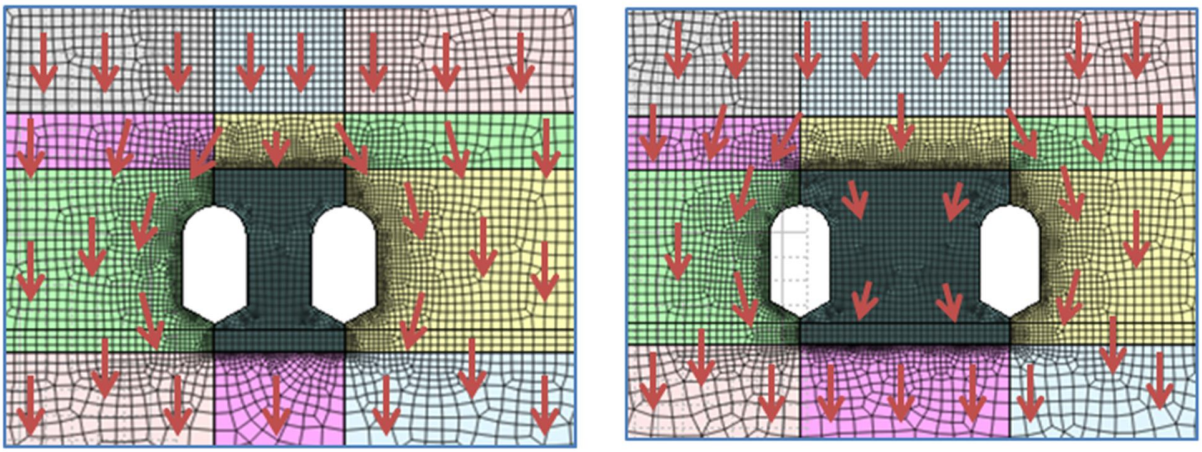

Figure 91: Images of stress redistribution around caverns, for small pillar width (left) and large pillar width (right)

When the pillar gets wider, it gets loaded more and the redistribution of stress around the caverns can be imagined as sketched in Figure 91 (right). This is supported when the distribution of the mean stress σ_m around the caverns is retrieved from a linear elastic analysis on the variants, see Figure 92 and Figure 93. As can be seen on the stress scales (equal in both figures) the lighter blue colours represent higher values of mean stress than dark blue colours. The light blue zone in the wider pillar in Figure 93 is relatively larger than in the smaller pillar in Figure 92. These larger stresses (light blue) cause larger deformations.

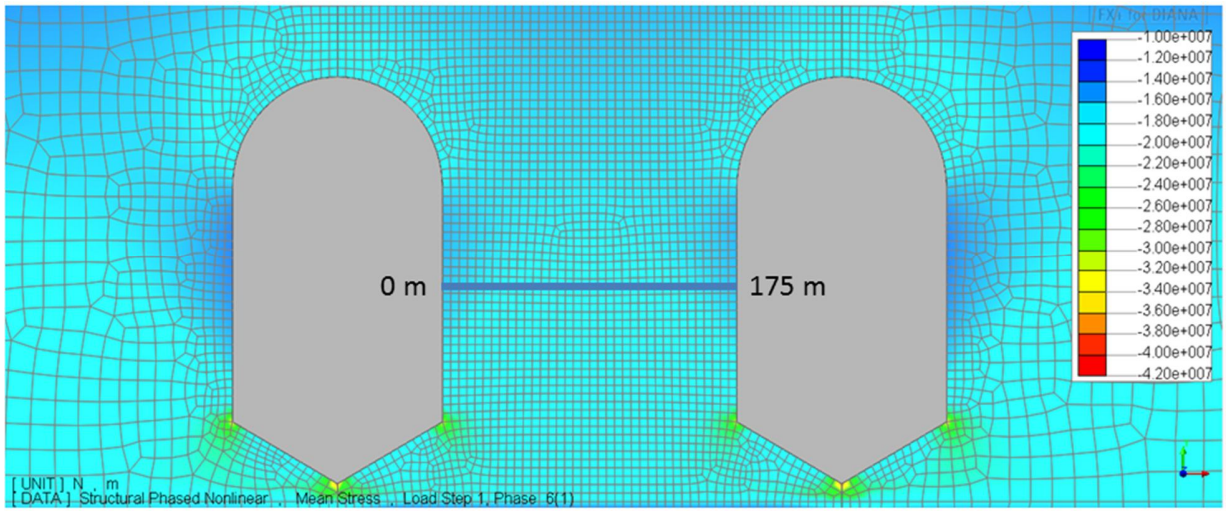

Figure 92: Distribution of mean stress around caverns separated by a 175 m wide pillar in a linear elastic analysis, including the line for the stress profiles of Figure 94 and Figure 95

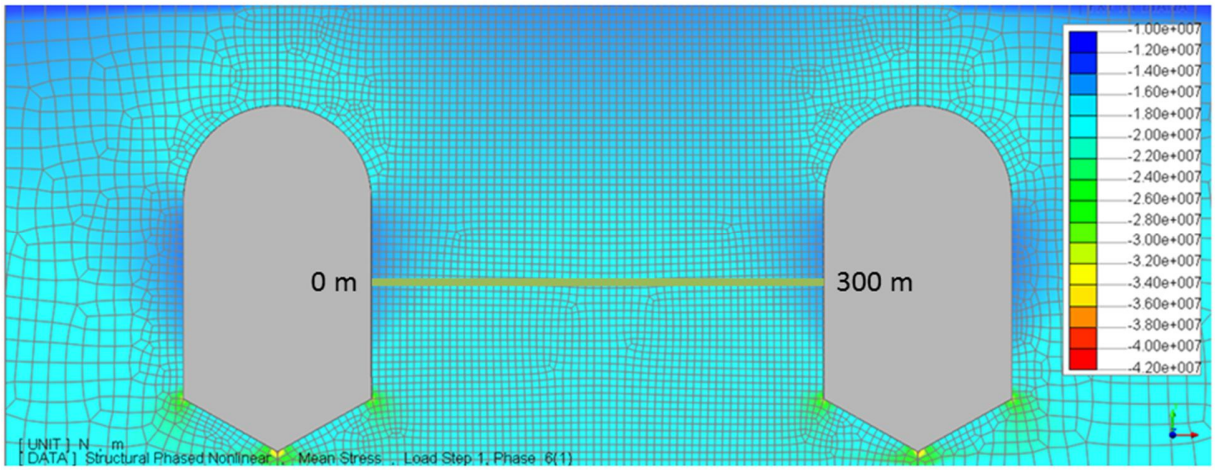

Figure 93: Distribution of mean stress around caverns separated by a 300 m wide pillar in a linear elastic analysis, including the line for the stress profiles of Figure 94 and Figure 95, stress scale equal to Figure 92

Because the colour differentiation is not very clear in Figure 92 and Figure 93, profiles of the mean stress through the pillars were made for the non-linear analysis that includes the creep behaviour. These profiles are shown in Figure 94. The mean stress is larger for the wider pillar throughout both profiles (note that compressive stresses have a negative value). This indicates that the load on the pillar increases, when the cavern spacing becomes larger as suggested in Figure 91.

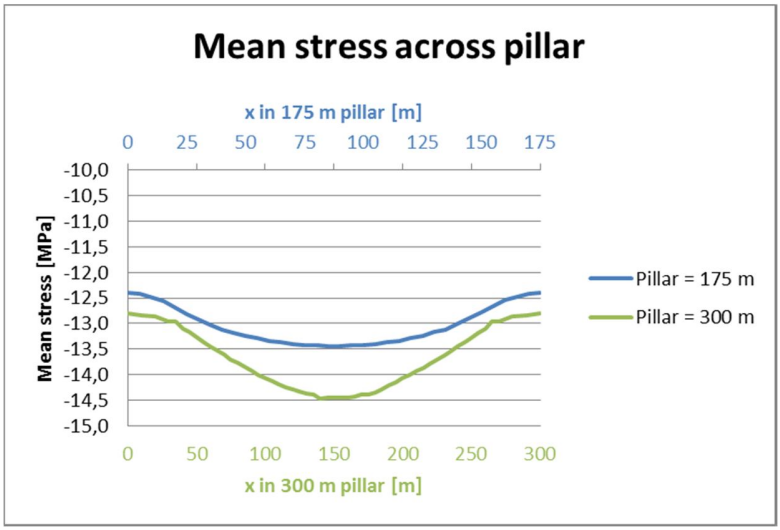

Figure 94: Profile of mean stress across 175 m wide pillar (blue) and 300 m wide pillar (green) in last time step (year 35) of nonlinear analysis

Since the differential stress ($\sigma_1 - \sigma_3$) influences the creep rate (see σ_{eff} or $\Delta\sigma$ in Eq. 3.12 on page 15), profiles of the differential stress across the pillars were made as well. These profiles are presented in Figure 95. The diagram shows that the differences between the differential stress profiles are very minimal. For this reason it is concluded that the cause of the difference in convergence must not be sought in different creep deformations. This leads to the conclusion that the larger convergence in the caverns that are separated by wider pillars is caused by higher mean stress in the pillars that causes larger (elastic) deformations.

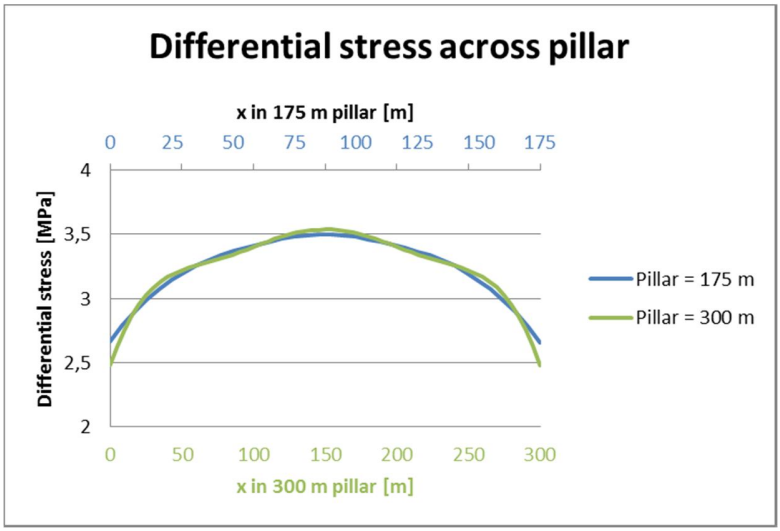

Figure 95: Profile of differential stress across 175 m wide pillar (blue) and 300 m wide pillar (green) in last time step (year 35) of nonlinear analysis

10. Conclusion and recommendations

In the first part of this chapter, the conclusions of this work are presented. They are formulated to answer the research questions from section 1.2. This is followed by a section where recommendations are made.

10.1. Conclusions

In this section on conclusions the research questions from section 1.2 will be answered.

Question 1: Which fundamental differences in the approaches to geomechanical modelling of salt deposits can be distinguished and how do these approaches influence the results?

The fundamental differences in the approaches to the geomechanical models that were discussed in chapters 4 to 7 do not originate in the fact that the caverns were situated in different salt deposits, rather in the fact that different parties were asked to make the geomechanical models. All consultants that were mentioned apply, for instance, their own material model or constitutive law to model the behaviour of salt. They have developed experience and gained confidence in the quality and applicability of this model as well as their general approach to the modelling process.

For example, the BGR has applied the same material model (BGRa) to the bedded salt deposit of Hengelo and the salt domes of Heiligerlee and Zuidwending. Although the parameter values were different in both cases, the approach was the same, since the same material model was used. But not all aspects of the geomechanical models were similar. The difference in the nature of the salt deposits, leads to some differences in the simplifications and assumptions, for example the implementation of temperature in the model. The limited depth of the Hengelo caverns allows the assumption of a constant temperature, where this is not possible in the Heiligerlee and Zuidwending caverns that are deeper and hundreds of meters high.

Another example is the comparison of the geomechanical models made by IfG on the gas storage project in Zuidwending (salt dome) and the generic cavern design for the future Haaksbergen brine field (pillow salt). Again, the same material model was used for salt, so the same approach to the mechanical behaviour of salt was applied, despite the difference in the type of deposit. A difference between both models can be found in the evaluation criteria. The fact that the caverns in Zuidwending needed to be designed for gas storage, made it necessary to apply a gas tightness criterion. The Haaksbergen generic cavern model is not evaluated on this criterion.

In the last part of this question it is asked why different approaches lead to different results. The outcome of a model depends on every input to the model. Examples are material parameters, or the input of depth-dependent temperature. Some of the studies that are referred to in chapters 4 to 7 include calculation variants where the values of some parameters or the influences of assumptions and simplifications are tested. Performing a sensitivity analysis gives insight to the influence that a parameter, assumption or simplification has on the results.

Question 2: What is relevant from this, regarding geomechanical modelling and subsidence prediction of the future operation in Haaksbergen?

From the current geomechanical models it can be learned that it is not always necessary to make the most sophisticated model possible. Often a simpler analysis with conservative assumptions already leads to results that prove the stability of a cavern design or indicate that the amount of subsidence is acceptable. This makes it unnecessary to develop more sophisticated models that cost more time and money, but that are less conservative and therefore more realistic. This can be seen as an opportunity from the business point of view, because more sophisticated models may prove that a higher extraction ratio is possible.

It should be noted here that the geometry of the Haaksbergen pillow salt deposit is not 'continuous' across the area. The Hengelo Röt Salt deposit is thin and stretches over a large area, where the Zuidwending and Heiligerlee salt domes are thick, but limited in horizontal dimensions. This makes these salt deposits and their caverns suitable for plane strain and axisymmetric models. This does not apply to the Haaksbergen salt deposit that has a large thickness variation, see Figure 44 on page 65. The future Haaksbergen brine field is therefore most suitable for the development of a 3D model.

The amount of available data for the Haaksbergen brine field is very limited (only salt properties are known and only for the location of the exploration well). Therefore it is not logical to make a more sophisticated model than there is at the moment.

Question 3: Which factors influence the convergence of a cavern in salt and the subsidence that results from this?

This question applies to the modelling part of the thesis work.

- The results that are presented in chapter 11 indicate that the convergence behaviour of a single cavern is mainly influenced by the creep properties of the salt (the parameters *A* and *n*, see Figure 84 on page 108). Higher values of *A* and *n* result in stronger convergence. On the contrary, a higher elasticity modulus for salt results in less convergence, because the salt is less deformable.
- From the outcome of the variation of the cavern dimensions it is derived that the cavern cross-sectional area (or volume) largely influences the convergence, see Figure 79 on page 104. This diagram shows that there is no large difference in which of the dimensions is changed. However, as shown in Figure 80 on page 104, the diameter has a slightly larger influence on the results than the salt floor and salt roof thickness respectively.
- By 3D volume calculation of some of the calculation variants for different values of overburden elasticity it is shown that these only marginally influence the portion of the convergence volume that contributes to the subsidence bowl. The larger the value of the overburden elasticity modulus, the lower the percentage of convergence volume that contributes to the subsidence bowl. However, as shown in Table 24 on page 111, despite the variation of overburden elasticity, the portion of convergence volume that contributes to the subsidence bowl remains between 99.0 and 100.0%.

The outcome of the plane strain analysis of a single cavern has shown that a plane strain analysis is much more conservative than an axisymmetric analysis, because it results in much more convergence and subsidence, as shown in Figure 88 on page 113. The variants with different pillar widths have shown that a larger cavern spacing does not lead to less convergence, see Figure 89 on page 114. Due to the stress redistribution around caverns the pillar between the caverns is increasingly loaded when the pillars are wider and caverns are further apart.

10.2. Recommendations

A number of recommendations are made regarding the modelling study described in chapters 10 and 11. Since an initial objective of this project was to make a 3D model, recommendations for making this model are also made here.

- Based on the results of this study it is concluded that the elasticity modulus of different overburden units does not have a significant influence on the amount of subsidence at surface. An implication of assigning linear elastic behaviour to the overburden units is that the influence of the strength of the overburden on the amount of subsidence can not be tested, since plastic deformations are not modelled. When a more sophisticated material model such as Drucker-Prager is used, this could also be taken into account. This however, requires values for the material parameters that are representative for the overburden units. Laboratory tests need to be carried out on samples from the overburden (which are not available) to determine these values. In case they might become available in the future it can be considered to implement this into the model to see how it influences the results. However in the meantime, in a further study a material model that includes plasticity could be implemented with literature values for the parameters. By doing this, the sensitivity of the results to these material models and parameter values can be tested. The result of this study might show that it is not necessary to implement more sophisticated material models, because they do not have a significant effect on the results.
- In all models and calculation variants in this work, no discontinuities, such as fractures, were incorporated into the model. So the influence of the weakening effect of discontinuities is not taken into account. This can be considered in a possible future study. But the actual implementation of this discontinuities (how many, how long etc.) must be based on research that indicates the presence of these discontinuities. The current geological model provides insight in the location of a number of faults. However, the geomechanical properties of these discontinuities are unknown. Again, a sensitivity analysis in a future study could provide insight in the influence of discontinuities and their properties.
- Cavern sealing should be applied to calculation variants in further research to obtain results that are more applicable to the operation of the future Haaksbergen brine field.
- As an extension of the plane strain analysis on two caverns in this work, it can be considered to develop more models with even wider pillars. This way it can be investigated whether the trend of increasing convergence with increasing pillar width holds. Perhaps from increase above a certain value, the convergence decreases.
- In this work only pressures of static brine columns are applied. In practice, this situation only occurs when a cavern is disconnected from the production network, for example to do a

workover. During production an extra pressure is supplied from the network to be able to 'push' the brine (with a higher density than the water that is injected) out of the cavern. Implementation of this production pressure puts a limitation on the convergence and subsidence and gives more realistic results.
- The effect of the injection of water that is colder than the temperature in subsurface, was not investigated in this work. In further research this can be implemented by applying a lower temperature near the cavern contour during the period of cavern development (first 10 years).

In a 3D modelling study the following should be considered:

- The layer interfaces between the geological units Carboniferous, Z1 anhydrite, Z1 Salt, Z2-Z4, Triassic and Tertiary + Quarternary for the area are already available in a 3D 25 x 25 m grid that can serve as an input into DIANA.
- At each cavern location the thickness of the salt layer will be different. When the design parameters of a 10 m thick salt floor and a 70 m thick salt roof are kept, all caverns will have a different height and consequently a different volume. It needs to be considered how the development of the caverns will be simulated; in how many phases will the caverns be developed? Keeping in mind that the size of the sump phase will be equal for all caverns (35 m high and a diameter of 125 m) and that its development will take 2 years.
- The models that have been developed in this thesis work include depth-dependent input. Namely the temperature and the brine pressure. These are all calculated with respect to the top of the model (+25 m NAP, which is surface level), so not with respect to 0 NAP. The elevation of the planned phase-1-caverns varies between +20 m NAP and +25 m NAP roughly. This is not a large variation, looking at the hundreds of meters depth at which the caverns will be situated. However, it needs to be considered which assumption or simplification will be made here.
- It needs to be considered if and how cavern sealing is going to be implemented in the model. Questions like: "How long will a cavern remain open after leaching is stopped?" and "To which percentage of the lithostatic pressure will the brine pressure in the cavern increase?" are relevant here.
- Also it needs to be considered whether the dynamic pressure that is necessary to push the brine out of the cavern will be added to the brine pressure in the cavern. On the one hand, this would be more realistic, on the other hand this increases the complexity of the model. Particularly when it is considered that this dynamic pressure is also released during workovers in a number of periods during a cavern's lifetime.
- How is it going to be implemented that the twelve caverns are not developed simultaneously? Wells will be drilled one by one, and therefore caverns start to develop one by one. Smaller caverns will be completed in a shorter period of time than the larger ones.
- To be able to study cavern convergence it is required to retrieve the coordinates of the nodes that are at the cavern contours at different points in time. This requires an intelligent way to list the numbers of the nodes that form the contours of the caverns, so that DIANA gives the displacement of these nodes as an output. 3D software such as Surpac or AutoCAD is required to calculate the volume of 3D bodies.

11. References

AKZO NOBEL SALT B.V., 2003. *Winningsplan voor de winningsvergunningen Twenthe-Rijn en Twenthe-Rijn Uitbreiding (boorterrein Hengelo).* Hengelo: AKZONOBEL, 25pp.
Accessed via AkzoNobel archive

AKZO NOBEL SALT B.V., 2008a. *Aanpassing Winningsplan Adolf van Nassau ten behoeve van de uitbreiding van de zoutproductie in Delfzijl.* Hengelo: AKZONOBEL, 26pp.
Accessed via AkzoNobel archive

AKZO NOBEL SALT B.V., 2008b. *Aanpassing winningsplan Adolf van Nassau Uitbreiding ten behoeve van de uitbreiding van de zoutproductie in Delfzijl.* Hengelo: AKZONOBEL, 27pp.
Accessed via AkzoNobel archive

AKZO NOBEL SALT B.V., 2012. *HUT Hengelo Uitloog Techniek 7th edition.* Hengelo: AKZONOBEL, 21pp.
Accessed via AkzoNobel archive

ATKINS, 2012. *Project Lily: Geomechanical stability assessment of the planned underground gas storage caverns.* Manchester: ATKINS, 149pp.

BÉREST, P., BERGUES, J., BROUARD, B., DURUP, J. & GUERBER, B. 2001. A salt cavern abandonment test. *International Journal of Rock Mechanics and Mining Sciences*, p.357-368.

BUNDESANSTALT FÜR GEOWISSENSCHAFTEN UND ROHSTOFFE, 2000. *Diameter Enlargement of Brine Wells in the Heiligerlee Brine Field for a Field Expansion.* Hannover: BGR, 42 pp.
Accessed via AkzoNobel archive

BUNDESANSTALT FÜR GEOWISSENSCHAFTEN UND ROHSTOFFE, 2002. *Future Development and Optimization of the Zuidwending Brine Field.* Hannover: BGR, 44pp.
Accessed via AkzoNobel archive

BUNDESANSTALT FÜR GEOWISSENSCHAFTEN UND ROHSTOFFE, 2003a. *Geomechanische Berechnungen zur Pfeilerbeanspruchung zwischen den Kavernen 3 und 5 des Kavernenfeldes Zuidwending.* Hannover: BGR, 40pp.
Accessed via AkzoNobel archive

BUNDESANSTALT FÜR GEOWISSENSCHAFTEN UND ROHSTOFFE, 2003b. *Geomechanische Modellberechnungen zu Geländeoberflächensenkungen im Kavernenfeld Hengelo.* Hannover: BGR, 77pp.
Accessed via AkzoNobel archive

BUNDESANSTALT FÜR GEOWISSENSCHAFTEN UND ROHSTOFFE, 2004a. *Borung 480 Arbeitspakket 2: Durchführung von Versuchen an Steinsalzproben aus dem Röt.* Hannover: BGR, 83pp.
Accessed via AkzoNobel archive

BUNDESANSTALT FÜR GEOWISSENSCHAFTEN UND ROHSTOFFE, 2004b. *Ermittlung der zulässigen Beanspruchung von Pfeilern im Kavernenfeld Hengelo.* Hannover: BGR, 32pp.
Accessed via AkzoNobel archive

BUNDESANSTALT FÜR GEOWISSENSCHAFTEN UND ROHSTOFFE, 2004c. *Geomechanische Berechnungen zur Standfestigkeit und Integrität von Inline-Pfeilern in parallelen Kavernenreihen.* Hannover: BGR, 36pp.
Accessed via AkzoNobel archive

BUNDESANSTALT FÜR GEOWISSENSCHAFTEN UND ROHSTOFFE, 2006. *Senkungsvorausberechnungen für die Kavernenfelder Winschoten / Heiligerlee und Zuidwending.* Hannover: BGR, 32pp.
Accessed via AkzoNobel archive

BUNDESANSTALT FÜR GEOWISSENSCHAFTEN UND ROHSTOFFE, 2007. *Senkungsprognosen für die Kavernenfelder Winschoten/Heiligerlee und Zuidwending.* Hannover: BGR, 36pp.
Accessed via AkzoNobel archive

BRADY, B. H. G. & BROWN, E. T., 2006. *Rock Mechanics for Underground Mining.* Dordrecht: Springer, 628pp.

CRISTESCU, N. D. & HUNSCHE, U., 1998. *Time Effects in Rock Mechanics.* Chichester: John Wiley & Sons Ltd, 342pp.

TNO DIANA, 2011. *DIANA 9.4.3 user's manual.* Delft: TNODIANA.
Accessed via www.tnodiana.com/DIANA-manuals on 17/07/2013

DROST, G. I. A. 2012. *Geomechanical properties of a backfill material suitable for stabilising salt caverns in Twente.* MSc, TU Delft, 130pp.
Accessed via http://repository.tudelft.nl on 18/07/2013

DRUCKER, D. C. & PRAGER, W. 1952. Soil mechanics and plastic analysis on limit design. *Quarterly Appl. Math.,* 10**,** p.156-165.

EICKEMEIER, R., 2005. A new model to predict subsidence over brine fields. SMRI Fall 2005 Conference. Nancy, France, 2005. Clarks Summit: Solution Mining Research Institute, 21pp.
Accessed via online library of www.solutionmining.org on 04/03/2013

FOKKER, P. A. 1995. *The behaviour of salt and salt caverns.* Doctorate Dissertation, Delft University of Technology, 143pp.

GELUK, M., PAAR, W. & FOKKER, P., 2003. Salt. *In:* WONG, T. E., BATJES, D. A. J. & JAGER, J. D. (eds.) *Geology of the Netherlands.* Amsterdam: Royal Netherlands Academy of Arts and Sciences, p.283-294.

ROBERTSON HANDFORD, C., 1991. Marginal marine halite: Sabkhas and salinas. *In:* MELVIN, J. L. (ed.) *Evaporites, Petroleum and Mineral Resources.* Amsterdam: Elsevier, p.1-66.

HUNSCHE, U., SCHULZE, O. & LANGER, M., 1994. Creep and failure behavior of rock salt around underground cavities. 16th World Mining Congress. Sofia, Bulgaria, 1994. Sofia: Bulgarian national organizing committee, p.217-230.
Accessed via online library of www.solutionmining.org on 01/03/2013

INSTITUT FÜR GEBIRGSMECHANIK, 2009. *Geomechanical Modelling Natural Gas Storage Zuidwending (NL).* Leipzig: IFG, 49pp.
Accessed via AkzoNobel archive

INSTITUT FÜR GEBIRGSMECHANIK (IFG), 2010. *Rock Mechanical Investigations and Dimensioning for the New AkzoNobel NaCl-Brine Production Field Haaksbergen.* Leipzig: IFG, 25pp.
Accessed via AkzoNobel archive

INSTITUT FÜR GEBIRGSMECHANIK, 2012a. *Haaksbergen - update of cavern convergence.* Bad Zwischenahn: IFG, 3pp.
Accessed via AkzoNobel archive

INSTITUT FÜR GEBIRGSMECHANIK, 2012b. *Rock Mechanical Laboratory Investigations on Rock Salt from the AKZO Nobel well ISH-01.* Leipzig: IFG, 39pp.
Accessed via AkzoNobel archive

JEREMIC, M. L., 1994. *Rock Mechanics in Salt Mining.* Rotterdam: Balkema, 532pp.

KBB UNDERGROUND TECHNOLOGIES, 2012. *Development of a New Brine Cavern Field for Hengelo Salt Plant: Phase III Update of the Subsidence Prediction according to the Production Planning 2012.* Hannover: KBB, 20pp.
Accessed via AkzoNobel archive

KENTER, C. J., SCHREPPERS, G. M. A., BAAIJENS, M. N., BLANTON, T. L. & RAMOS, G. G., 1998. Compaction study for Shearwater field. SPE/ISRM Eurock. Trondheim, Norway, 1998. Richardson, USA: SPE, 28pp.

LOTZE, F., 1957. *Steinsalz und Kalisalze, I. Teil.* Berlin: Bornträger, 465pp.

LUX, K. H., 1984. *Gebirgsmechanischer Entwurf und Felderfahrungen im Salzkavernenbau - Ein beitrag zur Untwicklung von Prognosemodellen für den Hohlraumbau im duktilen Salzgebirge.* Stuttgart, Germany: Enke, 360pp.

MINKLEY, W., MENZEL, W., KONIETZKY, H. & KAMP, L. T., 2001. A visco-elasto-plastic model softening model and its application for solving static and dynamic stability problems in potash mining. *In:* AL., D. B. E., 2nd International FLAC Conference. Lyon, France, 2001. Balkema, p.21-27.

MWH, 2011a. *Evaluation of the geological and seismic velocity model for the Haaksbergen area using information from exploration well ISH-01.* Arnhem: MWH, 14pp.
Accessed via AkzoNobel archive

MWH, 2011b. *Seismic survey and geological model update of the Haaksbergen area of interest.* Arnhem: MWH, 100pp.
Accessed via AkzoNobel archive

ORANJEWOUD. 2007. *Holruimtemetingen verticaaldoorsneden I boorterrein Heiligerlee*. Heerenveen, NL: Oranjewoud.
Accessed via AkzoNobel archive (Map)

ORANJEWOUD. 2008. *Holruimtemetingen verticaaldoorsneden III boorterrein Zuidwending*. Heerenveen: Oranjewoud.
Accessed via AkzoNobel archive (Map)

RESPEC CONSULTING & SERVICES, 2008. *Selection of Salt_Subsid Y_{ss} Parameter for Akzo Nobel Hengelo and Usseleres (Netherlands) Brinefields.* Rapid City: RESPEC, 7pp.
Accessed via AkzoNobel archive

RESPEC, 2010a. *Salt_Subsid version 2.0 user's manual.* Rapid City, USA: RESPEC, 60pp.
Accessed via online library of www.solutionmining.org on 01/03/2013

RESPEC CONSULTING & SERVICES, 2010b. *Usseleres Zuid Subsidence Modeling Results.* Rapid City: RESPEC, 10pp.
Accessed via AkzoNobel archive

SCHREIBER, B. C. & HSÜ, K. J., 1980. Evaporites. *In:* HOBSON, G. D. (ed.) *Developments in Petroleum Geology.* Amsterdam: Elsevier, p.87-138.

TRUSHEIM, F. 1957. Uber Halokinese und ihre Bedeutung fur die strukturelle Entwicklung Norddeutschlands. *Zeitschrift der Deutschen Geologischen Gesellschaft***,** p.111-158.

WASSMANN, T. H. & BROUWER, M. S., 1987. The Mining of Rock Salt. *In:* LOON, A. J. V. (ed.) *Seventy-five years of mining and geology in the Netherlands.* The Hague: K.N.G.M.G., p.137-146.

Appendix A: Detailed diagram of the process of geomechanical modelling and subsidence prediction

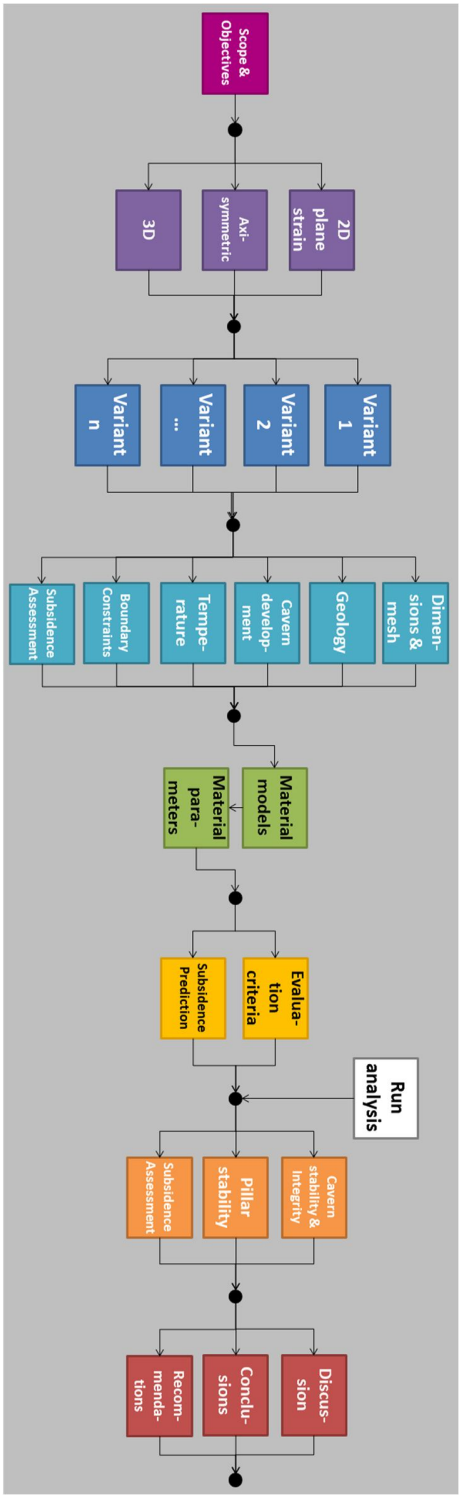

Appendix B: Process of building and running a model using DIANA